Università degli studi di Padova

DIPARTIMENTO DI FISICA E ASTRONOMIA GALILEO GALILEI

Corso di Laurea magistrale in Astrophysics and Cosmology

Master Thesis

The environment of AGN along the quasar main sequence

Candidate:
Luca Crepaldi

Supervisor:
Prof. Stefano Ciroi

Co-Supervisors:
Dr. Emilia Järvelä

Dr. Marco Berton

Academic year 2021-2022

ABSTRACT

The environment in which the AGN live is linked to many characteristics of the AGN itself. Indeed, a denser environment could mean more frequent interactions and mergers, which have a direct impact on the structure and the physical properties in both the AGN and host galaxy. Therefore, environmental studies at all the scales are of crucial importance. Marziani et al. (2001) built the so called quasar main sequence (MS), which shows a systematic trend in the observational properties and subdivides sources in different spectral types. The MS was a very important discovery, since it allows us to perform several structures and evolutionary studies. The goal of this thesis is to compare the environments of the sources in the MS, to find any possible relations which can explain the variations of some characteristics of the different spectral types. No study like this has been already published in the literature.

In this thesis I performed a comparison of the environments around a sample of 680 AGN spread as much as possible along the MS. The sample used was selected in Marziani et al. (2013), with redshift inside the range $0.4 \leqslant z \leqslant 0.75$, and taking sources brighter than $\mathrm{mag} = 18.5$ in *g*, *r* or *i* bands. The data used in the present analysis have been acquired in the Pan-STARRS 1 survey, in the five *grizy* bands. Three main selection methods for the companions were used and they were performed at different scales around the sources in the sample. The analysis was performed both visually, on the plots, and using several statistical tests. A correlation between the FWHM(H_β) of the sources in the sample and the number of companions was found at all scales by using the magnitude selection method. Precisely, a positive trend was found, which shows higher number of companions around sources with higher FWHM(H_β). No other relationship was identified, and only a small discrepancy between the i-Kron magnitude in population A and B sources in the sample was found. In the end, I discussed the results obtained in the different cases. Future, deeper studies on larger samples are needed to fully understand the behavior of environment along the quasar MS.

CONTENTS

1 ACTIVE GALACTIC NUCLEI 1
1.1 Introduction . . . 1
1.2 Structure of AGN . . . 2
1.2.1 Size of an AGN . . . 6
1.3 Taxonomy and unification . . . 7
1.4 Quasar main sequence . . . 11
1.4.1 Principal component analysis . . . 12
1.4.2 Eigenvector 1 parameter space . . . 13
1.5 AGN environment . . . 16
1.5.1 Host galaxies . . . 17
1.5.2 Mergers and interactions . . . 20
1.5.3 Local and large-scale environments . . . 21
1.5.4 Large-scale environmental structures . . . 24
1.6 Objectives . . . 27
2 SAMPLE AND DATA SELECTION 29
2.1 Acquisition of data . . . 29
2.1.1 Sample selection . . . 29
2.1.2 Pan-STARRS survey . . . 29
2.2 Galaxies-stars separation . . . 32
2.3 Selection methods . . . 35
2.3.1 Magnitude selection . . . 35
2.3.2 Photometric redshift selection . . . 36
2.3.3 Density approach . . . 36
2.4 Biases . . . 38
2.5 Statistical tests . . . 39
3 DATA ANALYSIS 41
3.1 Magnitude selection . . . 41
3.2 Photometric redshift selection . . . 42
3.3 Density approach . . . 43
3.3.1 Physical companions . . . 46
3.4 Sample analysis . . . 46
4 RESULTS 47
4.1 Magnitude selection . . . 47
4.2 Photometric redshift selection . . . 51
4.3 Density approach . . . 53
4.3.1 Physical companions . . . 60
4.4 Sample analysis . . . 60
5 SUMMARY AND CONCLUSIONS 61

BIBLIOGRAPHY 65
APPENDIX 77

1 ACTIVE GALACTIC NUCLEI

1.1 INTRODUCTION

Just like most astrophysical objects, active galactic nuclei (AGN) are a relatively recent discovery. Until the early 1800s, the scientists knew only the optical part of the entire electromagnetic spectrum. William Herschel and Johann Ritter were the first to understand the presence, and the importance, of additional bands besides the visible one, which subsequently were called infrared and ultraviolet. One after the other, in a century, all the spectral bands were discovered. In these years also spectroscopy started to have a crucial role in science, mostly in astronomy. With these two important steps forward in the understanding of the electromagnetic radiation, the historical astronomy field started to become the modern astrophysics.

Nevertheless, in that period, the knowledge about the composition of the Universe was not at all clear. Indeed, William Herschel was one of the first people to suggest the presence of extragalactic objects, making a catalogue of more than 5000 nebulae (up to less than one century ago all the extended objects, which scientists thought were inside the Milky Way, galaxies included, were called nebulae). However, the presence of some objects outside our Galaxy was not a simple thing to digest. In late nineteenth and early twentieth century, due to the extremely fast growth of technology, new, more advanced, telescopes allowed more and more precise studies of visible sources. For instance, Vesto Slipher revealed, via redshifted line measurements, that different nebulae had receding velocities with respect to the Milky Way larger than the escape velocity of our Galaxy (Slipher, 1913). Confirmation came in 1920, when Heber Curtis published *"Descriptions of 762 Nebulae and Clusters Photographed with the Crossley Reflector"* (Curtis, 1918), in which he described why these observed objects are galaxies of their own. Also Edwin Hubble, in his incredible work, estimated the distance of M31 (also called Andromeda) using Cepheid stars obtaining a distance of ~285 kpc, three times less then the right value, but enough to confirm the fact that Andromeda really outside of the Milky Way. In 1943 Carl Seyfert, superimposing spectra of six spiral galaxies with stellar spectra, discovered the presence of strong broad emission lines and realized that these emitting sources had to be a different type of galaxies, subsequently named 'Seyfert galaxies' (Seyfert, 1943). In the 30s Karl G. Jansky built the first radio antenna in history, and with a similar device in 1944 Grote Reber detected the first AGN in radio band, precisely Cygnus A at 160 MHz (Reber, 1944). Due to their radio features, and in addition to the fact that the central region is a high-luminosity point-like source, these mysterious objects were called Quasi-Stellar Radio Sources.

Woltjer (1959) pointed out that the observed luminosity inside the central 100 pc required a mass of $\sim 10^8 M_\odot$. The simplest explanation was the presence of a high-mass stellar-size object at the centre of the galaxy, which principally emits due to the accretion of the surrounding gas (Hoyle and Fowler, 1963). The emitting accretion disk was observationally confirmed before understanding the real nature of the central massive object, because the presence of the disk is required to explain some narrow non-variable forbidden lines (Richstone and Schmidt, 1980). The general relativity theory of Einstein (1916) and the hypothesis of the existence of black holes (BHs) was not widely accepted for many years, but when this hypothesis became useful to explain some phenomena like AGN, scientists started to take general relativity in serious consideration. Indeed, a supermassive black hole (SMBH) matches perfectly the characteristics necessary for the central source of an AGN, because it is relatively small compared to its enormous mass (Lynden-Bell, 1969; Salpeter, 1964; Zel'dovich and Novikov, 1964). In more than fifty years, enormous steps forward have been made, but we are still far from a complete understanding of these fascinating objects.

1.2 STRUCTURE OF AGN

Even if AGN are observationally different from each other, we can find a common pattern that is at the basis of all of them (see Fig. 1). The engine of the system is a SMBH, with a mass range from $10^5 M_\odot$ to $10^{10} M_\odot$ (Beckmann and Shrader, 2012). The composition and structure of an SMBH is completely unknown. A parameter associated to the BH mass is the event horizon, defined as the radius beyond which not even photons can escape. If the BH has mass M_{BH}, the horizon is called Schwarzschild radius (R_s)

$$R_s = \frac{2 M_{BH} G}{c^2}, \tag{1}$$

where G is the gravitational constant, and c is the speed of light. A particle which falls inside R_s is forced to have a geodesic motion and its only fate is to reach the BH singularity. Up to some hundreds R_s outside the event horizon there is an accretion disk. The structure is composed of plasma that orbits the BH. The motion of the gas particles is almost circular, with a minimum distance that can be reached called innermost stable circular orbit (ISCO). Considering a Schwarzschild solution for the general relativity space-time in the case of a spherical symmetric object, the ISCO has a value of

$$R_{ISCO} = 3 R_s. \tag{2}$$

If we take a generic particle which is at rest at infinity, and starts from there its motion towards the BH, considering the energy lost by the particle, the efficiency η is $\sim 6\%$ (Fabian and Lasenby, 2019). Such an efficiency is more than ten times that of the nuclear burning efficiency of a star.

The disk temperature is due to viscous friction between layers of plasma at different radii, that emit electromagnetic radiation. The plasma has a disk-like

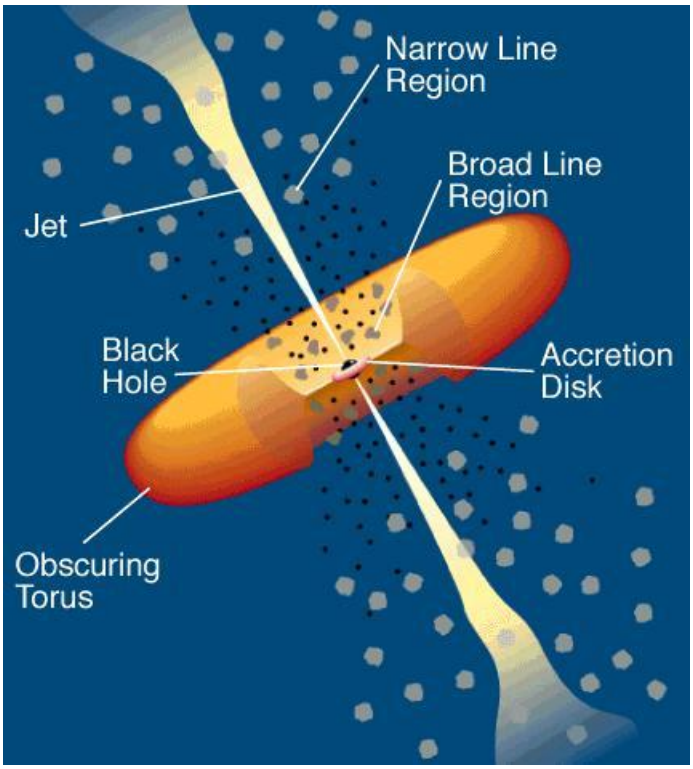

Figure 1: Basic structure of an AGN (Urry and Padovani, 1995).

structure due to its angular momentum, which is transported locally from the inside to the outside by the meso-scale eddies inside the layers. Then inner layers have higher velocities, resulting in an increase of the friction and higher temperatures with respect to the farthest layers ($T \propto R^{-3/4}$, Beckmann and Shrader, 2012). This indicates that there is a gradient in temperature along the radial direction in the disk, which influences the continuum emission. It is well known that an object with a uniform temperature emits like a blackbody (the so-called thermal emission). If we consider different radial layers of the accretion disk, with a temperature gradient, we obtain a superposition of blackbody emission profiles. The result is the so-called *multi-colour blackbody* (Fig. 2), which is a composition of three different blackbody approximations. In the low-energy range the Rayleigh-Jeans spectrum is dominant with a slope of ν^2, in the high energy the Wien tail that has an exponential cut-off like $\nu^3 e^{-\frac{h\nu}{kT}}$ is present, and in the middle range of energy there is a trend typical of multi-colour spectrum which follows $\nu^{1/3}$. Beside the optical range the spectrum assumes different shapes due to several radiative processes, from the radio band up to the X-rays.

The total luminosity of the spectrum is

$$L_{bol} = \eta \dot{M} c^2, \tag{3}$$

where $\dot{M}$ is the mass accretion rate. If we consider a spherical accretion mechanism (Bondi-Hoyle accretion model), from the continuity equation, the mass accretion rate is

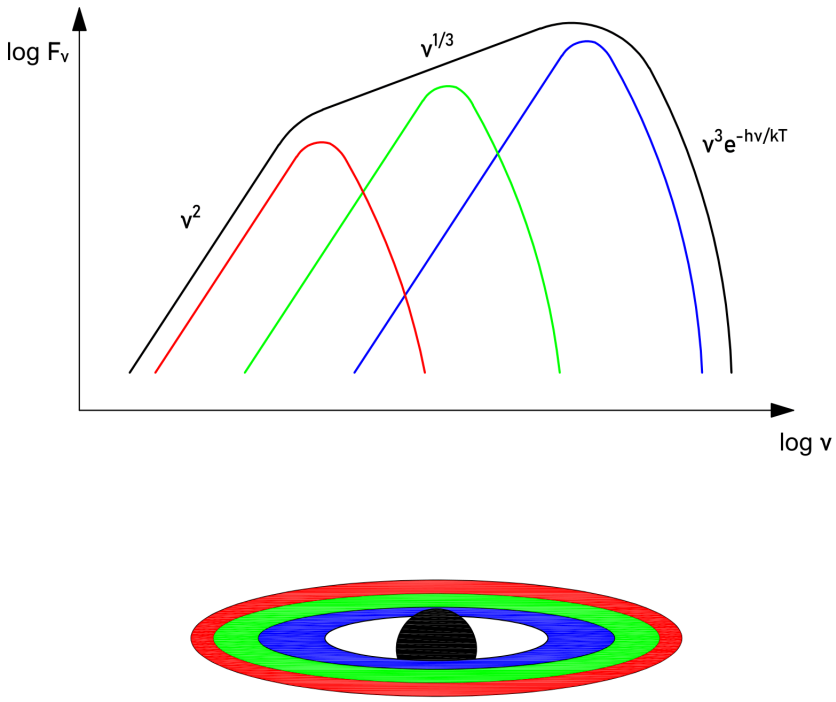

Figure 2: Representation of a *multi-colour blackbody* as a result of superposition of blackbody curves, derived from different rings at increasing temperature in the accretion disk.

$$\dot{M} = 4\pi r^2 \rho(r)\, u(r) = \frac{4\pi\rho G^2 M_{BH}^2}{v^3}, \tag{4}$$

where ρ is the gas density and u the radial velocity of the gas, both evaluated at radius r, and $V = \sqrt{2GM_{BH}/R}$ is the escape velocity at distance R. In Eq. 4 $\dot{M}$ is a constant value through all the radii in the accretion disk. Nevertheless, in this model, the gas falls toward the BH with a radial motion, and it has not enough time to heat up and produce thermal energy before passing the event horizon. However, this is not what we observe, since the accreting material is heated in the infall process. Angular momentum is necessary to increase the radiative timescale. We set a limit, always for a spheroidal system, for the maximum luminosity achievable which is called *Eddington luminosity*

$$L_{Edd} = \dot{M}_{Edd}\, c^2 = \eta\, \dot{M}_{crit}\, c^2 = \frac{4\pi G\, M\, m_p\, c}{\sigma_T} \simeq 1.3 \times 10^{38} \frac{M}{M_\odot}\, erg\, s^{-1}, \tag{5}$$

where $\dot{M}_{Edd}$ is the Eddington accretion rate, $\dot{M}_{crit}$ is the critical accretion rate, m_p is the mass of a particle and $\sigma_T \simeq 6.65 \times 10^{-25} cm^{-2}$ the Thomson cross-section. The Eddington accretion rate is defined as $\dot{M}_{Edd} = \dot{M}(\eta = 1)$, instead the critical accretion rate is the maximum value of $\dot{M}$ to maintain hydrostatic equilibrium. Of course, the maximum value for Eddington accretion rate is set for a spherical object. However, in astrophysical cases the emitter has a disk shape, and super-Eddington accretion ($L > L_{Edd}$) is possible.

A number of models have been used throughout the years to describe the physical properties of accretion disks. The most common and famous one is the Shakura-Sunyaev disk (SSD), also called standard disk (Shakura and Sunyaev, 1976), in which the disk is geometrically thin and optically thick. In the case of a sub-Eddington accretion rate and a very low opacity, the disk has a very low brightness because the energy derived from the warm up is captured by the matter (advection) instead of emitted as radiation. In cases like this the SSD model is no longer suitable and the advection-dominated accretion flow (ADAF) model has been introduced (Narayan and Yi, 1994). Obviously the two disk models mentioned above cannot explain the whole spectral energy distribution (SED) of all AGN accretion disks. For instance, in the SED we find a Big Blue Bump (BBB) (Richstone and Schmidt, 1980), which is an excess in the blue part of the spectrum which was one of the first evidence of the existence of the accretion disk. This feature often cannot be reproduced by neither the SSD nor the ADAF model. To create a hybrid disk model for high Eddington ratio sources, that is sources where the ratio between bolometric luminosity and Eddington luminosity is high, the slim disk has been introduced, with a disk-like geometry but a non-negligible amount of advection (Abramowicz et al., 1988; Mineshige et al., 2000; Szuszkiewicz, Malkan, and Abramowicz, 1996).

Independently from the disk model adopted, the radiation emitted from the central engine ionises the surrounding region of gas, called broad-line region (BLR), which has a density of $\rho \sim 10^9 \mathrm{cm}^{-3}$, and an effective temperature of $\sim 10^4 \mathrm{K}$ (Beckmann and Shrader, 2012). This region is very close to the central BH ($0.01 - 0.5\,\mathrm{pc}$), and it is assumed to be in photoionisation equilibrium, meaning that the rate of ionisation is balanced by the rate of recombination. The gas particles inside the BLR have a wide range of orbital velocities ($10^3 - 10^4$ km s^{-1}), due to the strong gravitational potential induced by the small distance from the BH. Such a range in velocities generates a Doppler broadening in the permitted emission lines. An important relation between AGN nuclear emission and the BLR was discovered by Baldwin (1977). He found a correlation between the equivalent width (EW) of C IV λ1549Å and the monochromatic luminosity of the continuum at $\lambda = 1450$Å, with the relation

$$\log EW(\mathrm{C\,IV}) = -K \log L_{1450\text{Å}} + \mathrm{const.} \tag{6}$$

Nowadays this correlation has been proven for different emission lines, like Lyα, [C III] λ1908Å and Mg II λ2798Å, and is commonly called *Baldwin effect*. With spectra we can retrieve a lot of information about the BLR, however, its precise geometry is still unknown. Recent works divide the BLR in two parts, the very broad-line region (VBLR) which is the closest one to the BH, and the intermediate-line region (ILR; Adhikari et al., 2018; Hu et al., 2008; Zhu, Zhang, and Tang, 2009), farther than the previous one, and that extends up to the narrow-line region (NLR).

On the disk plane, from 10 to 100 pc, there is a toroidal optically-thick region of dust and molecular clouds. When the angle of the line of sight is large,

the inner region is completely obscured by the torus in the optical band, and its emission is absorbed by the torus and re-emitted in the infrared band. Far beyond ~100pc in polar direction lives the NLR. It is composed of low-density ionised gas ($\rho \sim 10^4 cm^{-3}$) which moves at low velocities (10^2 km s^{-1}). Also in this case the ionisation is due to the continuum derived from the accretion disk emission, that generates the forbidden and permitted lines in the spectra. In some cases we can find an extended narrow-line region (ENLR; Cracco et al., 2011), that can reach up to several kiloparsecs, with a bi-conical shape along the dusty torus axis.

One of the most notable features which distinguishes some types of AGN is the presence of relativistic jets perpendicular to the accretion disk plane. The first evidence of an extremely powerful emission from an astrophysical source was found in M87 (Curtis, 1918). The bipolar shape of a jet arises when part of the ionised plasma, during its falling towards the BH, interacts with the intense magnetic field lines close to the BH (Blandford and Znajek, 1977). Due to the axisymmetry of the system, the particles are accelerated in both polar directions. The acceleration's intensity depends on the strength of the magnetic field, the BH spin and size, and, of course, the quantity of the infalling material connected with the density of the surrounding structures (Beckmann and Shrader, 2012). These features define the power and the extension of the jets. Today it is known that only $\sim$ 10% of the AGN harbor jets (Urry and Padovani, 1995), which can terminate rather close to the AGN (few parsec) when they have a low power, or can stay collimated for several kiloparsecs and reach distances of the order of megaparsecs (Mpc-scale jets).

Finally, in AGN the presence or lack of jets is not directly related with the radio loudness parameter, R[1], (originally used for morphological classification, I will discuss this in detail in the next paragraph). Indeed, jets with similar behaviour are present in AGN with different R (Beckmann and Shrader, 2012). Basically, the features that are used to calculate the radio loudness, do not define the presence of jets.

1.2.1 *Size of an AGN*

I briefly examined what we know about the size of the different AGN components in the last paragraph. Such a clear subdivision, however, does not have a straightforward correspondence in reality. Considering the central engine of the system, the BH, as seen in Eq. 1 the effective radius is the Schwarzschild radius, which depends only on the BH mass. Paradoxically, the only component that is not visible, is the only for which it is possible to retrieve a precise estimate. Indeed, there are several methods to measure the mass of a BH (e.g., reverberation mapping, see Peterson and Horne (2004) for a complete discussion). Once the mass has been obtained, the approximate size of the Schwarzschild radius is $R_S \sim 0.01 - 10 AU$. Just outside R_S, on the equatorial plane, we find the innermost part of the accretion disk, which is at the R_{ISCO}.

1 Ratio between radio flux density at 5 GHz (S_R) and optical flux density in B-band at $\lambda = 4400$Å (S_O) (Kellermann et al., 1989).

Its distance from the centre depends on the characteristics of the BH. Indeed, we have different solutions for R_{ISCO} if the BH is rotating or not (Kerr and Schwarzschild solutions, respectively), and if the accretion disk and the BH are co- or counter-rotating. Accounting for all of this, the R_{ISCO} can vary between 1.2-6R_S, and its physical size becomes $R_{ISCO} \sim 0.01 - 60AU$. The outer radius of the accretion disk is also determinable using the BH mass. However, it is not based on theory, but on an empirical formula. Morgan et al. (2010) found, via microlensing analysis, a relation between the outermost radius of the accretion disk visible at $\lambda = 2500$Å and the BH mass

$$\log(R_{2500Å}/cm) \simeq 15.8 + 0.8\log(M_{BH}/10^9 M_\odot). \quad (7)$$

Using Eq. 7 its approximate value is $R_{out} \sim 1 - 1000AU$.

Although the scale of BLR is retrievable with the reverberation mapping cited above, it is not so straightforward to obtain an exact size. We already saw that the BLR starts very close to the central engine. At the same time, we know there is not a definite border between the BLR and the NLR, and that the two regions, even if they exhibit different features, are similar at least in their general structure. Comparing Hubble Space Telescope (HST) and spectroscopic observations, Bennert et al. (2004) found several relations for the BLR and NLR size. They found, for BLR $R_{BLR} \propto L^{0.6}$, and they distinguish NLR size for Type 1 AGN $R_{NLR,1} \propto L_{[OIII]}^{0.55\pm0.05}$, and for Type 2 AGN $R_{NLR,2} \propto L_{[OIII]}^{0.32\pm0.05}$. In addition, they defined a relation between the two region $R_{BLR} \propto R_{NLR,1}^{0.88\pm0.1}$. Following such relations the approximate size of BLR is $R_{BLR} \sim 0.01 - 1pc$, and of NLR is $R_{NLR} \sim 10^2 - 10^4 pc$. Time delay is a technique commonly used to retrieve the size of the molecular torus. Using this method the size obtained is of the order of parsecs. In addition, interferometric measurements with long baseline were made (Kishimoto et al., 2011), but the results are hard to obtain because of the geometry of the torus and the complexity of the interferometry. New technological capabilities will improve, in the next years, our estimation techniques. The only feature clearly visible at great distances is the jet, which can reach up to $\sim 10^2 kpc$, and even more in some particularly powerful cases. To analyse its characteristics radio images are required.

1.3 TAXONOMY AND UNIFICATION

During the years several attempts were made to make a complete AGN classification. The main problem is that each source has characteristics that distinguish it from other, so is not simple to define a complete and exhaustive model.

Since the discovery of different AGN types, radio emission was clearly an important feature that had to be considered. Indeed, the first distinction was made using radio loudness, basically the radio-to-optical flux density ratio, used by Sandage (1965) to prove that most of AGN are radio-quiet ($R < 10$) instead than radio-loud ($R > 10$). This result was confirmed in subsequent

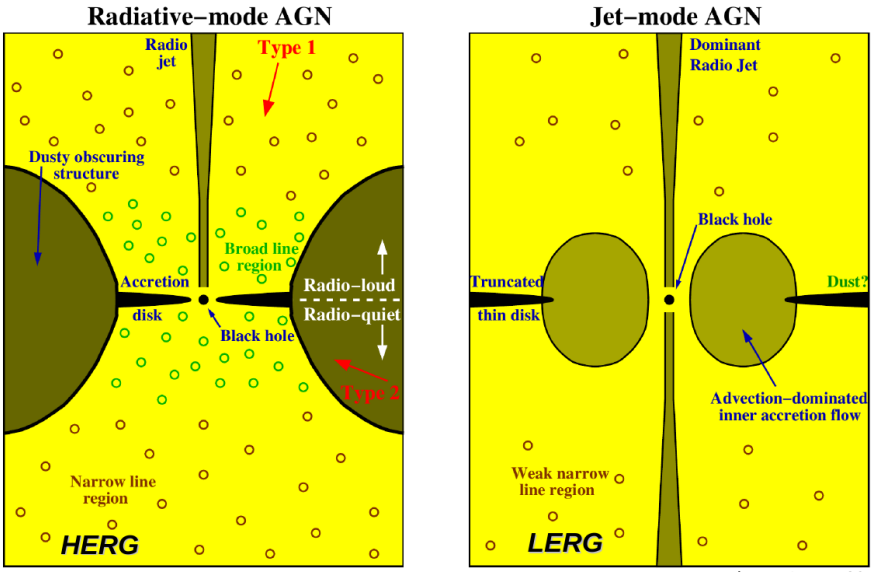

Figure 3: Radiative-mode and jet-mode AGN classification (Heckman and Best, 2014).

years (Kellermann et al., 1989; Miller, Peacock, and Mead, 1990; Strittmatter et al., 1980). At the beginning, the two categories were identified as sources with and without jets (Hutchings, Janson, and Neff, 1989; Wilson and Colbert, 1995), but, as said above, the parameter R does not really predict the presence of jets, except in some particular extreme cases.

Using only parameter R as a yardstick, it is clear that we should have a bimodal distribution. Nevertheless, two classes defined based only one observational parameter are not enough to describe all the AGN populations (Cirasuolo et al., 2003; Zamfir, Sulentic, and Marziani, 2008). One physical property used is the presence or not of the jets, which divides AGN into two subclasses, jetted and non jetted. This distinction is at the basis of the model made by Padovani (2017), which classifies the radio loudness parameter as obsolete and unreliable.

Heckman and Best (2014) divided AGN into two distinct populations, which are radiative-mode and jet-mode AGN (Fig. 3), performing a low-redshift large survey of the Universe. The radiative-mode population is associated with slightly less massive BHs growing in high-density pseudo-bulges, and produces energy powered by accretion close to the Eddington limit. The circumnuclear environment contains high-density cold gas which is associated to the on-going star formation. In the jet-mode population most of the energy extracted from the accretion process produces collimated outflows, like jets. This population is associated with the more massive BHs which usually reside in massive elliptical galaxies. Such BHs are probably fueled by the accretion of slowly cooling hot gas, with a very low efficiency accretion mechanism. Star formation in jet-mode AGN is either missing or very inefficient. In some cases, radiative-mode AGN can also harbor relativistic jets.

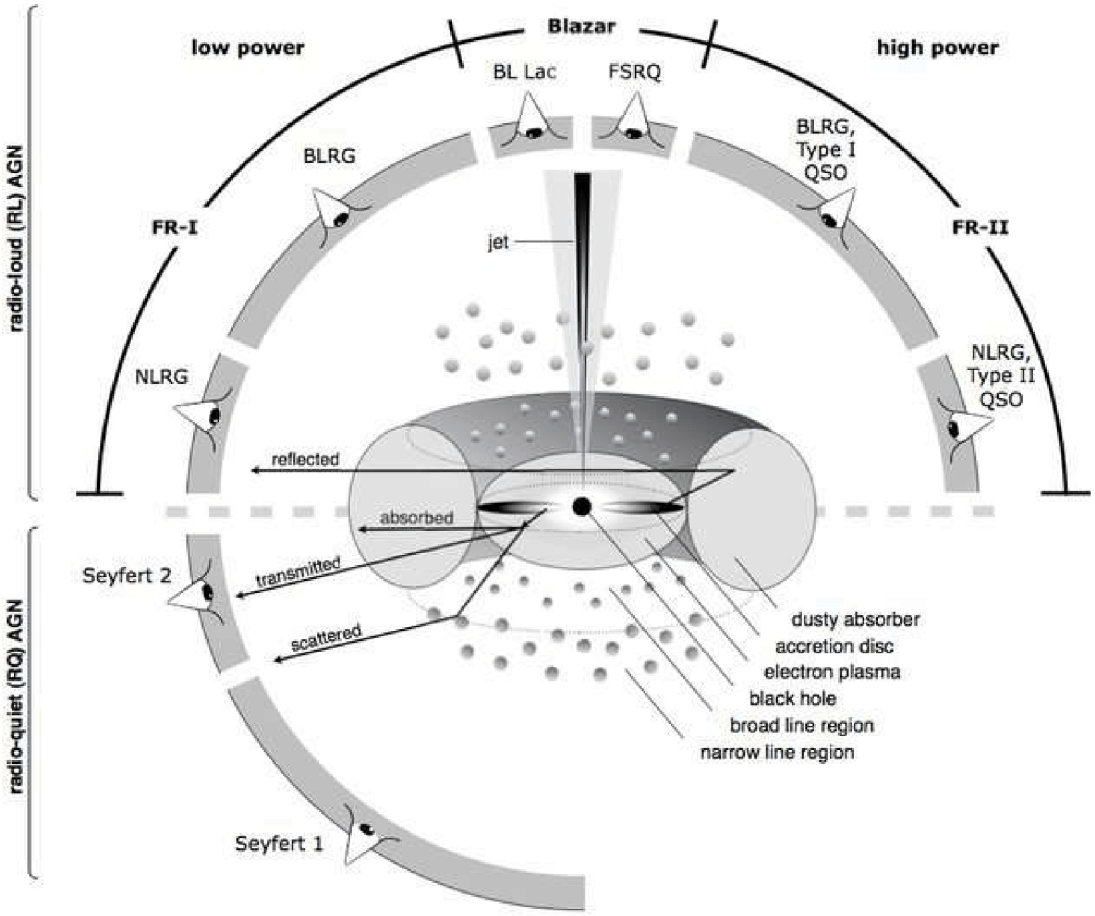

Figure 4: Unified model based on orientation feature (Beckmann and Shrader, 2012).

Obscuration of the inner region by the molecular torus was first proposed by Antonucci and Miller (1985) as the principal element of the unified model (subsequently explained in detail in Antonucci (1993), and further confirmed in Urry and Padovani (1995)). This means that, operationally, the different AGN are classified based on the inclination of their symmetry axis respect to the line of sight. A comprehensive scheme about orientation-based model is shown in (Figure 4).

The observable characteristics of the inner region does not seems to vary also seeing the AGN under different inclination angles. Nevertheless, since the only structure which can absorb the radiation emitted by the central engine is the molecular torus, the incoming spectrum depends on how much it obscures the central engine. Obviously the torus' edges are not a defined surface, so the spectrum does not changes sharply. If we see an AGN edge-on, beside the decrease in luminosity due to the obscuration of the accretion disk, the BLR emission lines are also obscured. In conclusion, regardless of whether jets are present or not, Type 1 are those AGN where all the components are visible,

and the spectrum shows both narrow and broad lines, instead in Type 2 the BLR is completely obscured and the spectrum shows only narrow lines.

Seyfert galaxies frequently, but not exclusively, reside in disk-like host galaxies (Penston et al., 1974; Weedman, 1973). In the optical spectrum they show Balmer emission lines and narrow forbidden lines, like [O II] λ3727, [O III] λλ4959, 5007, [N II] λλ6548, 6583, [S II] λλ6716, 6731, and many others. The emitted spectrum is a combination of the host galaxy and AGN emission. Due to the inclination, the spectrum of Seyfert 1 is brighter compared to the spectrum of its host galaxy. Instead, the spectrum of Seyfert 2 galaxies have a brightness similar to that of its host galaxy. From the X-ray point of view, Seyfert 1 are those sources with an intrinsic hydrogen column density (N_H) $N_H < 10^{-22} cm^{-2}$, while Seyfert 2 have an $N_H > 10^{-22} cm^{-2}$.

The structure and optical depth of the obscuring medium are not constant over the time. Indeed, 'variable' Seyfert galaxies have been discovered, that change their emitted spectrum, and whose classification varies accordingly (LaMassa et al., 2015; Penston and Perez, 1984; Yang et al., 2018). There are sources with an optical spectra dominated by emission lines from low ionisation species (like [O I], [N II], [S II]) and faint high-ionisation emission lines, which are called Low-Ionisation Nuclear Emission-line Regions (LINERs). As suggested by their low X-ray luminosity, they are thought to be the link between normal and active galaxies. Their precise role in the unified model is still debated.

In jetted sources, in addition to the characteristics cited for non-jetted AGN, there are of course the characteristics of the jet. Blazars, as show in upper part of Fig. 4, are those sources seen face-on, with the line of sight inside the jet, and are divided into two main classes: BL Lacertae Objects (BL Lac or BLO) and Flat-Spectrum Radio Quasars (FSRQ). Urry and Padovani (1995) divided these two population according to the equivalent width (EW) of the optical emission lines, BL Lacs have $EW \geqslant 5$Å and FSRQ have $EW < 5$Å. In FSRQs the efficient accretion process produces strong emission lines. BL Lacs, on the other hand, have an inefficient accretion mechanism and a subsequent lower luminosity, thus do not show prominent emission lines. At higher inclinations, among sources with high radio luminosity, we distinguish Fanaroff–Riley I (FR-I) and II (FR-II) sources (Fanaroff and Riley, 1974). FR-I have a low-efficiency accretion and a radio emission almost totally produced by the jets. FR-II are brighter sources with an high-efficiency accretion mechanism, and their radio emission is dominated by the radio lobes far away from the inner region. Within both populations there are Type 1 and Type 2 objects, in terms of optical classification. The former are broad-line radio galaxies (BLRGs) and the latter narrow-line radio galaxies (NLRGs). The distinction between BLRGs and NLRGs is based on the inclination of the line of sight. Among jetted AGN, some particular sources are present, which show uncommon behaviour such as a compact morphology with jets scale comparable to the host galaxy size. Among these there are compact steep-spectrum sources (CSS), giga-hertz peaked sources (GPS) and compact flat-spectrum sources (CFS).

We can make another classification among jetted sources, according to some characteristics visible in the optical spectrum. High-Excitation Radio Galaxies (HERGs) are objects which show strong narrow emission lines and some broad-lines, whereas Low-Excitation Radio Galaxies (LERG) have an optical spectrum with very weak or no emission lines. The main difference between these classes is probably the accretion mechanism onto the black hole (Hardcastle, Evans, and Croston, 2006). There is not a clear distinction, but commonly FR-I and BLO tend to be LERG, instead, FR-II and FSRQ tend to be HERG. LERGs are thought to live in red elliptical galaxies, accreting hot gas with a low velocity dispersion and an almost spherical/puffed accretion disk, well described with the ADAF model (Janssen et al., 2012). Due to this quasi-spherical process the accretion mechanism is close to Bondi one (Allen et al., 2006). Instead, HERGs have a more common thin accretion disk and an obscuring torus, as evidenced in Fig. 3. They are frequently hosted in bluer and star-forming galaxies (Butler et al., 2018). The accretion efficiency in LERGs is very low ($L/L_{Edd} \leqslant 1\%$), while it is higher in HERGs ($L/L_{Edd} \sim 1-10\%$).

The classes mentioned so far are the main ones. Nevertheless, there are a lot of smaller subclasses, which differ from each other based on one or few features. For instance, in Type 1 AGN there are Narrow-line Seyfert 1 galaxies (NLS1), first described in Osterbrock and Pogge (1985), which show a Sy1 optical spectrum but with narrower permitted lines ($FWHM(H\beta) < 2000$ km s^{-1}, (Goodrich, 1989)) and slightly larger forbidden lines ([O III] $\lambda 5007/H\beta < 3$). The broadening of the permitted lines is due to the Doppler broadening effect, which depends on how fast the gas rotate around the BH. Narrow lines means a low-rotational gas velocity likely connected with a small BH mass ($10^6 M_\odot < M_{BH} < 10^8 M_\odot$, (Peterson, 2011)). However, their bolometric luminosity is comparable to that of Sy1 galaxies ($10^{10} L_\odot < L_{bol} < 10^{12} L_\odot$), which suggests a very high accretion rate, close to the Eddington limit (Boroson and Green, 1992) or even larger. Conversely to what was expected, some NLS1 ($\sim 7\%$ of total) show a radio excess (Komossa et al., 2006), and they should be classified as radio loud according to the unified model described above. It has been even proven that NLS1 with a particularly high BH mass are more likely to launch powerful relativistic jets and emit γ-ray emission (Järvelä, Lähteenmäki, and León-Tavares, 2015). These exceptions point out the difficulties in create as uniform as possible a taxonomy model. Similar sources are broad-line Seyfert 1 galaxies (BLS1), in which broader optical emission lines are present, and BHs are more massive than in NLS1. Nowadays it is not yet clear if differences in the various morphological types are only due to the orientation, or also to different evolutionary stages.

1.4 QUASAR MAIN SEQUENCE

Our knowledge of physical mechanisms such as accretion processes or jets formation, as well as connections between the observed spectral properties and the physical parameters, made great steps forward in last fifty years. However, some aspects are still poorly or not at all understood. A diagram for AGN sim-

ilar to the Hertzsprung-Russel requires many efforts to be obtained, due to the complexity that AGN have when compared to stars. Indeed, active galaxies have extended anisotropic emissions/absorptions which influences their observational properties. The only way is to do a multivariate analysis, in which a great number of variables are considered. However, finding any correlation among hundreds of variables is almost impossible. To do so, the principal component analysis (PCA) has been used.

1.4.1 *Principal component analysis*

PCA is a computational process in which a change of basis using the principal components of a high quantity of data is performed. When we have a large sample of data, and multiple variables referred to each element of the sample, it is hard to understand whether any correlation is present. Each variable is a dimension in the parameter space and, with a linear combination, it is possible to reduce the total number of dimensions of this space. The first principal component can be defined equivalently as a direction in which the variance of the projected data is maximized. Practically, an orthogonal transformation is performed and the resulting principal components are called eigenvectors (EVs). The number of EVs is equal to the number of starting variables.

The principal benefit of PCA is to identify the dominant variables, or the most important ones, in a dataset. The choice of the variables involved in the analysis must be very careful, because PCA is very sensitive to the properties of the original data sample. Indeed, if two variables are even slightly correlated, the analysis emphasises this connection and it will become the dominant part of the results.

Let us take a look at the analysis from a geometrical point of view. Let us set n as the value of a certain quantity (e.g. sources) and m as variables (e.g. parameters, that for our purpose could be the FHWM, luminosity, intensity of the emission line/continuum etc.). Each object is represented as a vector $\vec{v}$ in a m-dimensional space, which forms a matrix M with n vectors in m-dimensions. The PCA seeks for the best-fit for the orthogonal axis to replace the original one. To do so the Lagrange multiplier λ must be introduced for the calculation of the eigenvalues $M^{\mathsf{T}} M\vec{v} = \lambda\vec{v}$, where M^{T} is the transposed matrix of M. Finally, given the eigenvalues obtained and using the characteristic polynomial, we can obtain the linearly independent (orthogonal) EVs. The EVs which constitute the new basis are called eigenvector 1, 2, 3 (EV1, EV2, EV3) and so on (see Marziani, Dultzin-Hacyan, and Sulentic (2006) for a more exhaustive review). Of course, EVs are all orthogonal to each other, and usually the first few EVs are those used in an analysis.

For instance, let us take a two-dimensional (m=2) plane in which there is a set of points (n) almost aligned in a random direction, so not parallel with the axes. In a physical way we can say that the two variables, in the two axes, are in this case highly correlated. To maximize the projections along one axis, we can perform a change of basis, which is in practice a rotation of the original axes. Now we can rely only on one dimension which contains all the maximum

variance of the data set. A problem treated at the beginning in two-dimensions becomes a one-dimensional analysis. The power of PCA is precisely this: it reduces variables, often in a very large number, to only the essential ones.

1.4.2 *Eigenvector 1 parameter space*

In AGN research, up to early '90, correlation analysis almost always reached confusing results. A prime example is the Baldwin effect, which was found only in a few sample, without any apparent explanation. A fundamental improvement was done by Boroson and Green (1992), with the first PCA applied to the optical properties of a sample of 87 QSO at redshift $z < 0.5$. They found an anticorrelation that dominates the EV1 parameter between the strength of Fe II λ4570, or $R_{Fe\ II}$ (or peak strength of [O III] λ5007) and the FWHM(Hβ). Instead the EV2 was found to be proportional to the optical luminosity and associated with the high-ionisation lines (HILs, like He II λ4686). Similar subsequent studies with different samples (Boroson, 2002; Grupe, 2004; Xu et al., 2012) obtained consistent results, and proposed that the physical mechanism related to EV1 is the Eddington ratio (L_{Bol}/L_{Edd}), while that related to EV2 is the accretion rate (strongly correlated to the BH mass). Another step forward was done in the last 20 years (Marziani, Dultzin-Hacyan, and Sulentic, 2006; Sulentic, Calvani, and Marziani, 2001; Sulentic and Marziani, 2015) with the 4-D Eigenvector 1 (4DE1), which is an extension of EV1 in 4-dimension. The four parameters, showed in Fig. 5, involved in 4DE1 are:

1. The full width half maximum of low-ionisation (broad) lines (LILs) (e.g. FWHM(Hβ)). Hβ is the most used line because it is reasonably strong and visible also at high redshift ($z \sim 1$).

2. The ratio between the equivalent width of Fe II λ4570 and Hβ ($R_{Fe\ II} = EW(Fe\ II\lambda4570)/EW(H\beta)$). The motivation about the use of the EW is its widespread availability in spectra up to $z \sim 0.7$. Recently, the intensity or flux of the two lines was also used to calculate the ratio.

3. The centroid velocity shift of the HIL C IV λ1549 ($C(1/2)_{C\ IV}$).

4. The soft X-ray photon index (Γ_{soft}), which is used to measure the thermal emission in $0.1 - 2.4keV$ range.

When put on the EV1 plot, whose axes are FWHM(Hβ) and $R_{Fe\ II}$, different AGN types form the so called Quasar main sequence (MS) (Fig. 6), defined for Type 1 quasar with luminosity $logL < 47$ [erg s^{-1}], and $z < 0.7$. The MS defined different spectral types, which divide the 4DE1 optical plane in a sort of grid of bins with fixed range of FWHM(Hβ) and $R_{Fe\ II}$. In x-axis taking a bin-size of $\Delta R_{Fe\ II} = 0.5$ spectral types are A1, A2, A3, and A4, with an increasing $R_{Fe\ II}$. The bin-size in y-axis, instead, is $\Delta FWHM(H\beta) = 4000$ km s^{-1}. Moving to higher values we identify sources with broader Hβ, defined as B1, B1+, B1++, and so on. The MS and the different spectral types are

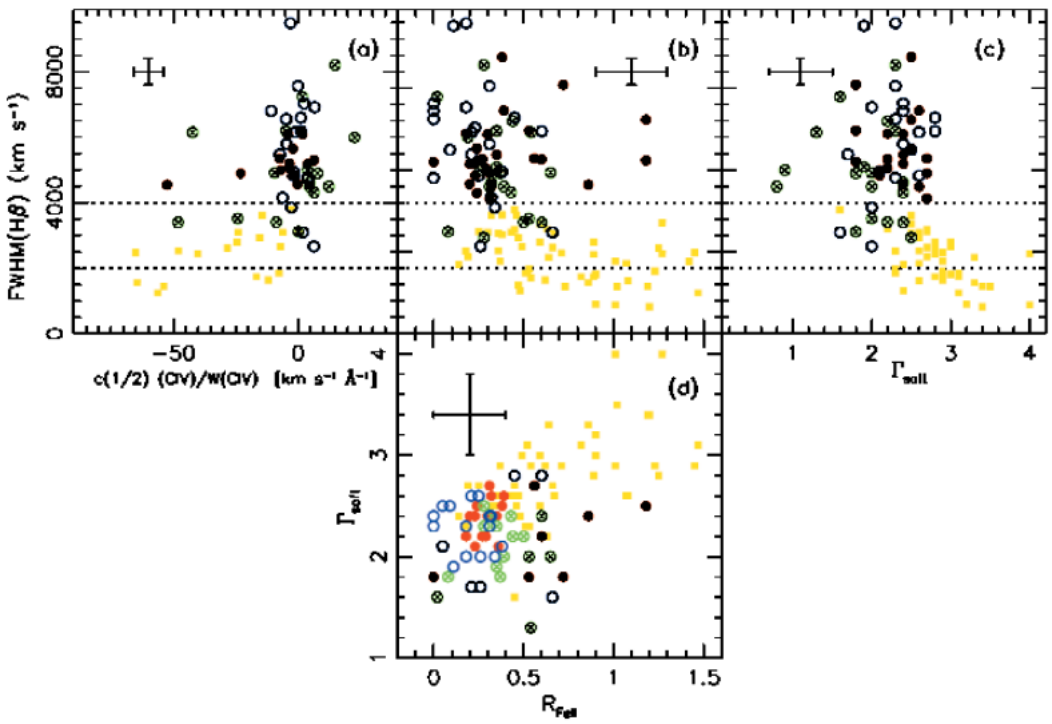

Figure 5: Principal correlation between the 4DE1 parameters space. The central panel (b) shows the optical EV1 plan, basically the quasar main sequence, in which there are RQ population A sources (yellow squares), RQ population B sources (red circles), core-dominated RL (green crossed circles) and lobe-dominated RL (blue open circles) (Sulentic, Calvani, and Marziani, 2001).

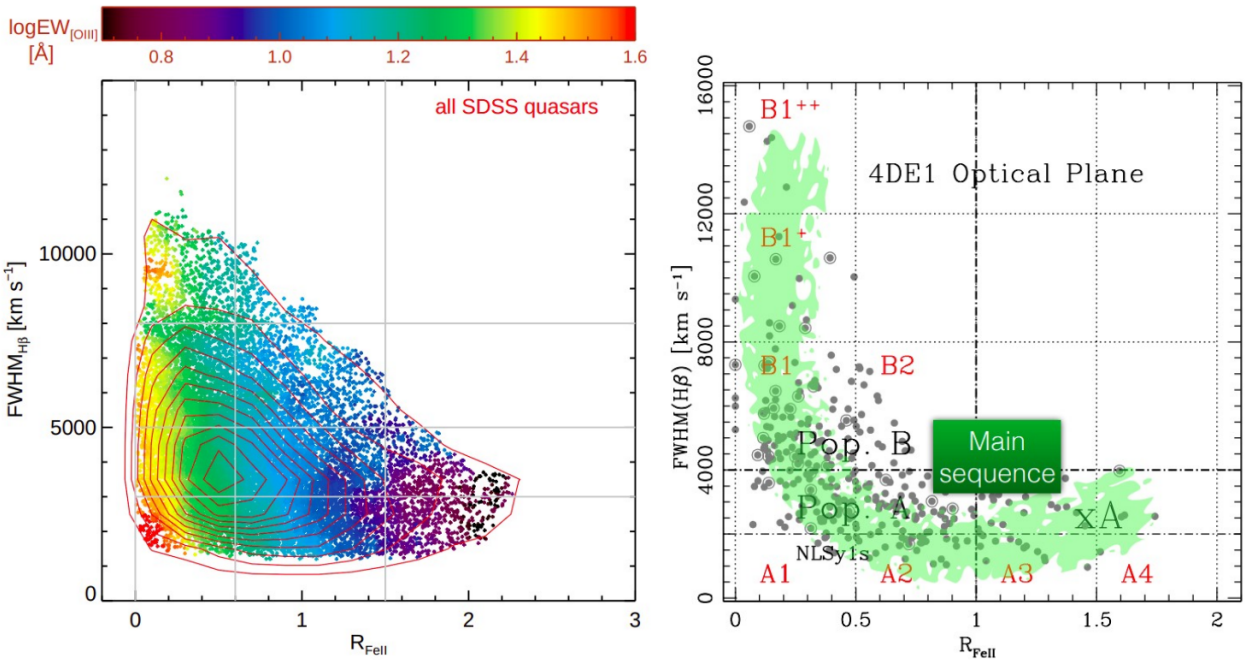

Figure 6: *Left panel*: The EV1 plane distribution of a sample ~ 20 000 quasars, observed in the Sloan Digital Sky Survey data-released 6 (SDSS6). The red contours show the distribution of SDSS quasar sample, and the coloured points show individual objects. The colour-code of the points is referred to [O III] λ5007 strength, averaged over all nearby objects in a smoothing box of $\Delta R_{Fe\ II} = 0.2$ and $\Delta FWHM(H\beta) = 1000$ km s^{-1}. An inverse proportionality between [O III] strength and $R_{Fe\ II}$ has been found (Shen and Ho, 2014). *Right panel*: The optical plane of the 4-D Eigenvector 1, FWHM(Hβ) vs $R_{Fe\ II}$. Thin dotted lines separate the different spectral types. The thick horizontal and vertical dot-dashed lines distinguish population A & B and define the limit of extreme Population A (xA) sources with $R_{Fe\ II} > 1$. Under the thin dot-dashed line live most NLS1s, which have a FWHM(Hβ) < 2000 km s^{-1}. The green shaded area indicatively traces the distribution of a quasar sample from Zamfir et al. (2010), and defines the quasar MS (Marziani et al., 2018).

Table 1: Main population A & B physical features (Fraix-Burnet et al., 2017).

parameter	**pop. A**	**pop. B**
$FWHM(H\beta)$	800-4000 km s^{-1}	4000-10 000 km s^{-1}
$C(1/2)_{CIV}$	-800 km s^{-1}	-250/+70 km s^{-1}
$R_{Fe\ II}$	0.7	0.3
Γ_{soft}	> 2	≈ 2
$C(1/2)_{H\beta}$	~ 0	500 km s^{-1}
Hβ profile shape	Lorentzian	double Gaussian
X-ray variability	extreme common	less common
optical variability	possible	more frequent
$\log M_{BH}[M_\odot]$	6.5 -8 .5	8.0 - 9.5
L/L_{Edd}	$\approx$ 0.2 - 1.0	$\approx$ 0.01 - 0.2

shown in Fig. 6. Obviously, sources with mixed characteristics can be present. For instance, an object that shows a line width of $4000 < FWHM(H\beta) < 8000$ and a strength on iron emission of $0.5 < R_{Fe\ II} < 1$ is classified as B2. Sources that belong to the same spectral type show similar spectroscopic features, such as similar line profiles and line flux ratios, and they are believed to be objects of similar nature. As explained in Marziani et al. (2001), the intrinsic features of sources that composed the MS change in a monotonic way, as the MS shape suggest. Therefore, even if two sources are classified with the same spectral type, minors difference can be present.

Considering the described MS, it is possible to distinguish two different classes, population A and population B. The dividing line is the dot-dashed thick-horizontal line shown in Fig. 6, with a set value $FWHM(H\beta) = 4000$ km s^{-1} (Sulentic, Marziani, and Dultzin-Hacyan, 2000). Population A is defined as those objects with $FWHM(H\beta) < 4000$ km s^{-1}, and population B with $FWHM(H\beta) > 4000$ km s^{-1}. Both the optical and the radio continuum luminosity appear to be uncorrelated with the EV1 parameters. Indeed, there are no similarities between pop.A&B and the radio-loud and radio-quiet classification. As it is clear in the figure, pop.A sources tend to spread in x direction, so they have very different Fe II intensities. Conversely, pop.B objects have in most cases an $R_{Fe\ II} < 0.5$, but a wide range of Hβ FWHM. Furthermore, it was observed that pop.A have a soft X-ray excess which is missing in pop.B. The main features of the two population are summarized in Table 1.

1.5 AGN ENVIRONMENT

AGN, by definition, reside in the centre of their so-called host galaxies. Therefore, studying the environment in which AGN evolve is of crucial importance. The Universe visible today is due to an evolution from the early Universe stages until now. There are two basic scenarios developed in the years which

explain such evolution: the monolithic dissipative collapse, and the hierarchical clustering. The first is based on the fact that the primordial mass distribution was not homogeneous, but it had regions at higher density. These overdensities, due to the small differences in the gravitational potential, started to accrete mass generating proto-galaxies. In this way, several galaxies began to develop and, by accreting even more gas, they started star formation processes. The higher the initial density, the higher the mass of the newly-created galaxy. The second scenario is supported by observations of the large scale structures and by cosmological simulation, so to date it is the favoured one. It assumes that some small galaxies were created in the primordial cosmic fluid, and they subsequently merged together to form more massive galaxies and clusters.

1.5.1 *Host galaxies*

The host galaxy is the closest environment to the AGN, and it is the first supplier of gas of the BH. A constant supply of gas toward the inner region is fundamental to keep the AGN active. Shapes like bars in spiral galaxies are very efficient carriers of material (Sakamoto et al., 1999; van de Ven and Fathi, 2010), much more than in elliptical galaxies, in which there are no tidy motions to feed the BH efficiently. Sometimes, the gas motion triggers nuclear star formation (LaMassa et al., 2013), or even starburst, but more frequently it reduces the star formation activity gradually, leaving an intermediate-age stellar population while the AGN activity goes on for mega-years (Storchi-Bergmann, 2008).

Although a connection is present, strong or weak, between AGN and host galaxy, it has been shown that the ratio between the total stellar mass (M_*) and the BH mass is not constant. At $z \simeq 2$ Trakhtenbrot et al. (2011) found that for BH mass lower than $M_{BH} \simeq 10^8 M_\odot$ the ratio is higher ($M_*/M_{BH} \sim 280$) than for BH mass above $M_{BH} \simeq 10^9 M_\odot$, in which $M_*/M_{BH} \sim 40$. This means that, although more massive BH are likely to reside in larger host galaxies, the M_*/M_{BH} ratio is not a constant parameter. An explanation about the variation on this ratio could be attributed to different evolutionary stages between spiral and elliptical host galaxies, or to different growth timescales which change based on the galaxy types. Moreover, Silk and Rees (1998) found a relation for spirals that connects the velocity dispersion of the bulge and the BH mass, while for ellipticals it relates the velocity dispersion of the spheroid and the total stellar mass. We will describe in the following a short derivation of this relation (for an exhaustive discussion see (Fabian, 2010)). When the AGN core accretes close to the Eddington limit, the radiation pressure drives away a fraction of the mass of gas in the bulge ($f M_{bulge}$), isotropically at radius R. In a stationary state the force from time-averaged luminosity (L_{Edd}/c, due to radiation pressure) is balanced to the gravitational force.

$$\frac{L_{Edd}}{c} = \frac{G\, M_{bulge}\, f M_{bulge}}{R^2}. \tag{8}$$

To replace the Eddington luminosity in the left hand side we can use Eq. 5. Assuming that the bulge can be represented by an isothermal sphere, the mass inside the radius R is a function of the velocity dispersion of the gas σ

$$M(<R) = \frac{2R\sigma^2}{G} \quad \Longrightarrow \quad \frac{M_{bulge}}{R} = \frac{2\sigma^2}{G}. \tag{9}$$

Using this, Eq. 8 becomes

$$\frac{4\pi G\, M_{BH} m_p}{\sigma_T} = G\, f \left(\frac{2\sigma^2}{G}\right)^2. \tag{10}$$

Therefore, the BH mass is

$$M_{BH} = \frac{f\, \sigma^4 \sigma_T}{\pi G^2 m_p} \quad \Longrightarrow \quad M_{BH} \propto \sigma^4. \tag{11}$$

An $f \simeq 0.1$ gives realistic results. A relation similar to the $M - \sigma$ was obtained by Faber and Jackson (1976) between the luminosity and the velocity dispersion at the centre of elliptical galaxies, which is called Faber-Jackson relation: $L \propto \sigma_o^4$. This relation, as mentioned before and pointed out by Murray, Quataert, and Thompson (2005), is quite similar to Eq. 11, and it determines the maximum luminosity above which the activity in the central region drives away an important fraction of gas, inhibiting the accretion process onto the bulge. An extended form of the Faber-Jackson relation is

$$L \simeq \frac{4\, f\, c\, \sigma_o^4}{G}. \tag{12}$$

It was shown that using $f \simeq 0.1$ for Eq. 11 and Eq. 12, and assuming a linear correlation between M_{BH} and M_{bulge}, both formulas well describe an AGN. It has been found that luminous AGN host, on average, have larger BHs, and that there is a trend for spheroidal host galaxies in which they become more frequent when AGN luminosity increase (Dunlop et al., 2003).

Particular attention must be paid when the same AGN populations at different redshift are studied. For instance, flux-limited observations detect only high-luminous objects at high-redshift, while at low-redshift also fainter sources are detectable. In addition to this, some structures or dynamical properties can be resolved only in the local Universe, and not at high z. The quantities involved in the aforementioned relations, taken in $\log$ scale, are linear correlated at low-redshift (Lauer et al., 2007). If some discrepancies are present, when same population at different z are examined, these can be translated in an offset of the quantities from the linear relation. Other selection effects are discussed in Schulze and Wisotzki (2011), and one of them is the cosmic downsizing.

As I mentioned at the beginning of this paragraph, the hierarchical clustering model hypothesises that smaller-mass objects are formed first, and then they merge with each other to form massive galaxies. This explains why at high redshift we observe sources with smaller mass, and why clusters are abundant only at $z < 1$. However, some contradictions were also discovered. It is well known that in the local Universe massive galaxies evolve in passive mode, and

they contain the oldest population stars. In turn, star forming galaxies are those with low or intermediate masses. This means that at higher redshift massive galaxies should be formed before less massive ones. However, this is completely in contradiction with the cosmic model. Additionally, a similar kind of discrepancy is present also when referring strictly to AGN evolution. Several studies were made on quasar evolution (e.g. Barger et al., 2005; Brown et al., 2006; Croom et al., 2009; Richards et al., 2006; Schmidt, 1968), and to build their luminosity function (LF, also called Schechter luminosity function (Schechter, 1976)). The LF represents the number of sources at a specific luminosity in a volume, and it can be analysed also at different redshift. The AGN luminosity is correlated with their activity state. Therefore, analyse the variation of the LF at different redshift means understand which is the AGN activity at such redshift. This kind of technique is not simple. To obtain comparable results, data for different AGN types at different redshift are needed, but they must be taken at same wavelengths. Therefore, the main problem is the choice of the observed energy band. There is not a correct solution, since any band can be a good choice in some circumstances and bad in other. For instance, in the radio band radio-loud quasars are very visible, but a fraction of Seyfert galaxies are missed. In optical all the absorbed Type 2 AGN are lost. On the other hand, X-rays are good tracers of AGN activity, especially at high redshift, because they are less affected by absorption. However, by using X-rays observation it is not simple retrieve the redshift, and it is still necessary to rely on optical and infrared observations to obtain this piece of information. Observations in several bands have been used to find the best solutions, and the results are pretty consistent with each other. From the LF analysis, it was found that bright quasars are dominant at higher redshift ($z > 2$), while faint AGN predominate in local Universe ($z < 1$), according to the aforementioned cosmic downsizing. The apparent paradox between hierarchical clustering and cosmic downsizing is not necessarily real. Old stellar populations do not mean old galaxy. In fact, some mechanisms which, for instance, increase the evolutionary pace in massive galaxies could be present. Some studies suggest that the BH is one of the controller of the star forming activity (see Schneider (2006) for an extended review). The BH can affect the host galaxy via different feedback mechanisms like radiation pressure, winds, jets, and outflows in general. An important thing to notice is that feedback is stronger in jetted compared to non-jetted AGN (Järvelä, 2018). Two feedback modes have been identified, quasar-mode and radio-mode, that depend on the AGN accretion mechanism. Quasar-mode works principally via radiation pressure and winds; it can enhance the star formation, but also suppress it (Ishibashi and Fabian, 2012; Pović et al., 2012). In radio-mode, the jet is the responsible of the feedback; jets can increase the temperature of the gas in the galaxy via shocks, inhibiting the star formation activity (Fabian et al., 2013).

1.5.2 *Mergers and interactions*

Understanding the dynamics behind mergers and interactions is a crucial point, because such phenomena could be the main responsible for changes in the host galaxy morphology and in the AGN activity. I have to do a first classification of merging events. Major mergers occur when the interacting galaxies have approximately equal mass. During this process a dynamical heating of the gas takes place, with the subsequent formation, in most of the case, of an elliptical galaxy with little to no star formation. Minor mergers, instead, occur when the ratio between the mass of the two interactive galaxies is in the range $m_1/m_2 = 0.1 - 0.5$. In this case, if the more massive galaxy is a spiral one, the resulting object is often a disk galaxy in which there is an enhancement of star formation because of the new gas supply (Barth et al., 2008; Taniguchi, 1999). Minor mergers are more frequent than major mergers, and often they do not change much the morphology of the more massive galaxy (Lotz et al., 2011). In some cases also major mergers can transport gas and either feed the BH or increase the quantity of gas available to form new stars (Ellison et al., 2011). Urrutia, Lacy, and Becker (2008) proved using 13 HST photometric images how frequently the interaction triggers the activity in quasars. However, sometimes, such strong encounters can strip the galaxy of its gas, quenching the star formation, limiting the supply of gas to the BH, and forming a passively evolving non-active and usually early-type galaxy.

Hopkins et al. (2010) studied, via simulations, how the mergers affect the mass of the bulge. They found that although major mergers dominate the formation of bulges, minor mergers are also relevant, forming a bulge in 30% of the times. Nevertheless, it seems that the merger type depends also on the mass of the system. Indeed, while in high-mass systems the bulge is mainly formed via major mergers, minor mergers seem to dominate in low-mass systems. They point out that the uncertainty in the average major merger rate is still high. This includes the possibility that half of the bulge mass is collected through non-merging activity. Therefore, more sophisticated simulations are needed.

Barnes and Hernquist (1991) showed that the results of major mergers between two spirals with similar mass is an elliptical galaxy, with the creation of a bar in the inner region. As I discussed in the previous paragraph, a bar allows the gas to reduce its angular momentum. This gas then becomes fuel for the central BH. In this phase, cold gas travels to the inner region ($r < 0.5$ kpc), and the hot gas ($T \simeq 10^4$K) forms a sort of "atmosphere", spreading inside the galaxy. Since a bar can have a crucial role in feeding the AGN, one can think that the former involves the latter. An analysis of $\sim 10\,000$ face-on barred galaxies at low redshift ($0.02 < z < 0.05$) was carried out to verify the possible correlation between bars and AGN (Cardamone et al., 2011). It was found that 31% of barred galaxies host an AGN (Gallo et al., 2010). Therefore, if a correlation is present, it is very weak. Again, there is no evidence conclusively proving that merging causes AGN activity.

Dry and wet mergers are two additional classes of mergers. Dry mergers change the gas distribution, neither adding nor removing mass. Early-type galaxies often are involved in dry merging. On the other hand, wet mergers carry a significant amount of cold gas, which can trigger star formation. This often occurs in spiral and irregular galaxies.

How some parameters (SFR, BH accretion rate and BH mass) vary during a major merging between two galaxies, it is shown in Fig. 7, which includes in addition a graphic representation of the merging phase. To obtain these results Di Matteo, Springel, and Hernquist (2005) performed a galaxy-galaxy merger simulation. We can see that in the initial phase the merger leads to an enhancement of AGN activity, because of tidal forces helping a flow of matter toward inner region. The authors pointed out that there might be a "final parsec problem". Assuming that the two galaxies both host a SMBH, the initial high angular momentum can prevent the coalescence, and the resulting merged galaxy harbors a binary SMBH pair. Instead, if the angular momentum is well exchanged with the surrounding mass (stars and gas), after the merging a final SMBH can be produced (Khan, Just, and Merritt, 2011). If this second scenario occurs, an enormous amount of energy is released via gravitational waves.

X-ray bright AGN might be a good indicator of recent merging events. Swift satellite observations of the host galaxy of hard X-ray-selected AGN revealed that the fraction of disturbed and irregular galaxies, as well as the number of hosts with a close companion, is enhanced when compared to a control sample of optically selected AGN (Koss et al., 2010). Since the Swift sample was selected in the local Universe ($z \sim 0.02$), one can conclude that merging and AGN activity might still be linked today. Large and deeper analysis should be carried out to settle the issue of how large the impact of merging on the AGN activity is, and what role minor and major mergers play in it. What is clear is that mergers play crucial role in AGN evolution and morphology, and are strictly connected with the local environment.

Finally, as merging between AGN leads, in some circumstances, to the coalescence of two SMBH, gravitational waves could be the next field that will give us more answers on this problem.

1.5.3 *Local and large-scale environments*

So far it looks clear that most of galaxies' features depend on the galaxy-galaxy interaction. Nevertheless, the number of mergers or interactions that a galaxy undergoes is related to the environment it resides in. To investigate the environment just outside a galaxy, we have to analyse the local and large-scale structure, starting from nearby galaxies, passing through groups and clusters, and then reaching cosmic structures. The evident interaction occurs when a galaxy has a close satellite, so basically when a close pair system is formed. The fraction of galaxies in pair systems is $\sim 1-4\%$ of the total, even if is still unclear whether a dependence on the redshift is present (Fu et al., 2018; Keenan et al., 2014; Man et al., 2012; Robotham et al., 2014). In the local en-

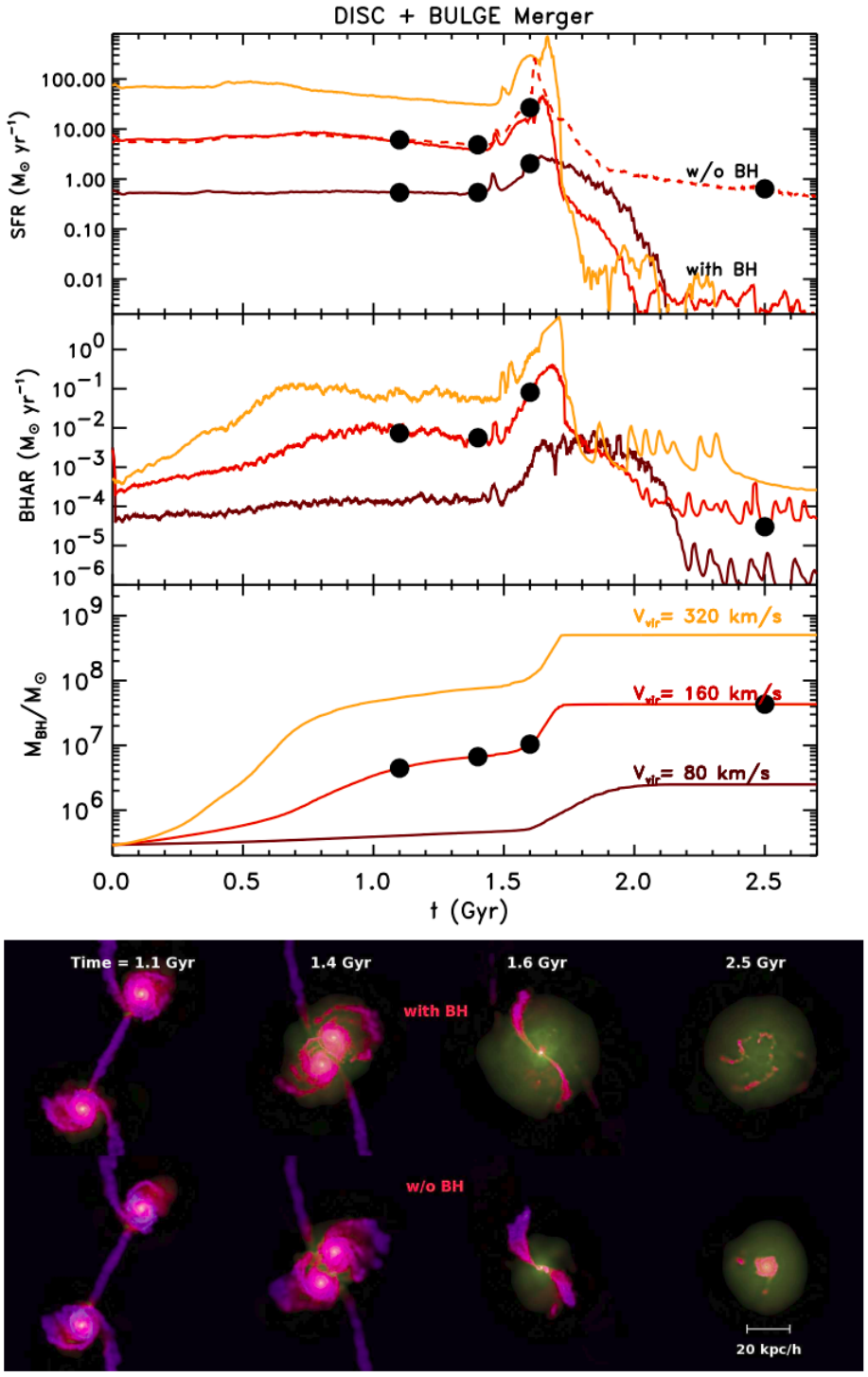

Figure 7: *Top graph*: Star-formation rate (SFR, a), BH accretion rate (BHAR, b) and BH mass (c) versus time for a simulated major merger event. The black dots indicate specific times in merging process. From lower to higher t: first close passage of the two galaxies, tidal interaction just before the merging, coalescence, and conclusion of the merging phase. In this simulation all the star formation is quenched after the merging. *Bottom figure*: Picture referred to galaxy-galaxy merging with (sequence above) and without BH (sequence below) at the centre of each objects. Each frame represents a phase during the merger, from left to right side, and is represented with a black dot in the top panel (Di Matteo, Springel, and Hernquist, 2005).

vironment, the number of satellite galaxies seems to be inversely proportional with the mass of the principal galaxy. Indeed, $\sim$ 15% of massive galaxies ($M_{gal} > 10^{11} M_{\odot}$) have at least one satellite with a mass of 10% of the mass of the principal galaxy, and $\sim$ 30% a satellite with a mass of 1% of the primary. Usually there is more than one galaxy in the neighborhood, especially if the differences in mass are relevant. On average early-type galaxies have two or three times more chances of having satellites than late-type galaxies, and then minor interactions are more common (Mármol-Queraltó et al., 2012). A galaxy in general undergoes ~ 1 major merger at $z < 3$, and $0.2 - 0.8$ mergers at $z < 1$. Obviously, the number of interactions depends on the density of the environment in which the galaxy resides in. If the local environment density increases, the fraction of non-isolated galaxies increases as well (Ideue et al., 2009).

Galaxy clusters are very large groups of galaxies which are relatively close each other because they are gravitationally bound. They can contain up to ~ 1000 galaxies, but already groups of $30 - 300$ members are considered rich clusters with a radius of $1 - 2\,h^{-1}\,Mpc$ ([2]). Groups and poor clusters have on average $3 - 30$ galaxies (our Local Group has ~ 50 members) and a radius of $0.1 - 1\,h^{-1}\,Mpc$ (Bahcall, 1996). Many, but not all, galaxy clusters have a very massive galaxy at the centre. Such galaxy is called central dominant (cD) galaxy, which is usually a red early-type galaxy, and in some cases it hosts an AGN like M87 in the Virgo cluster. Only $\sim$ 5% of galaxies in the Universe reside in rich clusters, $\sim$ 55% are in groups, $<$ 40% are singular field galaxies, and the few remaining are in pair systems. As I said, the denser the environment, as in groups and clusters, the higher is the probability of interaction. A consequence is that early-type galaxies are more often found in clusters than late-types, and a relation between the cluster-scale environment and the galaxy morphology has been found (Chen et al., 2017; Dressler, 1980; Hubble and Humason, 1931; Park and Choi, 2009). The speed at which late-type galaxies are transformed in early-types depends on how dense the local environment is. A single galaxy can also interacts with a cluster, and due to ram-pressure stripping and tidal forces, it may lose part or all of the gas, becoming a red-inactive galaxy whose star formation is totally quenched (Ebeling, Stephenson, and Edge, 2014; Steinhauser, Schindler, and Springel, 2016).

In the larger picture of the Universe, galaxies are not uniformly distributed. In some regions the concentration of mass is higher than the average, like in superclusters and filaments, or lower, like in voids. Each of these regions have different shapes. The set of structures which compose the cosmos is called cosmic web (see next paragraph). In this framework, superclusters are an ensemble of galaxy clusters and groups, and have a size of $10 - 100\,Mpc$. In some cases, due to this very large distances, the expansion of the Universe overcomes the gravitational attraction, moving away different gravitationally-bounded groups. Similar properties to those in clusters have been found also

2 *h* is the *dimensionless Hubble constant* which must be used to consider Universe expansion. It arises from Hubble's formula $H_0 = 100h$ km $s^{-1} Mpc^{-1}$ and has a value $h \sim 0.7$ (Croton, 2013).

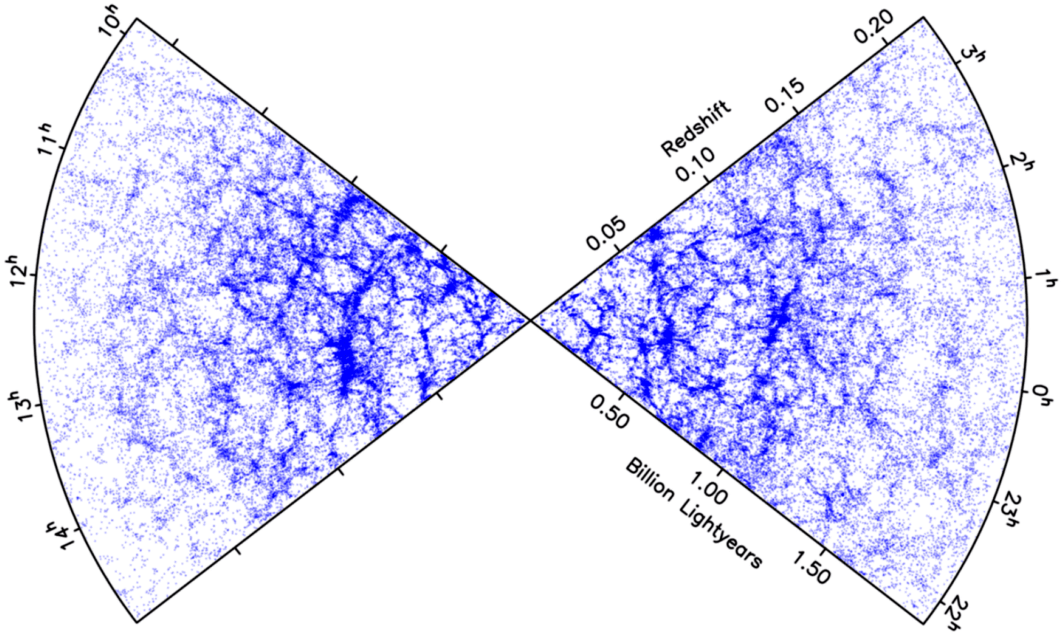

Figure 8: Two-dimensional image from Two-degree-Field Galaxy Redshift Survey (2dFGRS). This survey has been performed between 1997 and 2002 by Australian Astronomical Observatory with the 3.9m Anglo-Australian Telescope. The field observed by the survey is about 1500 square degrees and the volume is about $10^8 h^{-1}\,Mpc^3$. In total were found 382 323 objects (The Royal Observatory, Edinburgh).

in large-scale environments: a spheroid morphology is more common in superclusters and filaments, whereas late-type galaxies increase in sub-dense regions (Chen et al., 2017; Einasto et al., 2014; Kuutma, Tamm, and Tempel, 2017; Lietzen et al., 2012; Pandey and Sarkar, 2017). In addition, large-scale environment density influences the properties of galaxy groups, and then indirectly also the evolution of their galaxies (Poudel et al., 2017). Many studies were carried out to investigate how the environment affects the different aspects of certain AGN types. For instance, Krongold, Dultzin-Hacyan, and Marziani (2001) investigated the local environment of samples of Sy2, NLS1, and BLS1 galaxies, mapping their neighbour galaxies. We are particularly interested in this paper because the approach followed in this thesis is similar to what they proposed.

1.5.4 *Large-scale environmental structures*

The large-scale structure (LSS) of the observable Universe has diverse components, and each of them are not uniformly distributed at all (Fig. 8). Let us focus our interest on dark matter (DM). The nowadays structure of the local Universe is thought to be the outcome of a gravitational instability evolution of small fluctuations in the primordial density field, at the early stages of the Universe. The inflationary model suggests that a very small fluctuation be-

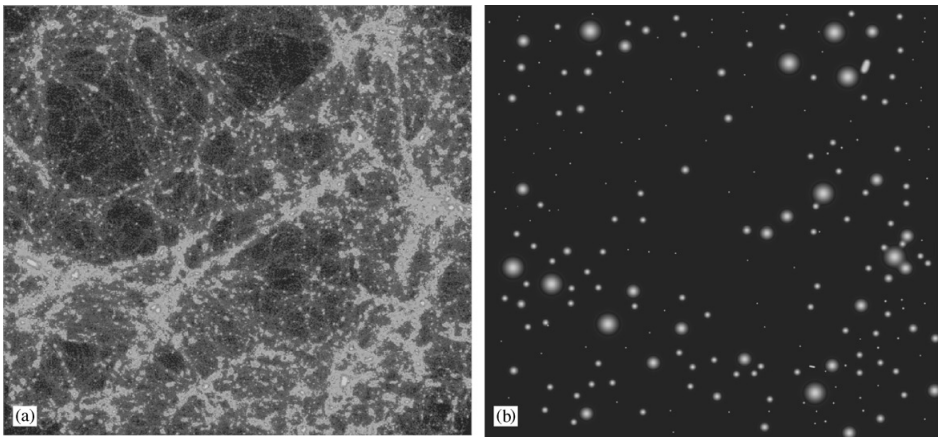

Figure 9: *Left figure (a):* LSS of DM distribution. *Right figure (b):* Map of knots as DM halos to have a discrete number of objects to perform N-body simulations (Cooray and Sheth, 2002).

came a large scale inhomogeneity thanks to inflation, that caused a very rapid expansion of the Universe. After that period, there was a large density field with both underdense and overdense regions that started to interact with each other, mainly because of gravity. The structures that was created with time was defined by Bond, Kofman, and Pogosyan (1996) with the words *cosmic web*. If we assume that the primordial density field had a nearly Gaussian shape, we can describe its evolution with a high order linear and non-linear Perturbation Theory (PT) (Bernardeau et al., 2002). This approach is quite good if we smooth the field up to few megaparsec scale, but when we go to very small scales the PT (at the tree level) is no longer valid, because the field and the clustering of DM become highly non-linear. The highly non-linear evolution of the DM distribution has been widely studied through numerical N-body simulations, and some models that could reproduce it were developed. The most commonly used model, built to reproduce the galaxy halos, is the Navarro-Frenk-White profile (Navarro, Frenk, and White, 1996), which describes a spatial mass distribution of DM in DM halos. They found a relation for DM density as a function of radius

$$\rho(r) = \frac{\rho_{crit} \cdot \delta_c}{\left(\frac{r}{r_s}\right)\left(1+\frac{r}{r_s}\right)^2}, \tag{13}$$

where $r_s = r_{200}/c$ is a characteristic radius, $\rho_{crit} = 3H^2/8\pi G$ is critical density (H is Hubble constant), c and δ_c are dimensionless parameters

$$\delta_c = \frac{200}{3}\frac{c^3}{[\ln(1+c) - c/(1+c)]}, \tag{14}$$

where *200* is the same value chosen to defining r_s.

The N-body simulations performed during the years showed that an initial matter distribution evolves and become a very complex grid of sheets, filaments, voids, and knots, where the latters are clustered DM halos (Fig. 9). A recent cosmic web classification that describes the different components in a

rigorous and theoretical way was introduced by Hahn et al. (2007). Their idea was to consider the motion of a test particle moving in the gravitational potential (ϕ), and, using the equation of motion, retrieve the tidal field tensor, which from the Hessian of the gravitational potential is $T_{ij} \equiv \partial_i \partial_j \phi$. Then they calculated the relative eigenvalues, λ_i with $i = 1, 2, 3$, and they used them to built a classification of the different structures of the cosmic web:

- *Voids*: all eigenvalues are negatives
- *Sheets*: two eigenvalues are negatives and one is positive
- *Filaments*: two eigenvalues are positives and one is negative
- *Knots*: all eigenvalues are positives

This cosmic web classification is commonly known as *T-web*. Due to the definition of these four cosmic environments, the T-web is based on a three-dimensions kinematical footprint. Namely, $\lambda < 0$ means a motion outwards from a certain region (i.e. repulsion), while $\lambda > 0$ means a motion inward to that region (i.e. attraction). Such motions are those of galaxies and larger structure like groups, based on the cosmic web structure they reside in. However, a weakness of this model is precisely the arbitrariness of the threshold ($\lambda_{th} = 0$), that divides positive and negative eigenvalues. Indeed, if we shift the λ_{th} values, a cosmic environments could go from one classification to another. For instance, a filament could become a knot or a sheet, or also a void, depending on the eigenvalue threshold. Therefore, it is not obvious if a filament in the T-web model really is a filament.

A very recent work proposed an alternative theory to fix the problem. Kitaura et al. (2020), instead of taking the eigenvalues of the gravitational tidal field tensor, they are based on the invariants of T_{ij}, I_i with $i = 1, 2, 3, 4, 5$, which are combinations of λ_i. This model is called *I-web*, because it is based on the invariants I, and it is tightly connected with the T-web model. With respect to the T-web, the I-web is a better description for two reasons. The first is that it is independent from the choice of the threshold, so $\lambda_{th} = 0$ or $\neq 0$ shifts only the ensemble of values and does not change the cosmic environment. The second is that the T-web is limited to 4 categories (voids, sheets, filaments and knots), while the I-web is open for a larger number of possibilities.

What we learn from large field survey, and from simulations that built the cosmic web model, is that the luminous matter is not completely untied with the underlying DM distribution. Indeed, since White and Rees (1978), the idea that galaxies form within DM halos has gained a lot of strength. In the White and Rees based models, different galaxy types populate different halos. Precisely, a specific type of galaxy is formed in a specific type of DM halo. If we assume this is true, a detailed description of DM distribution, such as the different cosmic web models, would be extremely useful. Therefore, environment studies are very important to understand how galaxies formed the Universe that we see today.

1.6 OBJECTIVES

The goal of this thesis is to analyse how the environment changes for different types of sources, spread along the quasar MS, by studying close companions around each source. I performed statistical analysis subdividing the sample in different groups, to emphasise as much as possible any possible similarity or difference. These studies have been made at different scales, to investigate the closest local environment and local-large scale environment, and by using different approaches to minimize all the biases which affect the procedures.

An important thing to reiterate is that I am not doing environmental studies, at different scale, for AGN in general, but I am doing these analysis only within the sample selected. All the results obtained are applicable only to the sources I used, and not in general for quasars which populate the main sequence. This is extremely important to emphasize, because the results obtained could change if the selected sample was different. Therefore, in this case a control sample is not necessary at all.

2

SAMPLE AND DATA SELECTION

2.1 ACQUISITION OF DATA

The data used in the present thesis were taken from the Pan-STARRS survey archive, following an already existent list of targets. The sample is composed of 680 sources which are as much as possible spread along the quasar MS. Precisely, almost half of the sources are pop.A (311) and the other half of the sources are pop.B (369). The exact number of sources for each spectral type is: A1: 97, A2: 156, A3: 43, A4: 15, B1: 218, B1+: 115, B1++: 17, B2: 19.

2.1.1 *Sample selection*

The sample was selected by Marziani et al. (2013). The first sample consist of 716 AGN selected from the Sloan Digital Sky Survey[1] (SDSS) Data Release 7 adopting some thresholds in the redshift and the magnitude. They took sources with a redshift inside the range $0.4 \leqslant z \leqslant 0.75$, and brighter than $mag = 18.5$ in g, r or i bands, as was done in Zhou et al. (2006). The redshift range is quite small, thus I can assume that there is no significant cosmological evolution within the sample selected. Moreover, only bright sources were selected since they have good spectra, which are necessary to perform deep spectroscopic analysis. After these two first selections, 36 sources were discarded, since they showed very noisy spectra and an unusual red colour. They used three prominent narrow lines ([O II], Hβ and [O III] λ5007), to set the rest frame. In addition to the redshift values provided by the SDSS, they computed it again by taking an average of the three lines in each source spectrum. They used the command SPLOT of IRAF to estimate the FWHM(Hβ) to separate sources into spectral bins, as suggested in Sulentic et al. (2002). Using the command NGAUSSFIT, $R_{Fe\ II}$ was estimated and the final precise assignments of the corresponding bin has been made visually.

2.1.2 *Pan-STARRS survey*

Pan-STARRS is the acronym of Panoramic Survey Telescope and Rapid Response System. Pan-STARRS is a system of wide-field astronomical imaging developed and operated by the Institute for Astronomy at the University of Hawaii. This project used several telescopes, but the first which has been built to this purpose is the Pan-STARRS1 (PS1) Telescope. It is an altazimuthal mounting telescope with a 1.8m diameter mirror. The details are described in Table 2. The construction design of the telescope with corresponding optical

1 www.sdss.org

Table 2: Pan-STARRS1 main characteristics (https://outerspace.stsci.edu/display/PANSTARRS/).

characteristic	**description**
telescope focal length	8000 mm
plate scale	25.75 arcsec/mm
field of view diameter	3.0 degrees
field of view area	7.068 square degrees
primary mirror diameter	1800 mm
primary mirror coating	protected aluminum
secondary mirror diameter	947 mm
secondary mirror coating	protected silver
focal ratio	4.44
effective aperture	17 284 cm^2
detector pixel size	10 µm = 0.258 arcsec
camera fill factor	76%

path is shown in Fig. 10. It is a Ritchey-Chretien configuration telescope designed by Morgan and Kaiser (2008), characterized by a wide field of view and the presence of three correction lenses just before the Charge-Coupled Device (CCD). In the middle of the correction lenses a set of filters is present.

The CCD mounted in the focal plane of the telescope is called Gigapixel Camera 1 (GPC1). It consists of 60 CCID58 back-illuminated Orthogonal Transfer Array (OTA) devices, which is a concept developed by Tonry, Burke, and Schechter (1997). Each of these devices consists of an 8×8 array of individual addressable CCDs called "cells". Each OTA consists of 64 cells, with 590×598 pixels, which on the whole create an array of 4846×4868 pixels.

Large field surveys made with PS1 are carried out through a set of five broadband filters designated as *grizy*, word that arises from the combination of the letters referred to the single filters. The mean wavelengths of each filters are: $g = 4866$Å, $r = 6215$Å, $i = 7545$Å, $z = 8679$Å and $y = 9633$Å. In addition to these five filters, another filter is used. This one is called *w* (wide) filter and it is mainly use for near-earth object and not for large-scale surveys. The bandpass of the filters along the wavelength axis is shown in Fig. 11.

Using the PS1 facility, several surveys have been made. The main one is the 3π Steradian Survey, which covers 30 000 deg^2 (3 steradians) of northern sky with minimum Declination of $-30°$. This survey was performed in the five filters aforementioned, with approximately ten exposures for each filter, reaching a combined depth of approximately 21-23 mag. Data were taken over the period between 2009 and 2014. During this survey, two schedules and organizations were adopted: the initial pattern laid out is the Design Reference Mission (DRM), which was replaced, in 2012, by the Modified Design Reference Mission (MDRM). In DRM each exposure was separated by a Tran-

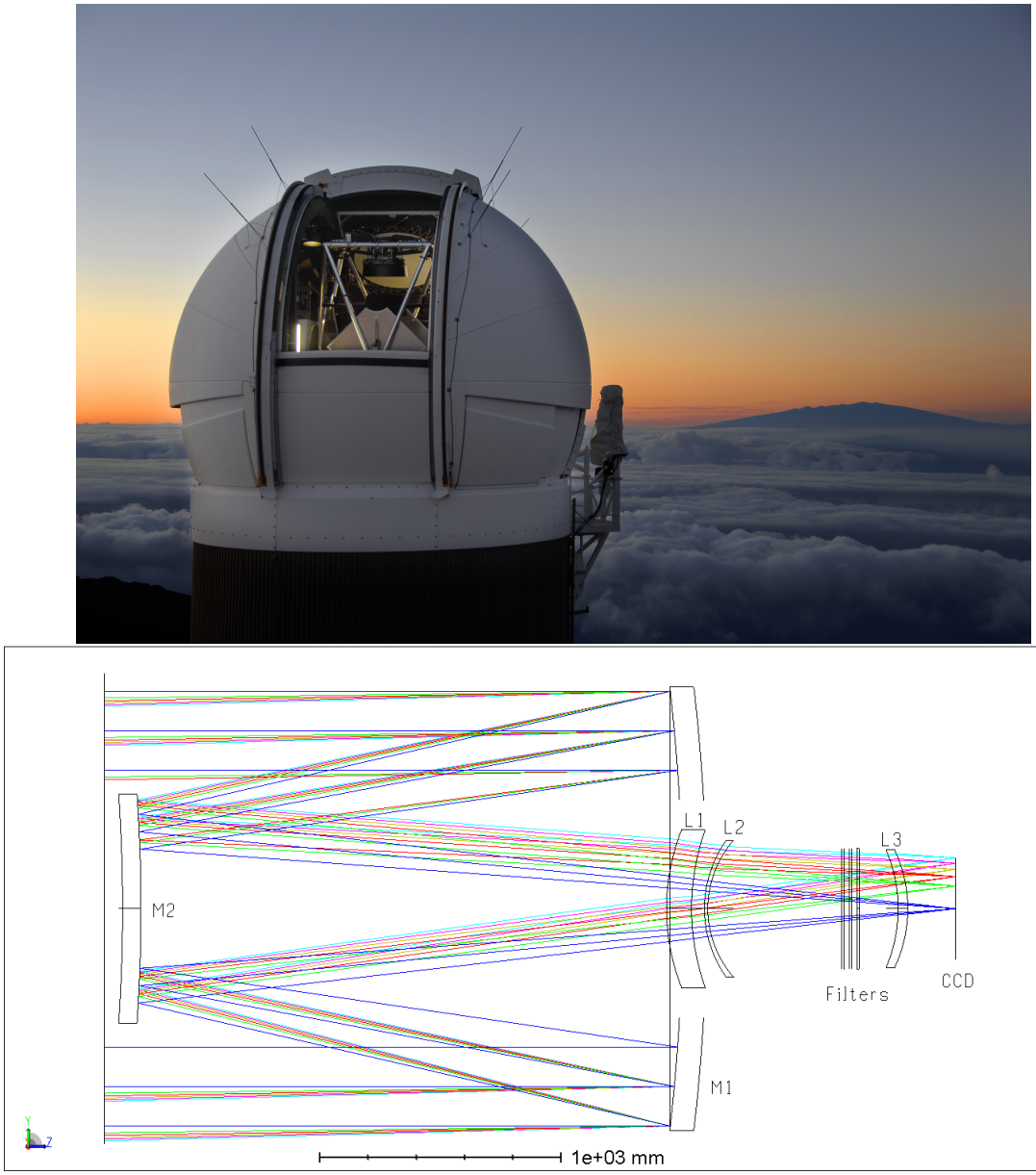

Figure 10: *Top figure*: Photography of the telescope site (http://www.ifa.hawaii.edu/info/press-releases/PS1/PS1.jpg). *Bottom figure*: Scheme of optical path and structure of the telescope (Chambers et al., 2016).

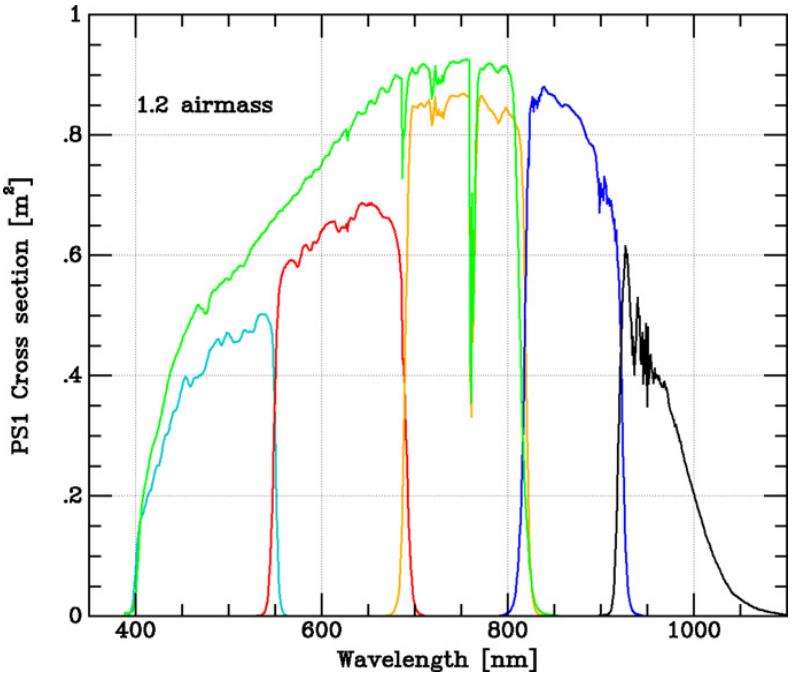

Figure 11: The PS1 capture cross-section in $\mathrm{m}^2 e^{-1} \mathrm{photon}^{-1}$ to produce a detected electron for an incident photon for the six Pan-STARRS1 bandpasses, considering a standard airmass of 1.2. The five consecutive colour curves, from cyan to black, are referred to *grizy* filters. Green curve, instead, represents the w-filter (Tonry et al., 2012).

sient Time Interval (TTI), with the duration from 12 to 24 minutes, in which moving objects within the Solar System were searched.

Since the beginning of the PS1 project, two Data Releases have been made: DR1 and DR2. DR1 is composed only of data taken before 2012, basically with DRM schedule. DR2, instead, contains all the data acquired by the PS1 project up to 2014. This second data released is that used in this analysis.

2.2 GALAXIES-STARS SEPARATION

The first necessary step is to retrieve the data from the Pan-STARRS archive. All PS1 data are archived at the Space Telescope Science Institute (STScI) in Baltimore, Maryland, and can be accessed through the portal Mikulski Archive for Space Telescopes (MAST). From it I downloaded data products related to the objects inside areas, in the celestial sphere, of 500 kpc and 30 arcmin radii, around each AGN selected. As I said before, the redshift are different inside the sample, this means that the scale $\mathrm{kpc}/\mathrm{arcsec}$ is different for each source and the radius must be calculated time by time.

Since we are observing a portion of sky, both galaxies and stars are included in the downloaded data. However, I want to find only galaxies as possible companions of the AGN in the sample. Therefore, I have to separate galaxies and stars, and then discard the latters. For this purpose a Pan-STARRS webpage[2]

2 https://outerspace.stsci.edu/display/PANSTARRS/How+to+separate+stars+and+galaxies

is present, which summarises all the possible approaches, developed over the years, to separate galaxies and stars. Two methods have been tried in this thesis: the PSF-Kron magnitude (Farrow et al., 2014) and the psfLikelihood.

The PSF-Kron magnitude is a separation method developed by Farrow et al. (2014). Via simulations of very large samples of data, they found that the difference between the PSF magnitude and the Kron magnitude ($\Delta_{PSF-Kron}$), for galaxies and stars, gives different results. Precisely, on average, $\Delta_{PSF-Kron}$ is bigger than 0.05 for galaxies, and lower than the same value for stars. The PSF magnitude for a galaxy arises from the Sérsic function, also called $R^{1/n}$ model, which well fits its light profile (Sérsic, 1963; see Graham and Driver (2005) for a review). Following such model the intensity profile is

$$I(R) = I_e \exp\left\{-b_n\left[\left(\frac{R}{R_e}\right)^{1/n} - 1\right]\right\}, \tag{15}$$

where I_e is the intensity at the effective radius R_e, which in turn is the radius that encloses half of the total light. Finally b_n is a scalar value that depends on the index n. Values of $n = 1$ and $b_n = 1.678$ give an exponential profile, common in the disk of spiral galaxies, while $n = 4$ and $b_n = 7.669$ represent the de Vaucouleurs profile, typical of elliptical galaxies (de Vaucouleurs, 1948). For stars in the PS1, they used a fitting model

$$I = \frac{I_0}{1 + kz + z^{3.33/2}} \quad \text{where} \quad z = \frac{x^2}{2\sigma_x^2} + \frac{y^2}{2\sigma_y^2} + xy\sigma_{xy}, \tag{16}$$

where I_0 is the central intensity, x and y are the distances from the centre along the x- and y-axes, k is a free parameter, and σ_x, σ_y, σ_{xy} are x-axis width, y-axis width, and a cross-term, respectively. After several tests, they have shown that this separation method works with a confidence level between 91-98%. Kron magnitude is defined using the luminosity-weighted radius (R_1) which defines the 'first moment' of an image, and this latter is the result of a combination of pixels' intensity value

$$R_1(R) = \frac{2\pi \int_0^R I(x)x^2 dx}{2\pi \int_0^R I(x)x dx}, \tag{17}$$

where R is the radius which contain 1% of the sky flux (Kron, 1980). Following that $\sim$ 90% of the source's flux is inside R_1. In the PS1 survey the Kron magnitude is defined as the light intensity in $2.5 \times R_1$. The advantage of PSF-Kron method is that all the sources in the MAST have PSF and Kron magnitude available, so a result, more or less reliable, is guaranteed.

In the psfLikelihood method, the separation is made considering that for galaxies psfLikelihood is ~ 0 and for stars it is close to 1, in absolute value. I used a threshold of |psfLikelihood|<0.5 to distinguish a galaxy from a star.

The method that gives me less sources is the PSF-Kron magnitude. I used this because the possibility of false positives is reduced. In Fig. 12 is shown the quantity of galaxies+stars (red line) and of the only galaxies after the application of the PSF-Kron magnitude separation method (blue line).

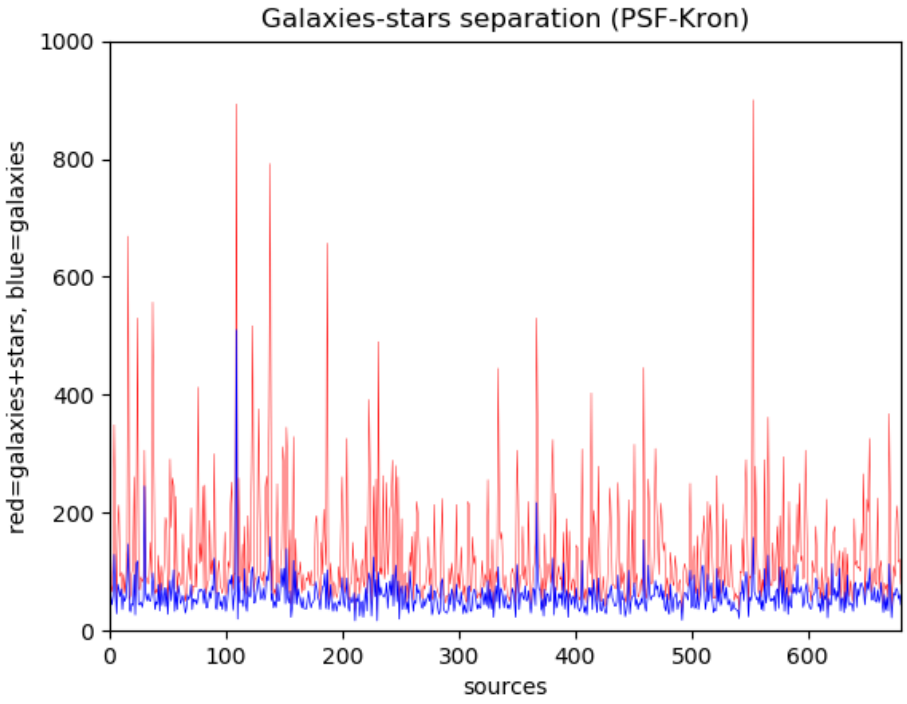

Figure 12: Before and after the PSF-Kron magnitude separation method to separate galaxies and stars. The red line identifies the number of objects downloaded from the Pan-STARRS catalogue (y-axis) around each source (marked as a number on the x-axis). The blue line identifies the number of galaxies left (y-axis) after the separation, in the same conditions.

2.3 SELECTION METHODS

At this stage, all the remaining sources are galaxies. Nevertheless, no object has a redshift information, so the principal effort is to understand which galaxy is really a close physical companion of the central AGN, and not only angularly close but far in front or behind in radial direction. I used three approaches: magnitude selection, photometric redshift selection, and density approach. Without any experimental confirmation I cannot say which method is the best and gives the most reliable results. I decided to try all of them for this very reason. Each of them have positive and negative aspects, and comparing their results at the end is very worthwhile.

2.3.1 *Magnitude selection*

Originally the way to understand whether two objects, of the same kind, are close to each other or not was developed by Rafanelli and Marziani (1992). In that paper they analysed the environment around a sample of Sy1 and Sy2 galaxies using the galaxy companions. They found an excess of companions in the Sy1 sample respect to the Sy2 sample. Different results have been found in Laurikainen et al. (1994), which found an excess of companions for their Sy2 sample. In addition to these two papers, several others similar papers have been made, like Rafanelli, Violato, and Baruffolo (1995) who have found no significant difference between Sy1 and Sy2 galaxies. Finally, Dultzin-Hacyan et al. (1999) have done a great work to try to find the correct answer, confirming Laurikainen et al. (1994) results.

In the previous cases, the magnitude method has been adopted to search for close companions around the sources of two separate classes, Sy1 and Sy2 galaxies, which is not too different from what I want to do. Rafanelli, Violato, and Baruffolo (1995) proved that almost 90% of objects, which are close enough to a selected source that can be defined physical companions, have magnitudes within 3 mag from the target. It is important to notice that in Rafanelli, Violato, and Baruffolo (1995) this approach is almost completely justified. Since they used Palomar Observatory Sky Survey (POSS) the faintest magnitude detected is ~ 15.5. Therefore, the only detectable objects around a source are very bright, and since the Seyfert galaxies that constitute their sample are bright sources, they found basically only similar objects taking a range of $3\,\mathrm{mag}$. Using more recent surveys, the detection limit in magnitude increases a lot (in the PS1 survey it is around $\sim 22-23\,\mathrm{mag}$). Therefore, more sources and of different types are included. In addition, more distant objects are visible since the increasing of the limit in magnitude allows observations at higher redshift.

In the present analysis I applied the magnitude selection both considering each filter separately and all filters simultaneously. In the first selection method, an object is classified as a companion if its magnitude in the filter band minus the magnitude of the principal source in the same band is less than 3, in absolute value, and this procedure has been made separately for each

filter. In the second case, I did the procedure only one time and I consider a galaxy companion if in at least one filter band the difference in magnitude is less than 3, also in this case in absolute value.

2.3.2 *Photometric redshift selection*

PS1 is a 5-band photometric survey, and not a spectroscopic one, therefore the spectroscopic redshift is information not available in the data archive. It is basically impossible to take spectra for all the sources, because too much time would be needed given the large amount of targets involved. However, some information can be retrieved using the available magnitudes. In fact, the magnitude in the five bands can give us a crude spectrum, composed of five points, through which several calculation can be made. Recently Tarrío and Zarattini (2020) developed an highly sophisticated algorithm, built ad hoc for the PS1 DR2 data, which is able to calculate the photometric redshift of each object. It uses a training set of 2 313 724 galaxies for which the spectroscopic redshift is available from the SDSS, and magnitudes and colours are obtained from the PS1 DR2 survey. The algorithm is based on the local linear model (Beck et al., 2016) which establishes that the redshift of a galaxy can be obtained with a linear regression in a 5D space. This latter is a linear combination of the so called D galaxy properties (magnitudes and colours). The magnitude values used are the Kron ones in *g*, *r*, *i*, *z*, and *y* bands. This huge training set allows to retrieve precise results for a big area of the sky, covered by the PS1 survey. For this approach, they estimate an average bias of $\overline{\Delta z_{norm}} = -1.92 \times 10^{-4}$, and a standard deviation of $\sigma(\Delta z_{norm}) = 0.0299$.

In the present case I downloaded Kron magnitudes from the MAST table called StackObjectThin, and then processed and prepared as input for the algorithm.

Tarrío and Zarattini (2020) software gives as outputs photometric redshift values, with relative errors. Besides, spectroscopic redshifts for the 680 principal sources are available. Using them, I selected as companions those objects for which the difference between their photometric redshift and the spectroscopic redshift of the central AGN, times the speed of light is less than 1000 km s^{-1}, namely $|c \times \Delta z_{source-comp}| \leqslant 1000$ km s^{-1}, as suggested in Rafanelli, Violato, and Baruffolo (1995).

2.3.3 *Density approach*

The last approach that I used is not properly a selection method, but a comparison method. At very large scale the galaxy number density is almost isotropic and homogeneous, but in the local environment it is completely different from one source to another. Assuming this as an environmental comparison between the local areas considered and the very-large scale, it can give us a lot of information. The idea is to do a correction to the number of galaxies selected around the AGN, using the number density retrieved from very-large scale data. In this way I can investigate the differences between the very-large

scales and the searched areas used in the analysis, and I can finally compare the results between all the AGN in the sample. Using this approach I did not obtain a precise value for the number of companions, but rather an indication of how dense the local environment is.

Operationally, I downloaded from the MAST the data for the largest possible area considering a fixed aperture in the sky, and not a distance based on the redshift as did before. The aperture chosen is $0.5\,\mathrm{deg} = 30\,\mathrm{arcmin}$ in celestial sphere, centered in each source of the sample. Every file contains even tens of thousands of objects, and also in this case I did the galaxies-stars separation using the PSF-Kron method. Subsequently, the number of galaxies inside the region of interest (searched area) was subtracted, to not influence the final density, and it was divided by the area with a radius of 30 arcmin minus the searched area. Finally, I calculated the number density value (ρ)

$$\rho = \frac{[n^o objects(Area = 0.7854\ deg^2)] - [n^o objects(searched\ area)]}{[Area(r = 30\ arcmin) = 0.7854\,deg^2] - [searched\ area]}. \tag{18}$$

This number is a number density of all galaxies within that region. I subtracted this number density, rescaled for the searched area, from the real number of sources in the searched area. If the resulting value is positive it means that the local region close to the AGN is an overdense region. On the contrary, if the value is negative the source lives in an underdense region.

Additionally, I estimated the fraction of sources in the principal sample with at least one physical companion, following the procedure suggested in Krongold, Dultzin-Hacyan, and Marziani (2001). The probability to find one or more optical companions within a given search area follows the relation

$$P = 1 - e^{-\rho a}, \tag{19}$$

where ρ is the number density as calculated in Eq. 18 and a the area subtended by the search radius (see Dahari (1984) for a complete description). The fraction of principal sources with at least one physical companions are then calculated taking the fraction of sources with observed companions (f_{obs}), diminished by the fraction of sources with optical companions (foreground/background objects, f_{opt}), which is calculated as the mean value of the probability (<P>) calculated using Eq. 19

$$f_{phys} = f_{obs} - f_{opt}. \tag{20}$$

In the present analysis I used areas with radii of 100 and 50 kpc, since for larger areas the probability to find at least one companion is almost always equal to one.

It is of crucial importance to reiterate that I am not doing an absolute environmental study around AGN, but I am doing a comparison between the environments of subsamples of sources in the MS. Therefore, a control sample is not necessary.

2.4 BIASES

As I said before, each aforementioned selection method has pros and cons. In all of them there are several biases which are not negligible. We will see one by one the three main methods, highlighting the biases in them.

In the PS1 data, several objects do not have all photometric band magnitudes available. In the magnitude approach this lack influences the selection both considering all filters simultaneously and each filter separately, reducing the possibility to find companions. I noticed that the filter with the least data available is the g-filter, and that with the most data is the z-filter, although no criterion which can explain this difference is visible. Another issue is that I knew neither the morphology nor the redshift of the objects. In this way it is almost impossible to estimate the spectral shape, and how much the spectrum is shifted, by only using the five magnitude bands. Therefore, I cannot be sure that all the galaxies selected using $\Delta m \leqslant 3$ are really close companions, because objects not physically close to the central source may have been included and some other which are instead at small distance may have been discarded. Finally, the choice of $\Delta m = 3$ in apparent magnitude are taken from Rafanelli and Marziani (1992), and it has not been tested specifically for the present analysis. Taking a range in magnitude like this means either risking to select only galaxies similar to the central source, if the possible companions have similar redshifts, or to select galaxies with different redshift but which have similar surface brightness. Unfortunately, it is a risk that cannot be avoided, because it is impossible to know in advance which types of galaxies reside in the different sky position.

The lack of magnitudes is a problem for the photometric redshift selection method too. Indeed, for an object the Tarrío and Zarattini (2020) algorithm works only if all the five band magnitudes are available. In Fig. 13 I show the available percentage of the photometric redshifts of the possible companions around each galaxy. On average, in the whole sample the value of such percentage is $\sim 70\%$. This bias, obviously, limits the number of companions which can be identified. To verify how reliable the photometric redshift values are we have to trust the tests made by the authors of the algorithm, since most of the possible companions have no spectroscopic redshift data which could be used to compare the results. Moreover, the algorithm calculated some photometric redshift values from objects which do not have all the magnitude bands available. This means that the algorithm does not work properly in all cases.

The density approach does not tell us the exact number of companions around a source, and also in this case there are biases. For example, galaxies-stars separation affects in a strong way the resulting density values, due to the large amount of data included in very large scale files. In addition, when I subtract the number of objects with the rescaled number density, a negative number of companions is not a realistic value, but it means that the number of companions predicted using the large-scale number density is larger than the number of objects which really reside around the central source. The fraction of sources with physical companions expresses the probability that a target

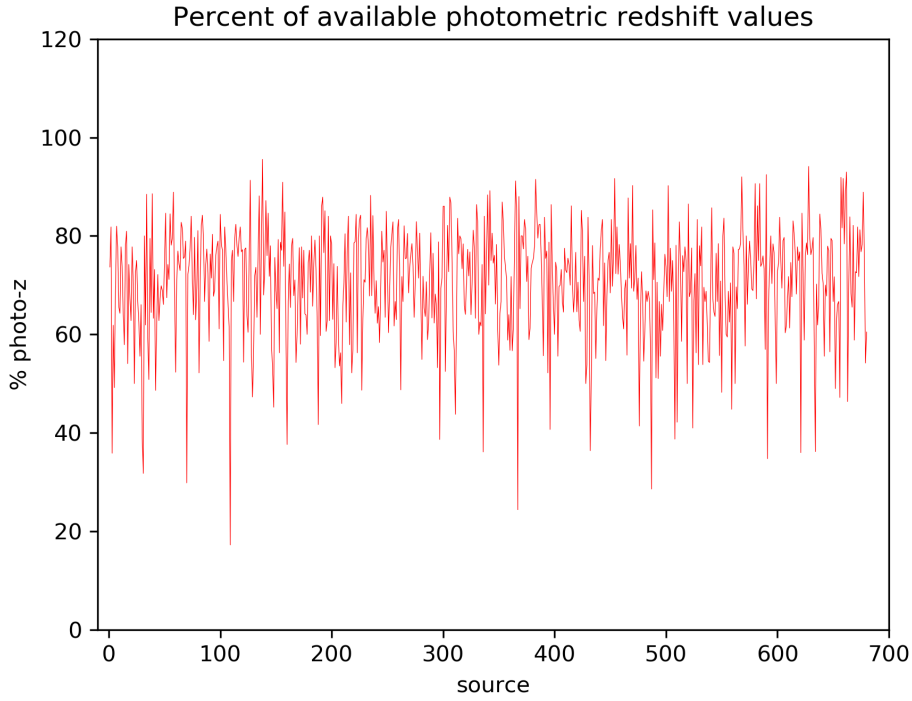

Figure 13: Red line identifies the percentage of the available photometric redshifts for each galaxy in the search field.

have one or more companions in the searched area considered. Therefore, also this last analysis performed does not estimate the real number of companions.

2.5 STATISTICAL TESTS

To analyse and compare the different subsamples, I performed several statistical tests. The FWHM(Hβ) of the sources in the sample and the number of companions for each source are the first characteristics that I tested. Any possible correlation between these two variables has been searched using three statistical tests: Pearson, Spearman, and Kendall test. These tests work in different ways, but all of them give two resulting values: a correlation value and a p-value. The first varies from -1 to 1, and it expresses the strength of the correlation. If it is equal to one, or minus one, there is a perfect negative or positive correlation. The closer it gets to one in absolute value, the stronger the correlation is. On the contrary, if it is close to 0 there is no correlation between the two variables, or the correlation is very weak. The p-value identifies the robustness of the correlation, and it varies from 0 to 1. If it is close to 1, it means that the probability that the correlation is random is high. On the other hand, if it is close to 0, it means that the two variables are correlated, and so that the probability that the correlation is random is low. I chose to fix the rejection of the null hypothesis at a 95% confidence level, corresponding to a p-value threshold of 0.05. Pearson and Spearman tests are similar, the

main difference is that the Pearson coefficient works with a linear relationship between the two variables whereas the Spearman coefficient works with any monotonic relationship. Moreover, Pearson test is a parametric test and it works only if the two input variables express a real physical quantity. Spearman and Kendall tests, instead, are non-parametric tests and work even if one of the two input variables is a qualitative characteristic. Nevertheless, Kendall test uses different formulas compared to the other two tests. Subsequently, to study different spectral populations, I used the Kolmogorov-Smirnov (K-S) and the Anderson-Darling (A-D) tests. In this case, I used the same variables as inputs but taken from two different subsamples, like Population A and B sources, or A4 an B1++ sources. Both the tests compare how the two companions' distributions of the subsamples differ from each other. The null hypothesis means that the two distributions are equal, or that have been drawn from the same population. Both tests give a p-value as the most relevant resulting value. The p-value varies in the range from 0 to 1 for K-S test, and from 0 to 0.25 for A-D tests. I decided to fix the rejection of the null hypothesis at a 95% confidence level, corresponding to a p-value threshold of 0.05 and 0.0125, for K-S and A-D respectively.

To check if the large-scale number densities, for population A and B, are similar I used the Mann-Whitney U-test. It is a non-parametric test of the null hypothesis that tests if the distribution underlying pop.A sample is the same as the distribution underlying pop.B sample. I decided to fix the rejection of the null hypothesis at a 95% confidence level, corresponding to a p-value threshold of 0.05.

3

DATA ANALYSIS

To do a study as complete as possible, I decided to apply the selection methods at different scales. Both the magnitude selection and the density approach have been used for areas with radii of 500, 250 and 100 kpc. The photometric redshift selection has been used only for area with 500 kpc radius. Instead, the fraction of sources with at least one physical companions has been calculated, as said before, for areas with radii of 100 and 50 kpc. Areas with radii of 500, 250, 100 and 50 kpc, hereafter will be called A500, A250, A100, and A50, respectively.

In all the three selection methods I mainly identified four subsamples to use in the analysis: population A and B, and A4 and B1++ sources. Population A and B are the two main classes in the MS, so they are the big populations which must be analysed as first step. A4 and B1++ sources are the subpopulations which extreme the principal population A and B. A4 are fast-accreting objects with a very high $R_{Fe\ II}$, and they have usually a weak radio emission (Ganci et al., 2019; Marziani and Sulentic, 2014). B1++, on the other hand, are prevalently low-accreting objects with low $R_{Fe\ II}$, and they are almost all sources with a strong radio emission (Ganci et al., 2019; Marziani et al., 2022). In addition, it has been found that A4 host lower BH mass than B1++ sources (Ganci et al., 2019).

In the following I will describe the plots and statistical tests performed for the selection methods at different areas. It is important to note that, in addition to the statistical tests, visual analysis on the plots were made.

3.1 MAGNITUDE SELECTION

The magnitude selection is based on the *grizy* filters. As I said in the previous chapter, I tried to apply the magnitude selection both considering each filter separately and all filters simultaneously. In both cases I plotted the number of companions obtained for each source. These plots were made for each filter separately considering A500, and considering a selection with all filters for A500, A250 and A100. I chose to use all filters selection for all the statistical tests and plots that I did in the three areas. I plotted again the number of companions in y-axis, but this time taking the FWHM(Hβ) of principal sources as the x-axis, for A500, A250 and A100. I made the FWHM(Hβ) vs median of the number of companions, dividing the FWHM(Hβ) in 1000, 2000 and 4000 km s^{-1} wide bins, for A500, A250 and A100. Two of the last plots, the FWHM(Hβ) vs number of companions, and the FWHM(Hβ) vs median of the number of companions with bins of 1000 km s^{-1}, were superimposed in one scatter plot, always for A500, A250 and A100.

Table 3: FWHM(Hβ) sources' sample - n°companions, magnitude selection statistical tests.

statistical test	**correlation value**	**p-value**
Pearson (A500)	0.32646	2.37612×10^{-18}
Spearman (A500)	0.27421	3.40760×10^{-13}
Kendall (A500)	0.18676	1.31958×10^{-12}
Pearson (A250)	0.22118	5.56420×10^{-9}
Spearman (A250)	0.17794	3.02785×10^{-6}
Kendall (A250)	0.12408	4.91574×10^{-6}
Pearson (A100)	0.16716	1.17646×10^{-5}
Spearman (A100)	0.14346	0.00017
Kendall (A100)	0.11027	0.00019

The four main subsamples which I used in this studies are population A, population B, A4 and B1++ sources. I made an histogram for the mean value of companions in population A and B. Companions' distributions were used as inputs for the K-S and A-D tests. I plotted the companions' distribution as the number of companions in x-axis, with bins equal to 5 and 2 companions, vs the number of sources which have such number of companions in y-axis. This was done also in this case for A500, A250, and A100. Precisely, I compared population A and B in one case and A4 and B1++ sources in the other. In both cases, bins of 5 and 2 companions were used, for a total of four tests for each searched area. As inputs for Pearson, Spearman, and Kendall correlation analysis I used the FWHM(Hβ) and number of companions. In the following tables (Table 3, 4) the resulting values obtained are shown.

3.2 PHOTOMETRIC REDSHIFT SELECTION

The plots and statistical tests I did for photometric redshift selection are similar to those I performed in the previous method. One of the main differences is that I chose to apply this selection method only for A500, due to the few candidate companions found even in this largest area. The first plot that I did shows the sources vs number of companions selected. A similar plot has been made taking the FWHM(Hβ) of principal sources, in x-axis, instead of the sources' order of the original sample. Taking 1000, 2000, and 4000 km s^{-1} wide bins for the FWHM(Hβ), I plotted three histograms for FWHM(Hβ) binned vs median number of companions. I superimposed the first plot with the latter, with the 1000 km s^{-1} wide bins for the FWHM(Hβ), in one scatter plot.

I performed Pearson, Spearman, and Kendall statistical tests always using the FWHM(Hβ) of principal sources and number of companions. I made two subsamples for population A and population B, and I plotted their mean value of companions in a histogram. For K-S and A-D tests I constructed the com-

Table 4: Magnitude selection statistical tests. Columns: (1,2) population A-population B sources, (3,4) A4-B1++ sources.

statistical test	**p-value**	**statistical test**	**p-value**
K-S, bin=5 (A500)	0.99692	K-S, bin=5 (A500)	0.63549
A-D, bin=5 (A500)	0.25	A-D, bin=5 (A500)	0.10500
K-S, bin=2 (A500)	0.80119	K-S, bin=2 (A500)	0.69018
A-D, bin=2 (A500)	0.03590	A-D, bin=2 (A500)	0.05138
K-S, bin=5 (A250)	0.99692	K-S, bin=5 (A250)	1.0
A-D, bin=5 (A250)	0.20882	A-D, bin=5 (A250)	0.25
K-S, bin=2 (A250)	0.99995	K-S, bin=2 (A250)	1.0
A-D, bin=2 (A250)	0.25	A-D, bin=2 (A250)	0.25
K-S, bin=5 (A100)	1.0	K-S, bin=5 (A100)	1.0
A-D, bin=5 (A100)	0.25	A-D, bin=5 (A100)	0.25
K-S, bin=2 (A100)	1.0	K-S, bin=2 (A100)	1.0
A-D, bin=2 (A100)	0.25	A-D, bin=2 (A100)	0.25

Table 5: FWHM(Hβ) sources' sample - n°companions, photometric redshift selection statistical tests, in A500.

statistical test	**correlation value**	**p-value**
Pearson (A500)	0.06107	0.11162
Spearman (A500)	-0.01277	0.73968
Kendall (A500)	-0.01088	0.71718

panions' distribution as number of companions in x-axis, with bins equal to 5 and 2 companions, vs the number of sources which have such number of companions, in y-axis. These companions' distributions were plotted in histograms for population A, population B, A4 and B1++ sources. In the following tables (Table 5, 6) are shown the resulting values obtained.

3.3 DENSITY APPROACH

The density approach is based on large-scale data. The first plot I created, similarly to what was done in the previous two methods, is the FWHM(Hβ) of principal sources vs number of companions, that was obtained by subtracting the number of galaxies in the search area with the number density rescaled for the same area, for A500, A250, and A100. Also in this case, I made histograms with 1000, 2000, and 4000 km s^{-1} wide bins for the FWHM(Hβ) in x-axis, and the median number of companions in y-axis, for the three search areas. I superimposed the first with the second plot, with bins of 1000 km s^{-1} wide,

Table 6: Photometric redshift selection statistical tests, in A500. Columns: (1,2) population A-population B sources, (3,4) A4-B1++ sources.

statistical test	**p-value**	**statistical test**	**p-value**
K-S, bin=5	1.0	K-S, bin=5	1.0
A-D, bin=5	0.25	A-D, bin=5	0.25
K-S, bin=2	1.0	K-S, bin=2	1.0
A-D, bin=2	0.25	A-D, bin=2	0.25

for A500, A250, and A100. Beside the number of companions, I calculated the fractional overdensity, which is the number of companions in the search area divided by the number density rescaled for the same area. A fractional overdensity larger than one means a close environment denser with respect to the large-scale environment. Conversely, a value lower than one means a lower density in the local environment than in the large-scale environment. I made a scatter plot for the FWHM(Hβ) vs fractional overdensity, highlighting the value equal to one for a better visual inspection.

I made two different plots for population A and B. In both plots the x-axis is the FWHM(Hβ), while in y-axis in one case there is the mean number of companions, in the other case there is the fractional overdensity, that here is defined as the mean value of companions divided by the mean number density rescaled in the area considered. In this case, the associated error to the fractional overdensity is the standard error of the mean ($\sigma_{\bar{x}}$), which is the ratio between the standard deviation (σ) and the square root of the number of values (n) used to calculate the mean value

$$\sigma_{\bar{x}} = \frac{\sigma}{\sqrt{n}}. \tag{21}$$

As in the previous selection methods, I did plots with in x-axis the number of companions, with bins of 5 and 2 companions, and in y-axis the number of sources which have such a number of companions, for population A, population B, A4 sources, and B1++ sources, obtaining the companions' distributions. Using these as inputs I performed the K-S and A-D tests. As before, Pearson, Spearman, and Kendall are the correlation analysis performed using as inputs the FWHM(Hβ) and the number of companions.

To find any possible anomalies in large-scale data, I performed a Mann-Whitney U-test on the large-scale companion number densities of population A and B. Additionally, I plotted an histogram comparing the mean value of companions in the large scale, for population A and B, to visually check for any possible difference. Also for these last values, the standard error of the mean was calculated. In the following tables (Table 7, 8, 9) the resulting values obtained are shown.

Table 7: FWHM(Hβ) sources' sample - n°companions, density approach statistical tests.

statistical test	**correlation value**	**p-value**
Pearson (A500)	0.04054	0.29111
Spearman (A500)	0.06699	0.08087
Kendall (A500)	0.04464	0.08159
Pearson (A250)	-0.00896	0.81563
Spearman (A250)	0.02141	0.57726
Kendall (A250)	0.01413	0.58156
Pearson (A100)	0.00243	0.94963
Spearman (A100)	0.04025	0.29462
Kendall (A100)	0.02728	0.28725

Table 8: Density approach statistical tests. Columns: (1,2) population A-population B sources, (3,4) A4-B1++ sources.

statistical test	**p-value**	**statistical test**	**p-value**
K-S, bin=5 (A500)	0.99999	K-S, bin=5 (A500)	0.92052
A-D, bin=5 (A500)	0.25	A-D, bin=5 (A500)	0.25
K-S, bin=2 (A500)	0.99995	K-S, bin=2 (A500)	0.69019
A-D, bin=2 (A500)	0.25	A-D, bin=2 (A500)	0.12343
K-S, bin=5 (A250)	1.0	K-S, bin=5 (A250)	1.0
A-D, bin=5 (A250)	0.25	A-D, bin=5 (A250)	0.25
K-S, bin=2 (A250)	1.0	K-S, bin=2 (A250)	1.0
A-D, bin=2 (A250)	0.25	A-D, bin=2 (A250)	0.25
K-S, bin=5 (A100)	1.0	K-S, bin=5 (A100)	1.0
A-D, bin=5 (A100)	0.25	A-D, bin=5 (A100)	0.25
K-S, bin=2 (A100)	0.99950	K-S, bin=2 (A100)	1.0
A-D, bin=2 (A100)	0.25	A-D, bin=2 (A100)	0.25

Table 9: Mann-Whitney U-test for population A - population B large-scale sample sources.

parameter tested	**p-value**
number of galaxies	0.20707

Table 10: A-D tests for population A-population B original sample sources.

parameter tested	**p-value**
spectroscopic z	0.05753
i-Kron magnitude	0.001

Table 11: Mean magnitude values of original sample.

mean value	**pop.A**	**pop.B**
i-Kron magnitude	17.18317±0.02729	17.60326±0.03424

3.3.1 *Physical companions*

To compare the fraction of population A and B sources with physical companions, I calculated this value and I plotted it in a histogram, for A100 and A50. The associated error was calculated using a 95% confidence interval assuming a Poissonian distribution as normal approximation (Patil and Kulkarni, 2012). In this case, the error is calculated as

$$err = 1.96\sqrt{\frac{\lambda}{n}}, \tag{22}$$

where 1.96 is a numerical factor related to the 95% confidence level, λ is referred to the Poissonian mean, and n is the number of sources used to calculate the mean value.

3.4 SAMPLE ANALYSIS

To identify anomalies in the original sample, I performed some control tests. I did an A-D test for spectroscopic redshift and the i-Kron magnitude using population A and B as subsamples. I also visually compared the mean i-Kron magnitude values of the two subsamples. The error associated to the mean i-Kron magnitude values is the standard error of the mean. In the following tables (Table 10, 11) the resulting values obtained are shown.

4

RESULTS

In the present chapter I will discuss the results obtained, both plots and statistical results. Since the high quantity of plots that have been made, in the following paragraph I will show only the most relevant ones. All the other plots are presented in the Appendix. The order of the original sample was not chose considering the FWHM(Hβ), but the sources was grouped only considering the spectral type. Therefore, the spectral type order of the first sample is: A1, A2, A3, A4, B1, B1+, B1++, and B2. In the plots this order will be call *source order*. In the other hand, after having reordered according to the FWHM(Hβ) of each source in the sample, this order will be call *FWHM order* in the plots.

4.1 MAGNITUDE SELECTION

For magnitude selection method I decided to use the selection with all filters simultaneously, instead of the selection using only one filter, because the choice of the most suitable filter would have required a deep analysis of the biases which would have been very difficult using only the available data. In Fig. 14 the number of selected companions is shown.

In Fig. 15 is shown the number of companions, which reside inside A500, with the FWHM(Hβ) of the principal sources in the x-axis. I noticed that, in the original sample there is a high concentration of AGN with a small FWHM(Hβ), compared to, for example, the sources that have FWHM(Hβ)> 10000 km s^{-1}. Reducing the search area, on average the number of companions is reduced, which is pretty obvious.

I binned the FWHM(Hβ) using different widths, 1000, 2000 and 4000 km s^{-1}, to emphasise any possible trend. As is clear in Fig. 16, in which there are two different rebinning (1000 and 4000 km s^{-1}) in A500, there seems to be a trend, in which the number of companions increases as the FWHM(Hβ) increases. This trend means that AGN with broader FWHM(Hβ) have more companions with respect to AGN with narrower FWHM(Hβ), in the sample selected. These results are visible also at different scales: in A250 and A100.

To support the trend visible by eye, we take a look at the statistical results in Table 3. All the three tests performed, for each area, return a slightly positive correlation value, and a p-value which reject the null hypothesis, being very close to 0 in all cases. It should be noted that the correlation value decreases reducing the search area. Such decrease can be justified knowing that the number of companions is larger in A500 than in A100, so the difference in the number of companions between sources with smaller and higher FWHM(Hβ) is larger in A500 with respect to in A100. In addition, it is well known that at very large scale the environment tends to be uniform, as it tends to be uniform

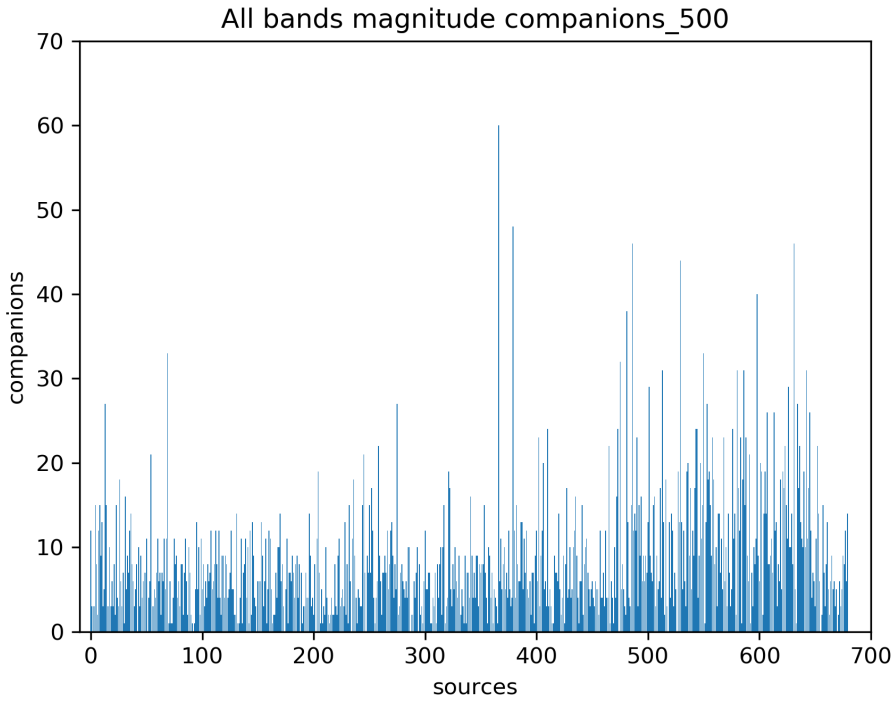

Figure 14: Sources order vs n°companions, all filters simultaneously, magnitude selection, A500.

at galaxy length scale, since at galaxy length scale the only object which is present is the galaxy itself. Therefore, this is an indirect demonstration that the range in areas, from A500 to A100, which I selected emphasize at best the variation of the local environment.

In Fig. 17 it is shown that, on average in the sample used, population B sources have a larger number of companions than population A sources, which is in accordance with the previous results. Fig. 17 has been made in A500, but similar results have been obtained in A250 and A100.

I plotted the companions' distribution for several subsamples (pop.A, pop.B, A4 and B1++), companion bins (with a width of 5 and 2 companions) and areas (A500, A250 and A100). I used the companions' distributions of pop.A and pop.B, and A4 and B1++, as inputs for the K-S and A-D statistical tests. It is visible both by eye (Fig. 18 and Fig. 19) and by looking at the statistical test results in Table 4, that the companions' distributions compared time by time are similar to each other. All the resulting p-values are larger than the chosen threshold, and so the null hypothesis cannot be rejected. In this case it seems that the companions' distributions are similar for each couple of subsamples used. Even if the p-values remain above the chosen threshold, they increase and tend to the limit values when we go from A500 to A100. When the p-values become equal to the limit values (1 for K-S test and 0.25 for A-D test), it does not mean that the two distributions compared are perfectly equal, but that the input values are too few to be used for these tests.

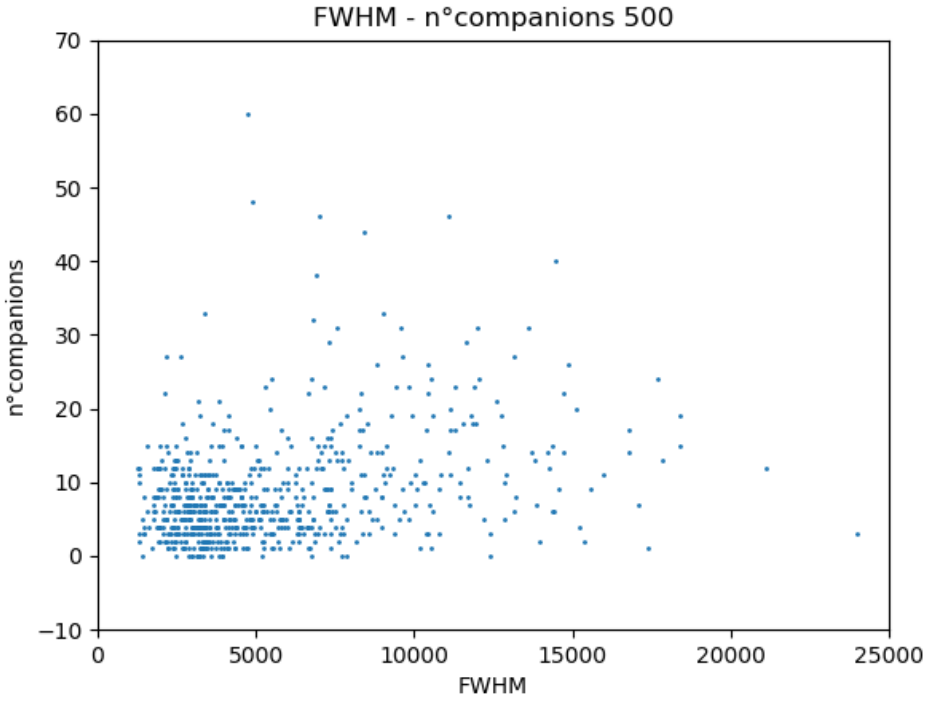

Figure 15: FWHM(Hβ) order vs n°companions, magnitude selection, A500.

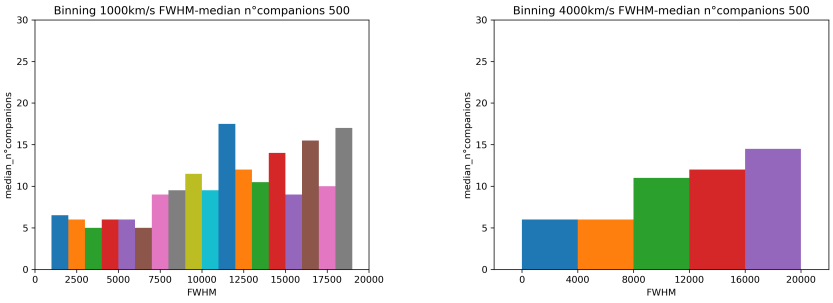

Figure 16: FWHM(Hβ) binned vs median n°companions, bins=1000 and 4000 km s^{-1}, magnitude selection, A500.

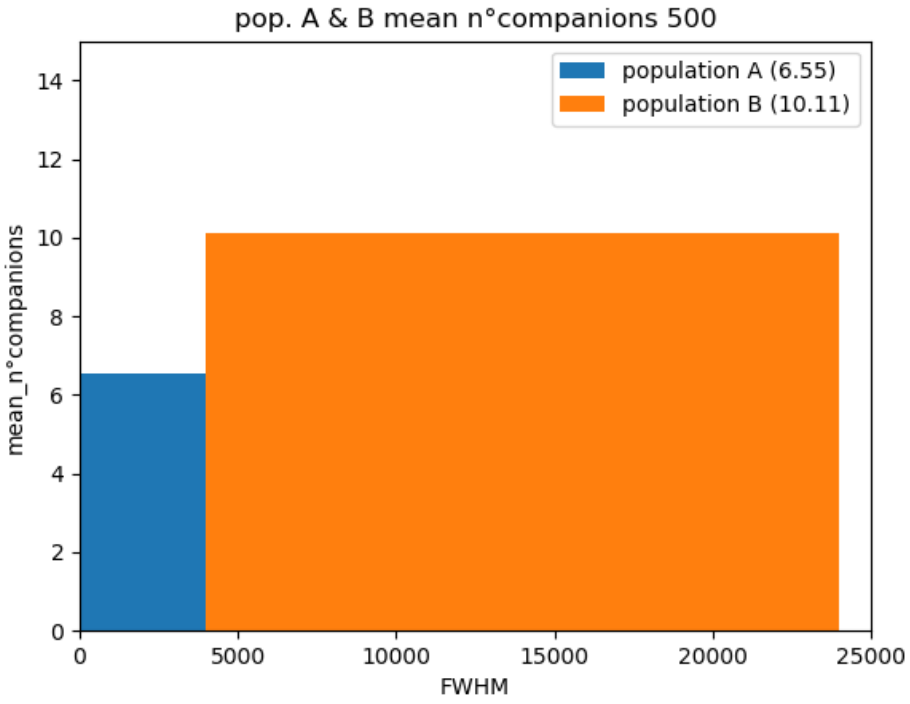

Figure 17: Mean number of companions for population A and B, magnitude selection, A500.

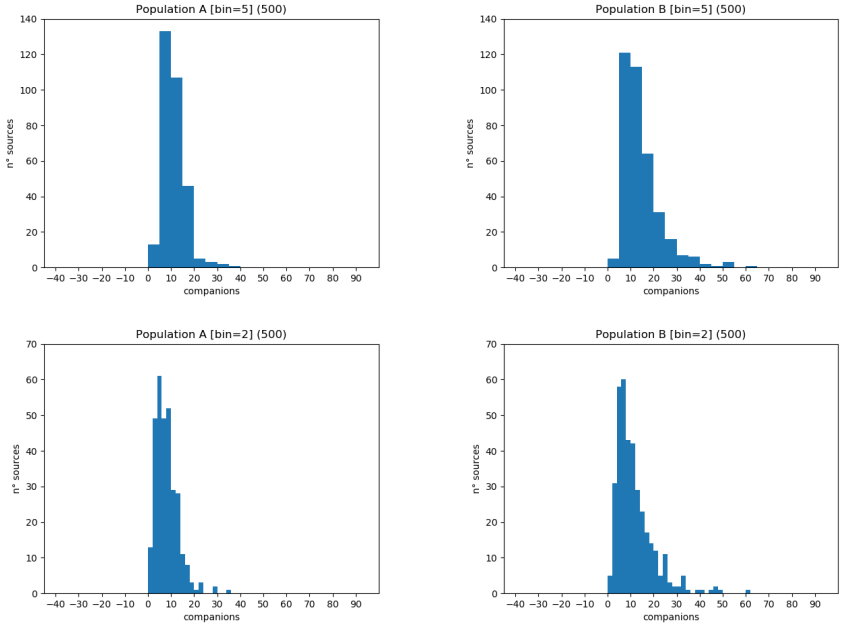

Figure 18: Companions' distribution, *top-left:* pop.A and bin=5, *top-right:* pop.B and bin=5, *bottom-left:* pop.A and bin=2, *bottom-right:* pop.B and bin=2; magnitude selection, A500.

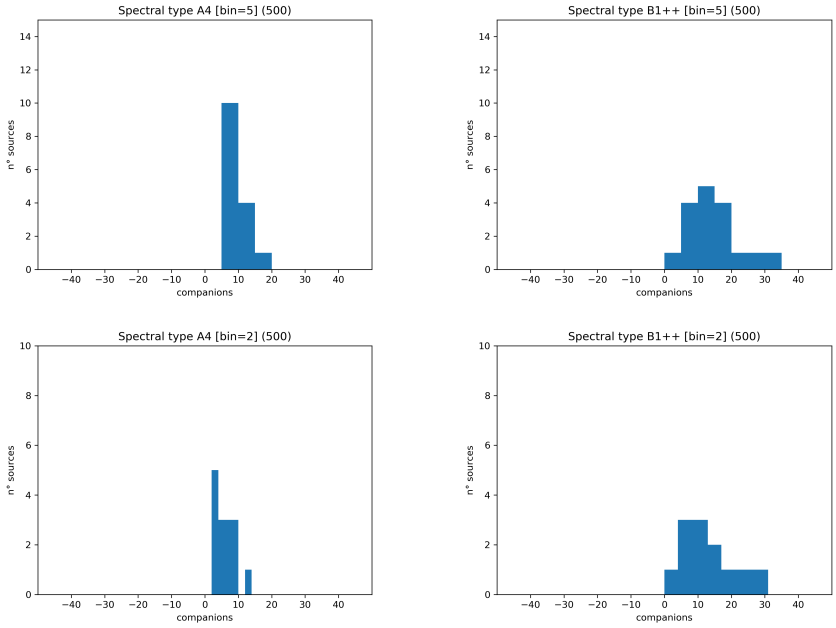

Figure 19: Companions' distribution, *top-left:* A4 sources and bin=5, *top-right:* B1++ sources and bin=5, *bottom-left:* A4 sources and bin=2, *bottom-right:* B1++ sources and bin=2; magnitude selection, A500.

4.2 PHOTOMETRIC REDSHIFT SELECTION

Once I retrieved the photometric redshift using Tarrío and Zarattini (2020) algorithm, I selected the close companions. I plotted the chosen objects with the photometric selection method, ordered according to the FWHM(Hβ) of the principal sources (Fig. 20). Using this method an AGN has at most four galaxies in the searched area, which is a number totally different with respect to those found with the magnitude selection method.

Looking at the results in Table 5 it is clear that basically there is no correlation between the FWHM(Hβ) of the sources in the original sample and the number of companions selected. In addition, all the p-values are greater than 0.1, so in any case the correlation values would not be statistically significant.

I plotted the median instead of the number of companions, dividing the FWHM(Hβ) in x-axis in different bins. Due to the small number of companions, and since there are several sources which have zero companions, frequently the median value is equal to zero, as is visible in Fig. 21. This phenomenon is pretty evident when wide bins are used, like 4000 km s^{-1}. Indeed, the only bin with a value different from zero is the one between 16 000 < FWHM(Hβ) < 20 000 km s^{-1}. By eye it seems that a positive trend is present. With good certainty, it can be said that this trend is not reliable, because of the very low number of companions with which the median is calculated.

A similar interpretation can be given for the plot in Fig. 22, showing the mean number of companions for populations A and B. In addition, if there had

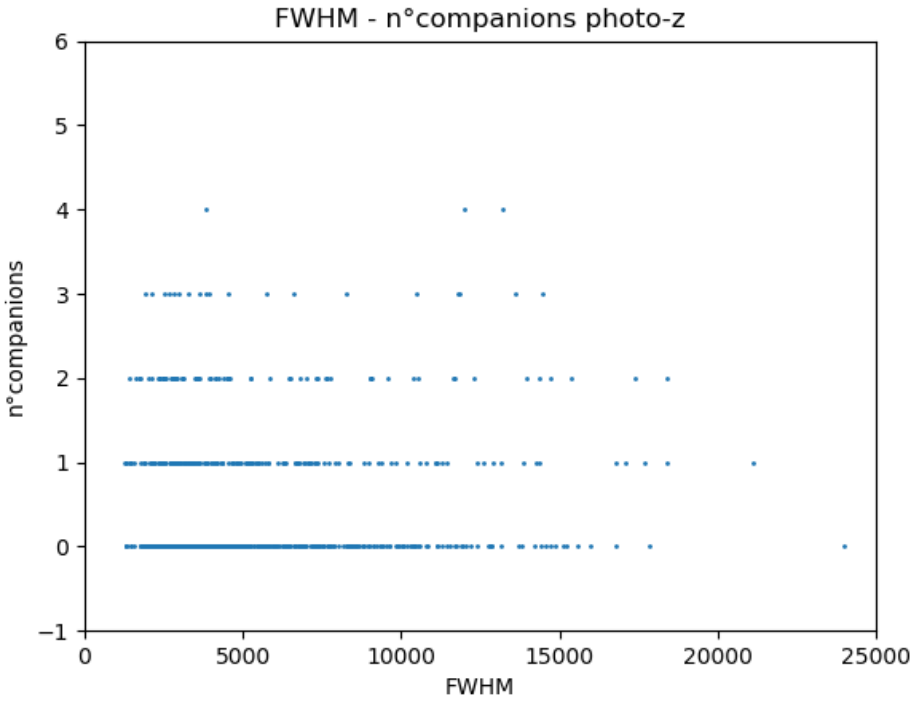

Figure 20: FWHM(Hβ) order vs n°companions, photometric redshift selection, A500.

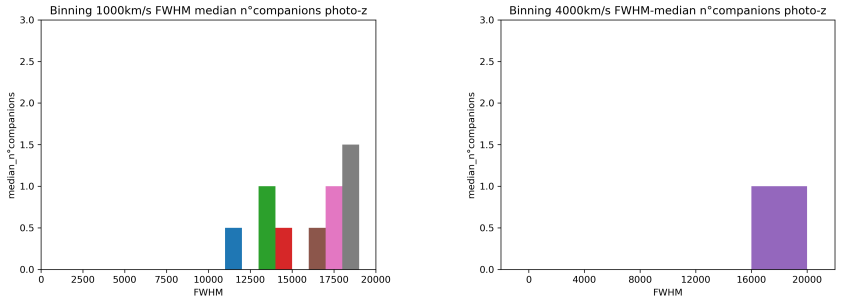

Figure 21: FWHM(Hβ) binned vs median n°companions, bins=1000 and 4000 km s^{-1}, photometric redshift selection, A500.

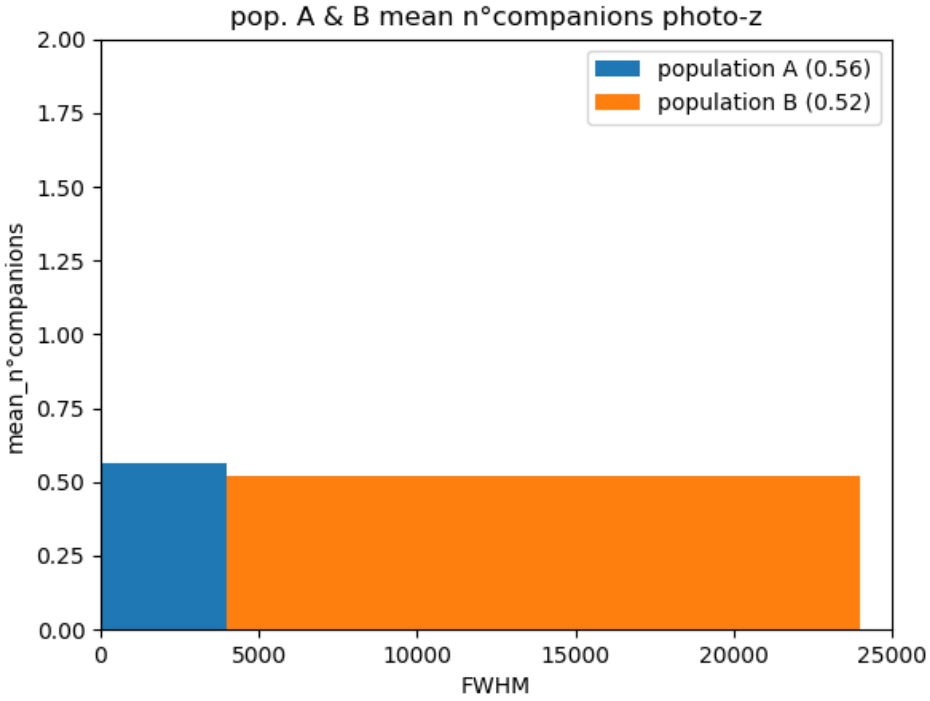

Figure 22: Mean number of companions for population A and B, photometric redshift selection, A500.

been a trend here, it should have had a negative slope, which is completely in contrast with the previous chart.

Also here, as in the magnitude selection, I did several statistical tests using the companions' distribution. In Fig. 23 and in Fig. 24 can be seen the various companions' distributions used. The results of the K-S and A-D tests in Table 6 are completely useless, all the p-values are equal to the upper limit values of the corresponding test. This does not mean that the real companions' distributions are totally equal, but it means that the inputs are not sufficient. Indeed, all the distributions have a very small width, because of the few companions selected, and so they are not suitable for statistical tests like the ones I used.

4.3 DENSITY APPROACH

Density approach method is slightly different with respect to the previous methods since it does not really apply a selection, but it makes a correction using very large-scale number density. Fig. 25 shows the number of galaxies in an area with a radius of 30 arcmin, centered in each source of the original sample. It can be noticed that the number of objects in this area is pretty homogeneous (around ~20 000 - 25 000 sources), so this means that the area selected is large enough for density correction.

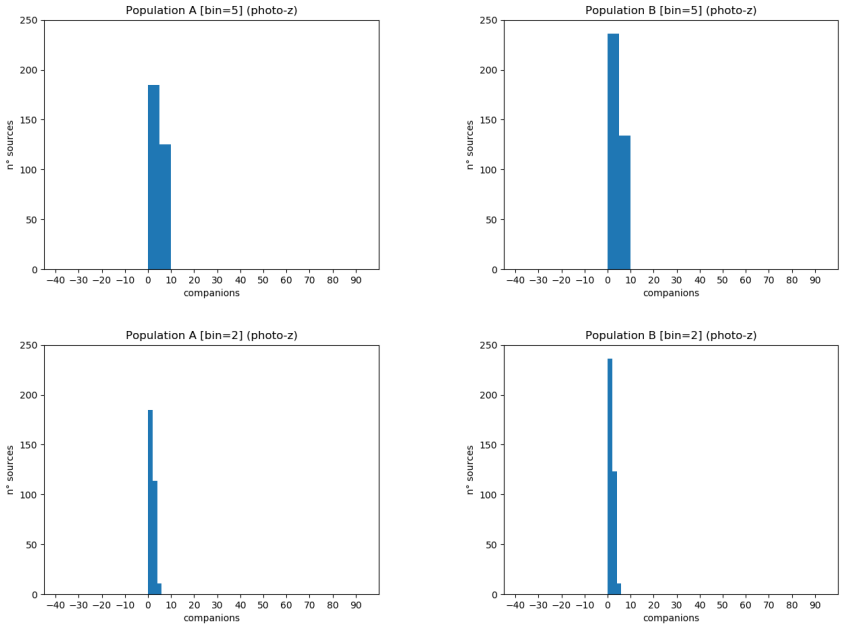

Figure 23: Companions' distribution, *top-left:* pop.A and bin=5, *top-right:* pop.B and bin=5, *bottom-left:* pop.A and bin=2, *bottom-right:* pop.B and bin=2; photometric redshift selection, A500.

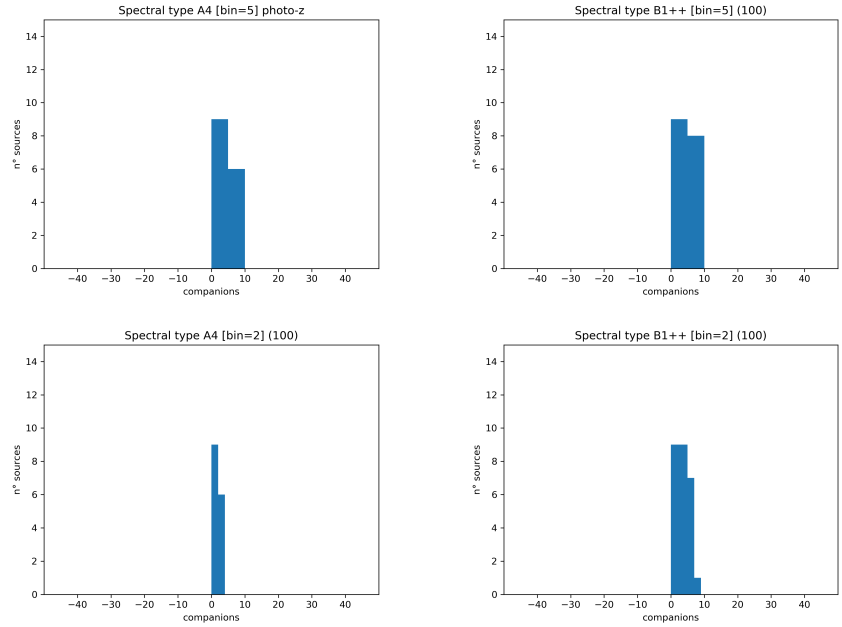

Figure 24: Companions' distribution, *top-left:* A4 sources and bin=5, *top-right:* B1++ sources and bin=5, *bottom-left:* A4 sources and bin=2, *bottom-right:* B1++ sources and bin=2; photometric redshift selection, A500.

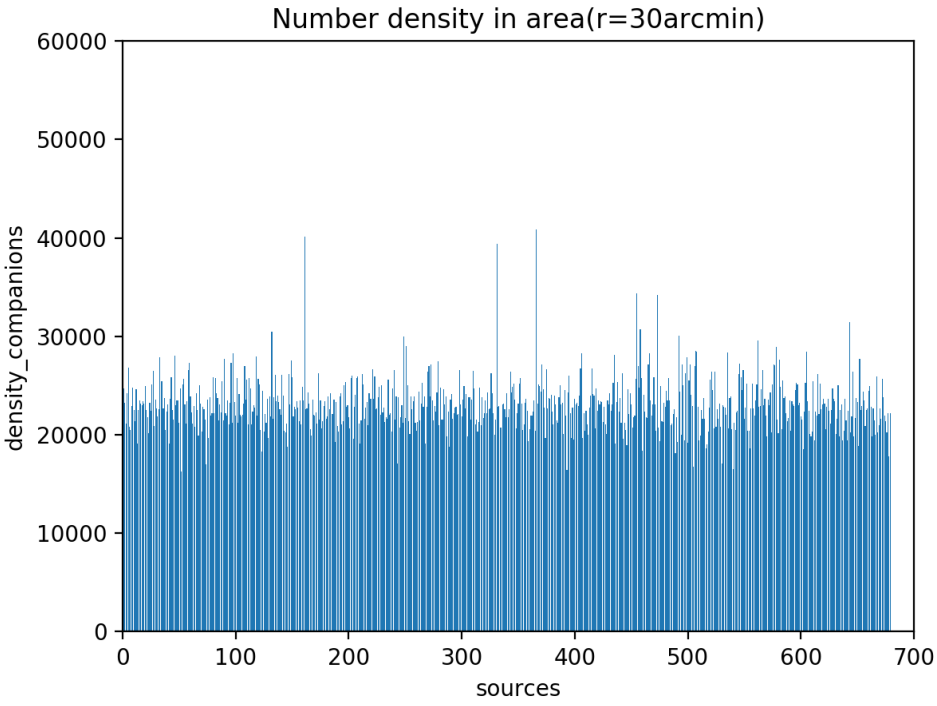

Figure 25: Source order vs n°objects in area(r=30arcmin), density approach.

After subtracting the rescaled number density in A500, A250 and A100, I plotted the results in three scatter plots. In Fig. 26 is shown the scatter plot using in A500. As I already said, in this method, also a negative number of companions can result. This happens because I carried out an environment comparison between the searched areas selected and the very large area, and not calculations to find the exact number of companions. Looking at the Fig. 26 no visible trend seems to be present. To confirm the results visible by eye, we take a look at the obtained statistical results in Table 7. In all the three areas analysed there are no evident correlations, since the correlation values are all very close to 0. Moreover, these correlation values are not statistically significant due to the high resulting p-values.

In addition, I divided the number of sources by the number density, obtaining the fractional overdensity. In this case, in Fig. 27 it is shown that the spread in y-axis increases a bit while reducing the searched area. However, the result is basically the same: none trend seems to be visible.

As in the previous methods I plotted the median value of companions defining a binning in the FWHM(Hβ) of 1000, 2000 and 4000 km s^{-1}. The results that I obtained are in contradiction with each other. Indeed, for some bin widths and areas a positive trend seems to be present, for some other a negative one, and in some cases none trend is visible. Fig. 28 supports such hypothesis.

I did a couple of tests to see if there are any anomalies, before dividing the sources in population A and B subsamples for the searched area. First of all, I plotted, in a histogram, the number of objects in the large-scale area around

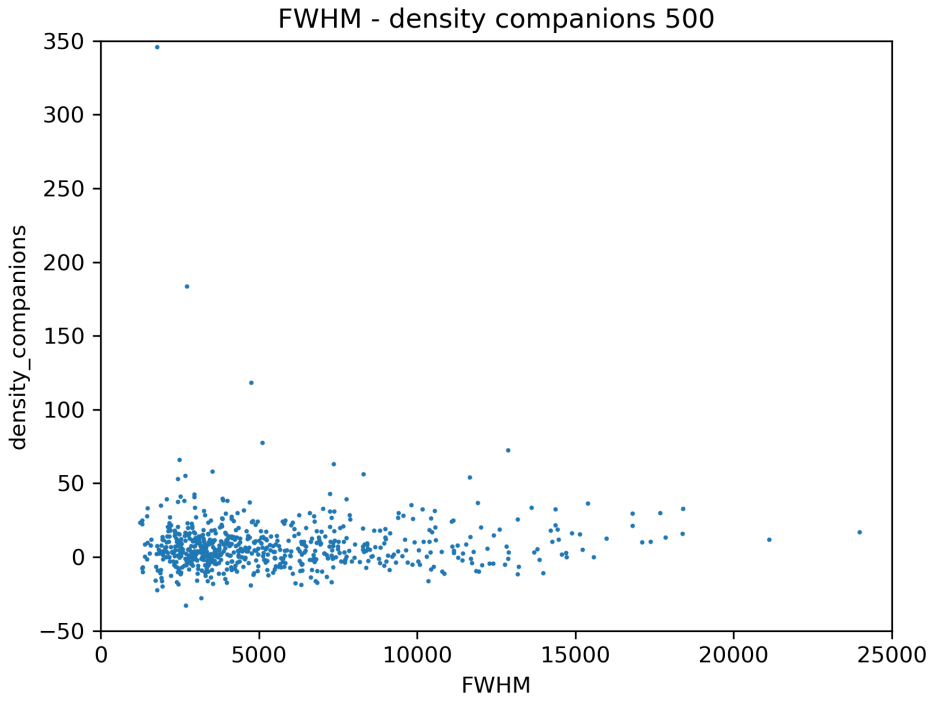

Figure 26: FWHM(Hβ) order vs n°companions, density approach, A500.

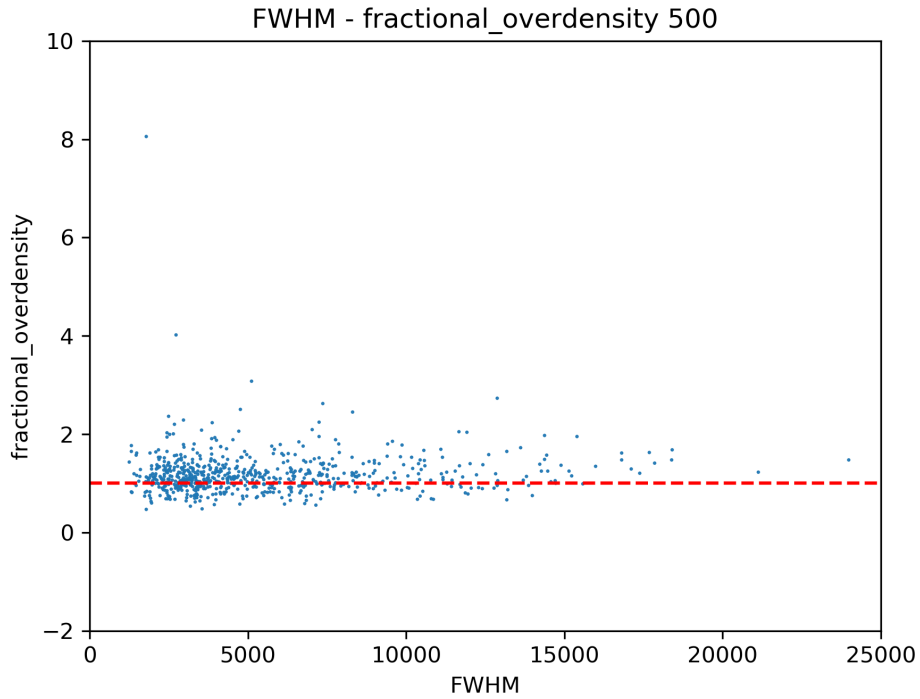

Figure 27: FWHM(Hβ) order vs fractional overdensity, density approach, A500.

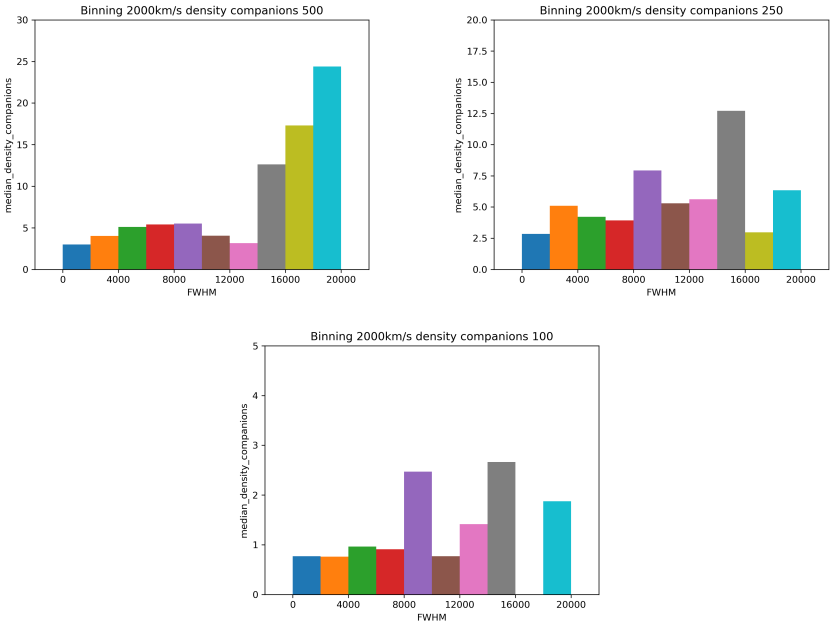

Figure 28: FWHM(Hβ) binned vs median n°companions, bins=2000 km s^{-1}, density approach, A500, A250 and A100.

population A and B sources. Second, I performed a Mann-Whitney U-test for the same number of objects used in the plot. In Fig. 29 it is shown that the number of galaxies around population A and B AGN is basically the same, considering the error bars. Same result are achieved with the test (Table 9), since I obtained a p-value larger than the threshold chosen. This means that the distribution of galaxies in large-scale area around population A and B is the same, as it should be.

At this stage, the mean value and the fractional overdensity of the companions for population A and B was analysed. To do so I plotted several histograms for population A and B sources. In Fig. 30 and in Fig. 31 it is shown that the mean value of companions is larger for population A in A500, and in A100, and larger for population B in A250. Instead, the fractional overdensity is equal, considering the error bars, for population A and B in all the three areas. Therefore, here again no clear trend is visible.

I did several K-S and A-D statistical tests for the companions' distributions in Fig. 32 and in Fig. 33. Looking at the results in Table 8, all the p-values are well beyond the chosen threshold, so the null hypothesis cannot be rejected. In accordance with these values, the companions' distributions of populations A and B, and A4 and B1++ sources, are similar to each other. The statistical test results obtained considering A4 and B1++ sources are almost equal to the limit values. However, by eye, especially in A500, the distributions are not very similar. The few data used as input in the statistical tests can partially explain the p-values obtained. Therefore, it cannot be said that these p-values are completely reliable.

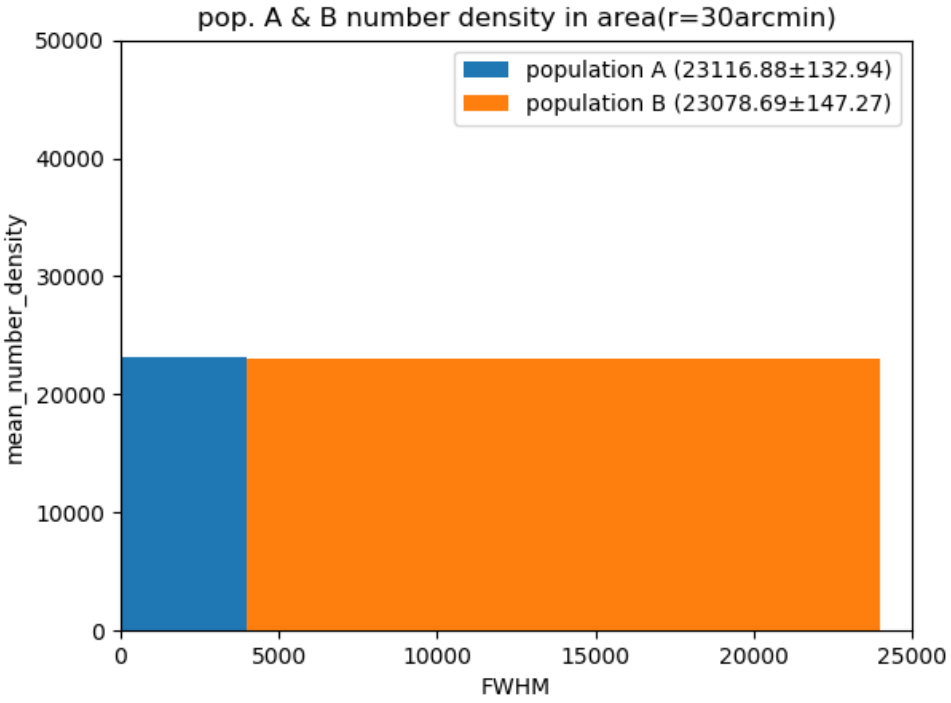

Figure 29: Number of companions in area(r=30arcmin) for population A and B, density approach.

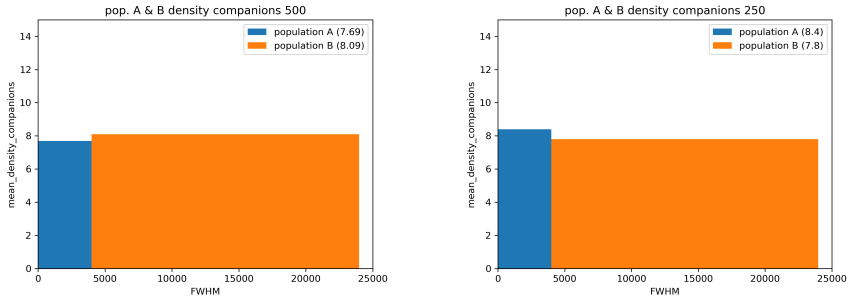

Figure 30: Mean number of companions for population A and B, density approach, A500 and A250.

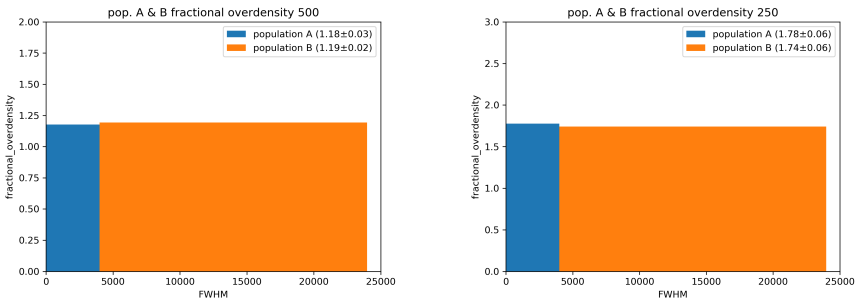

Figure 31: Fractional overdensity of the mean number of companions for population A and B, density approach, A500 and A250.

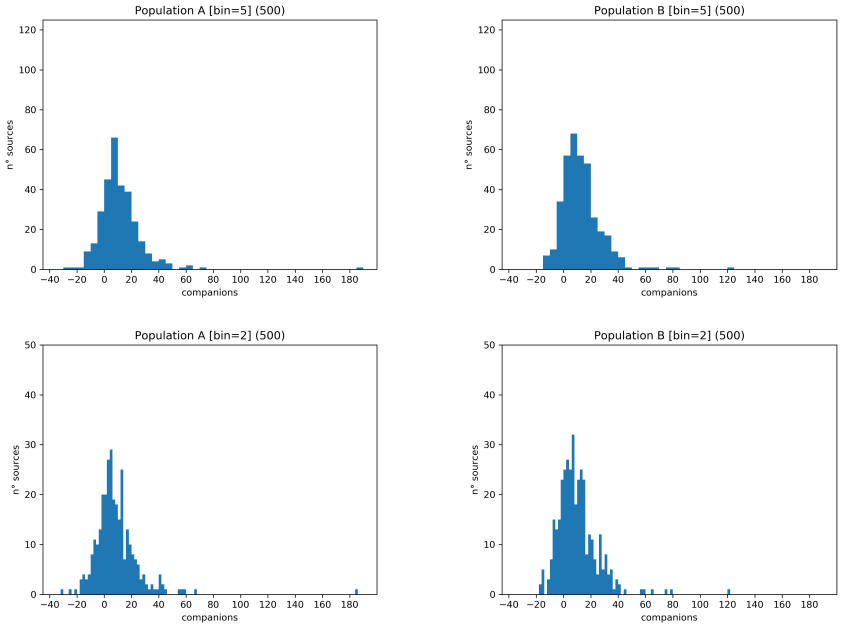

Figure 32: Companions' distribution, *top-left:* pop.A and bin=5, *top-right:* pop.B and bin=5, *bottom-left:* pop.A and bin=2, *bottom-right:* pop.B and bin=2; density approach, A500.

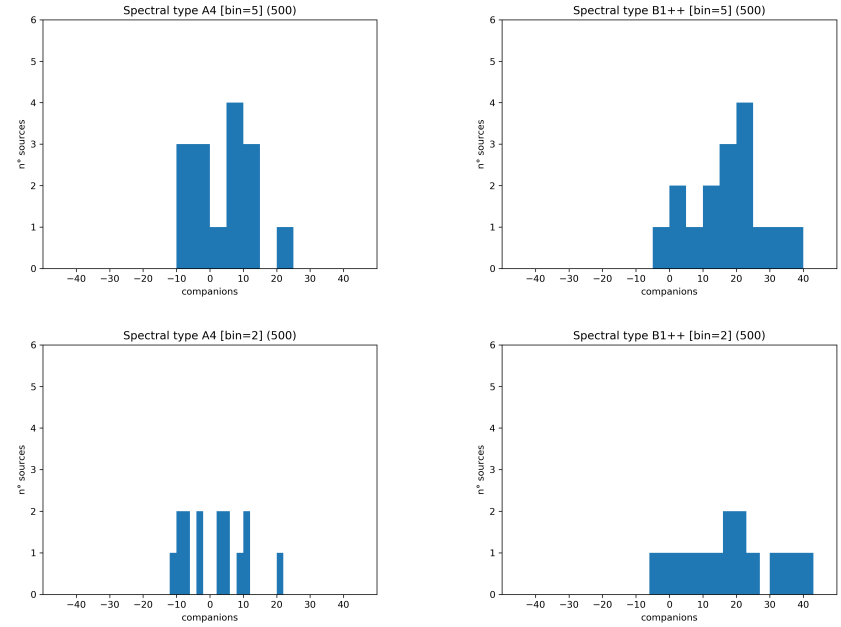

Figure 33: Companions' distribution, *top-left:* A4 sources and bin=5, *top-right:* B1++ sources and bin=5, *bottom-left:* A4 sources and bin=2, *bottom-right:* B1++ sources and bin=2; density approach, A500.

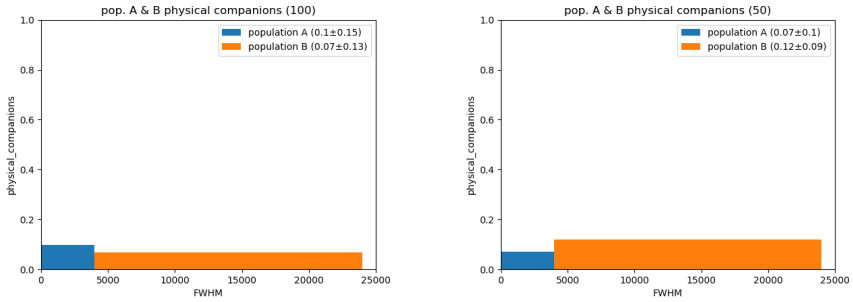

Figure 34: Fraction of sources with physical companions for population A and B, A100 and A50.

4.3.1 *Physical companions*

In Fig. 34 I plotted the fraction of population A and B sources with physical companions in A100 and A50. In A100 area, 10% of population A has at least one companion versus 7% of population B, but the values are the same within the errors. In A50 area a similar situation is present, indeed 7% of population A has at least one companion versus 12% of population B, but also in this case they are the same within errors.

4.4 SAMPLE ANALYSIS

Looking at the statistical results in Table 11, it is clear that the p-value associated to the spectroscopic redshift is just above the threshold chosen, and the p-value associated to the i-Kron magnitude is well below such threshold. The threshold that I set is of 95%, namely a p-value equal to 0.0125. This means that the spectroscopic redshift distributions of population A and B are similar to each other. It is a good result, since it means that the sources inside the two sample were chosen using similar criteria. Considering the i-Kron magnitude, it seems that the two distributions are different in population A and B. This difference is supported also by the mean i-Kron magnitude values. Indeed, the mean value for the population A (17.18317±0.02729) is different respect the same value for population B (17.60326±0.03424).

5

SUMMARY AND CONCLUSIONS

In this thesis, I compared the environments around a sample of AGN spread along the MS, using the companions residing in three areas with radii of 500, 250, and 100 kpc. The sample used was selected in Marziani et al. (2013), and I retrieved the necessary data from the PS1 survey, in all the five bands available (g, r, i, z and y). After a galaxies-stars separation, to get rid of all the stars in the field, I used three selection methods to identify the companions.

The method, introduced in Rafanelli and Marziani (1992), which is a magnitude selection method, gives the most interesting results in the present analysis. Indeed, I found a positive correlation between the FWHM(Hβ) of the sources in the original sample and the number of companions. It means that the populations in the MS with high values of FWHM(Hβ), like B1+ or B1++ sources, have a denser environment than that with lower FWHM(Hβ) values, like population A sources. This positive correlation was found at all the scales analysed. Such an increase in companions is visible also by eye, looking at the plots in which the FWHM(Hβ) axis was subdivided using the three bin widths or dividing it in population A and B, using in both cases the median number of companions in y-axis. In addition, I did several statistical tests to compare the companions' distributions of population A and B, and A4 and B1++ sources. In this case, due to too high p-values, no real difference in the distributions involved is visible. Indeed, the null hypothesis was not rejected. In some cases the p-values are perfectly equal to the limit values. Probably this means that the input values, basically the number of AGN considered in each subsample, are too few to be used in these types of tests. It is visible in Fig. 16, and also at different scales, that there is a clear threshold in the FWHM(Hβ) at about 7500-8000 km s^{-1}, above which the number of companions is higher than at lower FWHM(Hβ). Panda, Marziani, and Czerny (2019) found that above the same FWHM(Hβ) threshold, the different characteristics in the spectral types are not mainly due to an higher observation angle but are due to increasing BH masses. To explain these two phenomena it can be hypothesised that a denser environment can induce more frequent interactions, that result in a more gas to feed the central BH. Studies like those in Järvelä et al. (2017) support this idea. It is worth noting that this scenario is still hypothetical, and it needs more confirmations. As follow-up, statistical tests which relate the BH mass with the number of companions can be done.

Photometric redshift selection requires the Tarrío and Zarattini (2020) algorithm, which identifies the photometric redshift using the magnitudes in the five PS1 filters. Considering the results, this method gave very different results with respect to the other methods that I used. The algorithm calculated the redshift information in just over 50% of cases, and very few sources were selected as close companions according to the selection criteria considered. The three statistical tests performed did not found any evident correlations,

because the correlation values are very close to zero, and in any case the p-values are above the chosen threshold. In addition, also the plots made for the number of companions, mean number of companions in population A and B, and median number of companions considering rebinned FWHM(Hβ), give contradictory results with respect to each other. By eye, the companions' distributions that I plotted are very similar to each other, and also the resulting p-values are all equal to the limit values reachable in the test typologies used. The problems of these resulting p-values are not only due to the few number of sources, but also, in this case, they are due to the very few number of companions selected. Therefore, using photometric redshift selection I did not manage to compare the environment of the AGN in the sample, due to the different results obtained with respect to the other methods.

When using the density approach I performed a sort of correction knowing large-scale number density information, instead than a real selection. To retrieve the large-scale number density I used an area with a radius of 30 arcmin around each source. Both by eye and using statistical tests, no correlation between the FWHM(Hβ) and the number of companions seems to be present. In addition I used the fractional overdensity, to emphasize any possible difference in the environments, but no particular differences were found for the different spectral types. I subdivided also here the FWHM(Hβ) using different bins, and I performed several K-S and A-D tests. The p-values resulting are well beyond the chosen threshold, and then the null hypothesis cannot be rejected. Especially using A4 and B1++ subsamples the statistical tests have p-values almost always close to the limit values, even if by eye the distributions are different from each other. In particular such problem can be attributed to the few data available for the subsamples. This method did not give us the results expected, maybe due to some biases which have not been properly taken into account. A different approach in some phases of this procedure could be useful to obtain better results.

I calculated and compared the fraction of population A and B sources with physical companions in A100 and A50. No differences are found between the two subsamples, which means that no population shows an excess of companions in the local environment compared to the other.

In addition to the correlation found in the first part of magnitude selection, no other evident relations were discovered. In particular, no other K-S and A-D tests gave results that allowed me to reject the null hypothesis. The first reason is that the photometric redshift selection gave particular results which have to be properly analysed. Indeed, in this method I had few photometric redshifts available and even fewer companions selected. Even if at most four companions can even be the real number of companions, around a source in the sample, such data is completely in contradiction with the other selection methods. Probably in the photometric redshift selection a more careful analysis of all the possible biases would be necessary. The second reason is that sometimes I selected too small subsamples, which contain few sources. Few input data are problematic for the statistical tests, in particular for the K-S and A-D tests, because they could give misleading results in such conditions.

There are several ways to solve these problems. The most obvious solution is to use a larger sample, which results in larger subsamples. An example could be to include A3 in the A4 subsample selected for the companion distributions, since they show similar extreme characteristics (Ganci et al., 2019). Another thing is to compare all the different spectral types along the MS, to discovered every possible relation, and then understand if such relations are connected to physical characteristics. In addition, different statistical tests could be useful to compare the results obtained with those already used.

I must point out that a difference in the i-Kron magnitude for population A and B sources was found. Therefore, a more detailed analysis to study its impact in the correlation found in magnitude selection is needed, but it is outside of the scope of this thesis.

Some follow-up can be suggested, which can be done to improve and complete the analysis started in this thesis. A possibility is to test the validity of photometric redshift data by retrieving the spectroscopic redshift for a selected sample of companions. This step was not possible using the accessible facilities, since the majority of galaxies selected are very faint, so large optical telescopes are required. For the magnitude selection I could use different search areas, with radius like in Rafanelli, Violato, and Baruffolo (1995) that was equal to three times the diameter of the AGN host considered, and a different range in magnitude. Comparing several search areas could be useful also in the density approach. In addition to all the methods I could make position charts, which are basically two-dimensional plots like maps of the sky, to analyse the different arrangements of the galaxies. A similar analysis as what we did for the fraction of sources with physical companions can be done comparing different subsamples, like A4 and B1+ or B1++. Finally, by adopting a control sample I could compare the results obtained with those already present in the literature, to improve our knowledge about AGN environment in the Universe.

BIBLIOGRAPHY

Abramowicz, M. A., B. Czerny, J. P. Lasota, and E. Szuszkiewicz (Sept. 1988). "Slim Accretion Disks." In: 332, p. 646. DOI: 10.1086/166683.

Adhikari, T. P., K. Hryniewicz, A. Różańska, B. Czerny, and G. J. Ferland (Mar. 2018). "Intermediate-line Emission in AGNs: The Effect of Prescription of the Gas Density." In: 856.1, 78, p. 78. DOI: 10.3847/1538-4357/aab350. arXiv: 1803.00090 [astro-ph.GA].

Allen, S. W., R. J. H. Dunn, A. C. Fabian, G. B. Taylor, and C. S. Reynolds (Oct. 2006). "The relation between accretion rate and jet power in X-ray luminous elliptical galaxies." In: 372.1, pp. 21–30. DOI: 10.1111/j.1365-2966.2006.10778.x. arXiv: astro-ph/0602549 [astro-ph].

Antonucci, R. R. J. and J. S. Miller (Oct. 1985). "Spectropolarimetry and the nature of NGC 1068." In: 297, pp. 621–632. DOI: 10.1086/163559.

Antonucci, Robert (Jan. 1993). "Unified models for active galactic nuclei and quasars." In: 31, pp. 473–521. DOI: 10.1146/annurev.aa.31.090193.002353.

Bahcall, Neta A. (Nov. 1996). "Clusters and superclusters of galaxies." In: *arXiv e-prints*, astro-ph/9611148, astro–ph/9611148. arXiv: astro-ph/9611148 [astro-ph].

Baldwin, Jack A. (June 1977). "Luminosity Indicators in the Spectra of Quasi-Stellar Objects." In: 214, pp. 679–684. DOI: 10.1086/155294.

Barger, A. J., L. L. Cowie, R. F. Mushotzky, Y. Yang, W. H. Wang, A. T. Steffen, and P. Capak (Feb. 2005). "The Cosmic Evolution of Hard X-Ray-selected Active Galactic Nuclei." In: 129.2, pp. 578–609. DOI: 10.1086/426915. arXiv: astro-ph/0410527 [astro-ph].

Barnes, Joshua E. and Lars E. Hernquist (Apr. 1991). "Fueling Starburst Galaxies with Gas-rich Mergers." In: 370, p. L65. DOI: 10.1086/185978.

Barth, Aaron J., Misty C. Bentz, Jenny E. Greene, and Luis C. Ho (Aug. 2008). "An Offset Seyfert 2 Nucleus in the Minor Merger System NGC 3341." In: 683.2, p. L119. DOI: 10.1086/591905. arXiv: 0807.3314 [astro-ph].

Beck, Róbert, László Dobos, Tamás Budavári, Alexander S. Szalay, and István Csabai (Aug. 2016). "Photometric redshifts for the SDSS Data Release 12." In: 460.2, pp. 1371–1381. DOI: 10.1093/mnras/stw1009. arXiv: 1603.09708 [astro-ph.GA].

Beckmann, Volker and Chris R. Shrader (2012). *Active Galactic Nuclei*. Provided by the SAO/NASA Astrophysics Data System. URL: https://ui.adsabs.harvard.edu/abs/2012agn..book.....B.

Bennert, Nicola, Heino Falcke, Yuri Shchekinov, and Andrew S. Wilson (Nov. 2004). "Comparing AGN broad and narrow line regions." In: *The Interplay Among Black Holes, Stars and ISM in Galactic Nuclei*. Ed. by Thaisa Storchi-Bergmann, Luis C. Ho, and Henrique R. Schmitt. Vol. 222, pp. 307–308. DOI: 10.1017/S1743921304002340. arXiv: astro-ph/0404278 [astro-ph].

Bernardeau, F., S. Colombi, E. Gaztañaga, and R. Scoccimarro (Sept. 2002). "Large-scale structure of the Universe and cosmological perturbation theory." In: 367.1-3, pp. 1–248. DOI: 10.1016/S0370-1573(02)00135-7. arXiv: astro-ph/0112551 [astro-ph].

Blandford, R. D. and R. L. Znajek (May 1977). "Electromagnetic extraction of energy from Kerr black holes." In: 179, pp. 433–456. DOI: 10.1093/mnras/179.3.433.

Bond, J. Richard, Lev Kofman, and Dmitry Pogosyan (Apr. 1996). "How filaments of galaxies are woven into the cosmic web." In: 380.6575, pp. 603–606. DOI: 10.1038/380603a0. arXiv: astro-ph/9512141 [astro-ph].

Boroson, Todd A. (Jan. 2002). "Black Hole Mass and Eddington Ratio as Drivers for the Observable Properties of Radio-loud and Radio-quiet QSOs." In: 565.1, pp. 78–85. DOI: 10.1086/324486. arXiv: astro-ph/0109317 [astro-ph].

Boroson, Todd A. and Richard F. Green (May 1992). "The Emission-Line Properties of Low-Redshift Quasi-stellar Objects." In: 80, p. 109. DOI: 10.1086/191661.

Brown, Michael J. I. et al. (Feb. 2006). "The 1 < z < 5 Infrared Luminosity Function of Type I Quasars." In: 638.1, pp. 88–99. DOI: 10.1086/498843. arXiv: astro-ph/0510504 [astro-ph].

Butler, Andrew et al. (Nov. 2018). "The XXL Survey. XXXI. Classification and host galaxy properties of 2.1 GHz ATCA XXL-S radio sources." In: 620, A16, A16. DOI: 10.1051/0004-6361/201732379. arXiv: 1804.05983 [astro-ph.GA].

Cardamone, Carolin N., K. Schawinski, K. Masters, C. Lintott, and L. Fortson (May 2011). "Galaxy Zoo: The Connection between AGN Activity and Bars in Late Type Galaxies." In: *American Astronomical Society Meeting Abstracts #218*. Vol. 218. American Astronomical Society Meeting Abstracts, 206.03, p. 206.03.

Chambers, K. C. et al. (Dec. 2016). "The Pan-STARRS1 Surveys." In: *arXiv e-prints*, arXiv:1612.05560, arXiv:1612.05560. arXiv: 1612.05560 [astro-ph.IM].

Chen, Yen-Chi, Shirley Ho, Rachel Mandelbaum, Neta A. Bahcall, Joel R. Brownstein, Peter E. Freeman, Christopher R. Genovese, Donald P. Schneider, and Larry Wasserman (Apr. 2017). "Detecting effects of filaments on galaxy properties in the Sloan Digital Sky Survey III." In: 466.2, pp. 1880–1893. DOI: 10.1093/mnras/stw3127. arXiv: 1509.06376 [astro-ph.GA].

Cirasuolo, M., M. Magliocchetti, A. Celotti, and L. Danese (May 2003). "The radio-loud/radio-quiet dichotomy: news from the 2dF QSO Redshift Survey." In: 341.3, pp. 993–1004. DOI: 10.1046/j.1365-8711.2003.06485.x. arXiv: astro-ph/0301526 [astro-ph].

Cooray, Asantha and Ravi Sheth (Dec. 2002). "Halo models of large scale structure." In: 372.1, pp. 1–129. DOI: 10.1016/S0370-1573(02)00276-4. arXiv: astro-ph/0206508 [astro-ph].

Cracco, V., S. Ciroi, F. di Mille, L. Vaona, A. Frassati, A. A. Smirnova, G. La Mura, A. V. Moiseev, and P. Rafanelli (Dec. 2011). "The origin of gas in extended narrow-line regions of nearby Seyfert galaxies - I. NGC 7212."

In: 418.4, pp. 2630–2641. DOI: 10.1111/j.1365-2966.2011.19654.x. arXiv: 1109.1195 [astro-ph.CO].

Croom, Scott M. et al. (Nov. 2009). "The 2dF-SDSS LRG and QSO survey: the QSO luminosity function at 0.4 < z < 2.6." In: 399.4, pp. 1755–1772. DOI: 10.1111/j.1365-2966.2009.15398.x. arXiv: 0907.2727 [astro-ph.CO].

Croton, Darren J. (Oct. 2013). "Damn You, Little h! (Or, Real-World Applications of the Hubble Constant Using Observed and Simulated Data)." In: 30, e052, e052. DOI: 10.1017/pasa.2013.31. arXiv: 1308.4150 [astro-ph.CO].

Curtis, H. D. (Jan. 1918). "Descriptions of 762 Nebulae and Clusters Photographed with the Crossley Reflector." In: *Publications of Lick Observatory* 13, pp. 9–42.

Dahari, O. (July 1984). "Companions of Seyfert galaxies : a statistical survey." In: 89, pp. 966–974. DOI: 10.1086/113591.

Di Matteo, Tiziana, Volker Springel, and Lars Hernquist (Feb. 2005). "Energy input from quasars regulates the growth and activity of black holes and their host galaxies." In: 433.7026, pp. 604–607. DOI: 10.1038/nature03335. arXiv: astro-ph/0502199 [astro-ph].

Dressler, A. (Mar. 1980). "Galaxy morphology in rich clusters: implications for the formation and evolution of galaxies." In: 236, pp. 351–365. DOI: 10.1086/157753.

Dultzin-Hacyan, D., Y. Krongold, I. Fuentes-Guridi, and P. Marziani (Mar. 1999). "The Close Environment of Seyfert Galaxies and Its Implication for Unification Models." In: 513.2, pp. L111–L114. DOI: 10.1086/311925. arXiv: astro-ph/9901227 [astro-ph].

Dunlop, J. S., R. J. McLure, M. J. Kukula, S. A. Baum, C. P. O'Dea, and D. H. Hughes (Apr. 2003). "Quasars, their host galaxies and their central black holes." In: 340.4, pp. 1095–1135. DOI: 10.1046/j.1365-8711.2003.06333.x. arXiv: astro-ph/0108397 [astro-ph].

Ebeling, H., L. N. Stephenson, and A. C. Edge (Feb. 2014). "Jellyfish: Evidence of Extreme Ram-pressure Stripping in Massive Galaxy Clusters." In: 781.2, L40, p. L40. DOI: 10.1088/2041-8205/781/2/L40. arXiv: 1312.6135 [astro-ph.GA].

Einasto, M., H. Lietzen, E. Tempel, M. Gramann, L. J. Liivamägi, and J. Einasto (Feb. 2014). "SDSS superclusters: morphology and galaxy content." In: 562, A87, A87. DOI: 10.1051/0004-6361/201323111. arXiv: 1401.3226 [astro-ph.CO].

Einstein, A. (Jan. 1916). "Die Grundlage der allgemeinen Relativitätstheorie." In: *Annalen der Physik* 354.7, pp. 769–822. DOI: 10.1002/andp.19163540702.

Ellison, Sara L., David R. Patton, J. Trevor Mendel, and Jillian M. Scudder (Dec. 2011). "Galaxy pairs in the Sloan Digital Sky Survey - IV. Interactions trigger active galactic nuclei." In: 418.3, pp. 2043–2053. DOI: 10.1111/j.1365-2966.2011.19624.x. arXiv: 1108.2711 [astro-ph.CO].

Faber, S. M. and R. E. Jackson (Mar. 1976). "Velocity dispersions and mass-to-light ratios for elliptical galaxies." In: 204, pp. 668–683. DOI: 10.1086/154215.

Fabian, A. C. (May 2010). "Cosmic Feedback from AGN." In: *Co-Evolution of Central Black Holes and Galaxies*. Ed. by Bradley M. Peterson, Rachel S. Somerville, and Thaisa Storchi-Bergmann. Vol. 267, pp. 341–349. DOI: 10.1017/S1743921310006691. arXiv: 0912.0880 [astro-ph.CO].

Fabian, A. C. et al. (Mar. 2013). "Long XMM observation of the narrow-line Seyfert 1 galaxy IRAS 13224-3809: rapid variability, high spin and a soft lag." In: 429.4, pp. 2917–2923. DOI: 10.1093/mnras/sts504. arXiv: 1208.5898 [astro-ph.HE].

Fabian, Andrew C. and Anthony N. Lasenby (Nov. 2019). "Astrophysical Black Holes." In: *arXiv e-prints*, arXiv:1911.04305, arXiv:1911.04305. arXiv: 1911.04305 [astro-ph.HE].

Fanaroff, B. L. and J. M. Riley (May 1974). "The morphology of extragalactic radio sources of high and low luminosity." In: 167, 31P–36P. DOI: 10.1093/mnras/167.1.31P.

Farrow, Daniel J. et al. (Jan. 2014). "Pan-STARRS1: Galaxy clustering in the Small Area Survey 2." In: 437.1, pp. 748–770. DOI: 10.1093/mnras/stt1933. arXiv: 1310.6366 [astro-ph.CO].

Fraix-Burnet, Didier, Paola Marziani, Mauro D'Onofrio, and Deborah Dultzin (Feb. 2017). "The phylogeny of quasars and the ontogeny of their central black holes." In: *Frontiers in Astronomy and Space Sciences* 4, 1, p. 1. DOI: 10.3389/fspas.2017.00001. arXiv: 1702.02468 [astro-ph.GA].

Fu, Hai, Joshua L. Steffen, Arran C. Gross, Y. Sophia Dai, Jacob W. Isbell, Lihwai Lin, David Wake, Rui Xue, Dmitry Bizyaev, and Kaike Pan (Apr. 2018). "SDSS-IV MaNGA: Galaxy Pair Fraction and Correlated Active Galactic Nuclei." In: 856.2, 93, p. 93. DOI: 10.3847/1538-4357/aab364. arXiv: 1801.00792 [astro-ph.GA].

Gallo, Elena, Tommaso Treu, Philip J. Marshall, Jong-Hak Woo, Christian Leipski, and Robert Antonucci (May 2010). "AMUSE-Virgo. II. Downsizing in Black Hole Accretion." In: 714.1, pp. 25–36. DOI: 10.1088/0004-637X/714/1/25. arXiv: 1002.3619 [astro-ph.HE].

Ganci, V., P. Marziani, M. D'Onofrio, A. del Olmo, E. Bon, N. Bon, and C. A. Negrete (Oct. 2019). "Radio loudness along the quasar main sequence." In: 630, A110, A110. DOI: 10.1051/0004-6361/201936270. arXiv: 1908.07308 [astro-ph.GA].

Goodrich, Robert W. (July 1989). "Spectropolarimetry of "Narrow-Line" Seyfert 1 Galaxies." In: 342, p. 224. DOI: 10.1086/167586.

Graham, Alister W. and Simon P. Driver (Jan. 2005). "A Concise Reference to (Projected) Sérsic $R^{1/n}$ Quantities, Including Concentration, Profile Slopes, Petrosian Indices, and Kron Magnitudes." In: 22.2, pp. 118–127. DOI: 10.1071/AS05001. arXiv: astro-ph/0503176 [astro-ph].

Grupe, Dirk (Apr. 2004). "A Complete Sample of Soft X-Ray-selected AGNs. II. Statistical Analysis." In: 127.4, pp. 1799–1810. DOI: 10.1086/382516. arXiv: astro-ph/0401167 [astro-ph].

Hahn, O., C. Porciani, C. M. Carollo, and A. Dekel (2007). "Properties of dark matter haloes in clusters, filaments, sheets and voids." In: *Monthly Notices of the Royal Astronomical Society* 375.2, 489–499. ISSN: 1365-2966. DOI: 10.1111/j.1365-2966.2006.11318.x. URL: http://dx.doi.org/10.1111/j.1365-2966.2006.11318.x.

Hardcastle, M. J., D. A. Evans, and J. H. Croston (Aug. 2006). "The X-ray nuclei of intermediate-redshift radio sources." In: 370.4, pp. 1893–1904. DOI: 10.1111/j.1365-2966.2006.10615.x. arXiv: astro-ph/0603090 [astro-ph].

Heckman, Timothy M. and Philip N. Best (Aug. 2014). "The Coevolution of Galaxies and Supermassive Black Holes: Insights from Surveys of the Contemporary Universe." In: *araa* 52, pp. 589–660. DOI: 10.1146/annurev-astro-081913-035722. arXiv: 1403.4620 [astro-ph.GA].

Hopkins, Philip F., Kevin Bundy, Darren Croton, Lars Hernquist, Dusan Keres, Sadegh Khochfar, Kyle Stewart, Andrew Wetzel, and Joshua D. Younger (May 2010). "Mergers and Bulge Formation in ΛCDM: Which Mergers Matter?" In: 715.1, pp. 202–229. DOI: 10.1088/0004-637X/715/1/202. arXiv: 0906.5357 [astro-ph.CO].

Hoyle, F. and W. A. Fowler (Jan. 1963). "On the nature of strong radio sources." In: 125, p. 169. DOI: 10.1093/mnras/125.2.169.

Hu, Chen, Jian-Min Wang, Luis C. Ho, Yan-Mei Chen, Wei-Hao Bian, and Sui-Jian Xue (Aug. 2008). "Hβ Profiles in Quasars: Evidence for an Intermediate-Line Region." In: 683.2, p. L115. DOI: 10.1086/591848. arXiv: 0807.2060 [astro-ph].

Hubble, Edwin and Milton L. Humason (July 1931). "The Velocity-Distance Relation among Extra-Galactic Nebulae." In: 74, p. 43. DOI: 10.1086/143323.

Hutchings, J. B., T. Janson, and S. G. Neff (July 1989). "What Is the Difference between Radio-loud and Radio-quiet Objects?" In: 342, p. 660. DOI: 10.1086/167626.

Ideue, Y. et al. (Aug. 2009). "Environmental Effects on the Star Formation Activity in Galaxies at z sime 1.2 in the COSMOS Field." In: 700.2, pp. 971–976. DOI: 10.1088/0004-637X/700/2/971. arXiv: 0905.3982 [astro-ph.CO].

Ishibashi, W. and A. C. Fabian (Dec. 2012). "Active galactic nucleus feedback and triggering of star formation in galaxies." In: 427.4, pp. 2998–3005. DOI: 10.1111/j.1365-2966.2012.22074.x. arXiv: 1209.1480 [astro-ph.GA].

Janssen, R. M. J., H. J. A. Röttgering, P. N. Best, and J. Brinchmann (May 2012). "The triggering probability of radio-loud AGN. A comparison of high and low excitation radio galaxies in hosts of different colors." In: 541, A62, A62. DOI: 10.1051/0004-6361/201219052. arXiv: 1206.0578 [astro-ph.CO].

Järvelä, E. (2018). *Narrow-line Seyfert 1 galaxies.*

Järvelä, E., A. Lähteenmäki, and J. León-Tavares (Jan. 2015). "Statistical multifrequency study of narrow-line Seyfert 1 galaxies." In: 573, A76, A76. DOI: 10.1051/0004-6361/201424694. arXiv: 1410.2743 [astro-ph.GA].

Järvelä, E., A. Lähteenmäki, H. Lietzen, A. Poudel, P. Heinämäki, and M. Einasto (Sept. 2017). "Large-scale environments of narrow-line Seyfert 1 galaxies." In: 606, A9, A9. DOI: 10.1051/0004-6361/201731318. arXiv: 1707.01411 [astro-ph.GA].

Keenan, R. C., S. Foucaud, R. De Propris, B. C. Hsieh, L. Lin, R. C. Y. Chou, S. Huang, J. H. Lin, and K. H. Chang (Nov. 2014). "Evolution of the Major Merger Galaxy Pair Fraction at z < 1." In: 795.2, 157, p. 157. DOI: 10.1088/0004-637X/795/2/157. arXiv: 1408.3468 [astro-ph.GA].

Kellermann, K. I., R. Sramek, M. Schmidt, D. B. Shaffer, and R. Green (Oct. 1989). "VLA Observations of Objects in the Palomar Bright Quasar Survey." In: 98, p. 1195. DOI: 10.1086/115207.

Khan, Fazeel Mahmood, Andreas Just, and David Merritt (May 2011). "Efficient Merger of Binary Supermassive Black Holes in Merging Galaxies." In: 732.2, 89, p. 89. DOI: 10.1088/0004-637X/732/2/89. arXiv: 1103.0272 [astro-ph.CO].

Kishimoto, M., S. F. Hönig, R. Antonucci, F. Millour, K. R. W. Tristram, and G. Weigelt (Dec. 2011). "Mapping the radial structure of AGN tori." In: 536, A78, A78. DOI: 10.1051/0004-6361/201117367. arXiv: 1110.4290 [astro-ph.CO].

Kitaura, F.-S., A. Balaguera-Antolínez, F. Sinigaglia, and M. Pellejero-Ibáñez (2020). "The cosmic web connection to the dark matter halo distribution through gravity." In: arXiv: 2005.11598 [astro-ph.CO].

Komossa, Stefanie, Wolfgang Voges, Dawei Xu, Smita Mathur, Hans-Martin Adorf, Gerard Lemson, Wolfgang J. Duschl, and Dirk Grupe (Aug. 2006). "Radio-loud Narrow-Line Type 1 Quasars." In: 132.2, pp. 531–545. DOI: 10.1086/505043. arXiv: astro-ph/0603680 [astro-ph].

Koss, Michael, Richard Mushotzky, Sylvain Veilleux, and Lisa Winter (June 2010). "Merging and Clustering of the Swift BAT AGN Sample." In: 716.2, pp. L125–L130. DOI: 10.1088/2041-8205/716/2/L125. arXiv: 1006.0228 [astro-ph.CO].

Kron, R. G. (June 1980). "Photometry of a complete sample of faint galaxies." In: 43, pp. 305–325. DOI: 10.1086/190669.

Krongold, Y., D. Dultzin-Hacyan, and P. Marziani (Feb. 2001). "Host Galaxies and Circumgalactic Environment of "Narrow Line" Seyfert 1 Nuclei." In: 121.2, pp. 702–709. DOI: 10.1086/318768.

Kuutma, Teet, Antti Tamm, and Elmo Tempel (Apr. 2017). "From voids to filaments: environmental transformations of galaxies in the SDSS." In: 600, L6, p. L6. DOI: 10.1051/0004-6361/201730526. arXiv: 1703.04338 [astro-ph.GA].

LaMassa, Stephanie M., Sabrina Cales, Edward C. Moran, Adam D. Myers, Gordon T. Richards, Michael Eracleous, Timothy M. Heckman, Luigi Gallo, and C. Megan Urry (Feb. 2015). "The Discovery of the First "Changing Look" Quasar: New Insights Into the Physics and Phenomenology of

Active Galactic Nucleus." In: 800.2, 144, p. 144. DOI: 10.1088/0004-637X/800/2/144. arXiv: 1412.2136 [astro-ph.GA].

LaMassa, Stephanie M., T. M. Heckman, A. Ptak, and C. Megan Urry (Mar. 2013). "On the Star Formation-AGN Connection at z <∼0.3." In: 765.2, L33, p. L33. DOI: 10.1088/2041-8205/765/2/L33. arXiv: 1302.2631 [astro-ph.CO].

Lauer, Tod R., Scott Tremaine, Douglas Richstone, and S. M. Faber (Nov. 2007). "Selection Bias in Observing the Cosmological Evolution of the $M_{\acute{L}}$-σ and $M_{\acute{L}}$-L Relationships." In: 670.1, pp. 249–260. DOI: 10.1086/522083. arXiv: 0705.4103 [astro-ph].

Laurikainen, E., H. Salo, P. Teerikorpi, and G. Petrov (Dec. 1994). "Environments of Seyfert galaxies. I. Construction of the sample and selection effects." In: 108, pp. 491–508.

Lietzen, H., E. Tempel, P. Heinämäki, P. Nurmi, M. Einasto, and E. Saar (Sept. 2012). "Environments of galaxies in groups within the supercluster-void network." In: 545, A104, A104. DOI: 10.1051/0004-6361/201219353. arXiv: 1207.7070 [astro-ph.CO].

Lotz, Jennifer M., Patrik Jonsson, T. J. Cox, Darren Croton, Joel R. Primack, Rachel S. Somerville, and Kyle Stewart (Dec. 2011). "The Major and Minor Galaxy Merger Rates at z < 1.5." In: 742.2, 103, p. 103. DOI: 10.1088/0004-637X/742/2/103. arXiv: 1108.2508 [astro-ph.CO].

Lynden-Bell, D. (Aug. 1969). "Galactic Nuclei as Collapsed Old Quasars." In: 223.5207, pp. 690–694. DOI: 10.1038/223690a0.

Man, Allison W. S., Sune Toft, Andrew W. Zirm, Stijn Wuyts, and Arjen van der Wel (Jan. 2012). "The Pair Fraction of Massive Galaxies at 0 <= z <= 3." In: 744.2, 85, p. 85. DOI: 10.1088/0004-637X/744/2/85. arXiv: 1109.2895 [astro-ph.CO].

Mármol-Queraltó, E., I. Trujillo, P. G. Pérez-González, J. Varela, and G. Barro (May 2012). "Satellites around massive galaxies since z∼ 2." In: 422.3, pp. 2187–2194. DOI: 10.1111/j.1365-2966.2012.20765.x. arXiv: 1201.2414 [astro-ph.CO].

Marziani, P. and J. W. Sulentic (Aug. 2014). "Highly accreting quasars: sample definition and possible cosmological implications." In: 442.2, pp. 1211–1229. DOI: 10.1093/mnras/stu951. arXiv: 1405.2727 [astro-ph.GA].

Marziani, P., J. W. Sulentic, T. Zwitter, D. Dultzin-Hacyan, and M. Calvani (Sept. 2001). "Searching for the Physical Drivers of the Eigenvector 1 Correlation Space." In: 558.2, pp. 553–560. DOI: 10.1086/322286. arXiv: astro-ph/0105343 [astro-ph].

Marziani, Paola, Deborah Dultzin-Hacyan, and Jack W. Sulentic (2006). "Accretion onto Supermassive Black Holes in Quasars: Learning from Optical/UV Observations." In: *New Developments in Black Hole Research*. Ed. by Paul V. Kreitler, p. 123.

Marziani, Paola, Deborah Dultzin, Jack W. Sulentic, Ascensión Del Olmo, C. A. Negrete, Mary L. Martínez-Aldama, Mauro D'Onofrio, Edi Bon, Natasa Bon, and Giovanna M. Stirpe (Mar. 2018). "A main sequence for

quasars." In: *Frontiers in Astronomy and Space Sciences* 5, 6, p. 6. DOI: 10.3389/fspas.2018.00006. arXiv: 1802.05575 [astro-ph.GA].

Marziani, Paola, Jack W. Sulentic, Ilse Plauchu-Frayn, and Ascensión del Olmo (Feb. 2013). "Low-ionization Outflows in High Eddington Ratio Quasars." In: 764.2, 150, p. 150. DOI: 10.1088/0004-637X/764/2/150. arXiv: 1301.0520 [astro-ph.CO].

Marziani, Paola et al. (Jan. 2022). "The main sequence of quasars: The taming of the extremes." In: *Astronomische Nachrichten* 343.1-2, e210082, e210082. DOI: 10.1002/asna.20210082. arXiv: 2111.04140 [astro-ph.GA].

Miller, L., J. A. Peacock, and A. R. G. Mead (May 1990). "The bimodal radio luminosity function of quasars." In: 244, pp. 207–213.

Mineshige, Shin, Toshihiro Kawaguchi, Mitsuru Takeuchi, and Kiyoshi Hayashida (June 2000). "Slim-Disk Model for Soft X-Ray Excess and Variability of Narrow-Line Seyfert 1 Galaxies." In: 52, pp. 499–508. DOI: 10.1093/pasj/52.3.499. arXiv: astro-ph/0003017 [astro-ph].

Morgan, Christopher W., C. S. Kochanek, Nicholas D. Morgan, and Emilio E. Falco (Apr. 2010). "The Quasar Accretion Disk Size-Black Hole Mass Relation." In: 712.2, pp. 1129–1136. DOI: 10.1088/0004-637X/712/2/1129. arXiv: 1002.4160 [astro-ph.CO].

Morgan, Jeffrey S. and Nicholas Kaiser (July 2008). "Alignment of the Pan-STARRS PS1 prototype telescope optics." In: *Ground-based and Airborne Telescopes II*. Ed. by Larry M. Stepp and Roberto Gilmozzi. Vol. 7012. Society of Photo-Optical Instrumentation Engineers (SPIE) Conference Series, 70121K, 70121K. DOI: 10.1117/12.788426.

Murray, Norman, Eliot Quataert, and Todd A. Thompson (Jan. 2005). "On the Maximum Luminosity of Galaxies and Their Central Black Holes: Feedback from Momentum-driven Winds." In: 618.2, pp. 569–585. DOI: 10.1086/426067. arXiv: astro-ph/0406070 [astro-ph].

Narayan, Ramesh and Insu Yi (June 1994). "Advection-dominated Accretion: A Self-similar Solution." In: 428, p. L13. DOI: 10.1086/187381. arXiv: astro-ph/9403052 [astro-ph].

Navarro, Julio F., Carlos S. Frenk, and Simon D. M. White (May 1996). "The Structure of Cold Dark Matter Halos." In: 462, p. 563. DOI: 10.1086/177173. arXiv: astro-ph/9508025 [astro-ph].

Osterbrock, D. E. and R. W. Pogge (Oct. 1985). "The spectra of narrow-line Seyfert 1 galaxies." In: 297, pp. 166–176. DOI: 10.1086/163513.

Padovani, Paolo (Aug. 2017). "On the two main classes of active galactic nuclei." In: *Nature Astronomy* 1, 0194, p. 0194. DOI: 10.1038/s41550-017-0194. arXiv: 1707.08069 [astro-ph.GA].

Panda, Swayamtrupta, Paola Marziani, and Bożena Czerny (Sept. 2019). "The Quasar Main Sequence Explained by the Combination of Eddington Ratio, Metallicity, and Orientation." In: 882.2, 79, p. 79. DOI: 10.3847/1538-4357/ab3292. arXiv: 1905.01729 [astro-ph.HE].

Pandey, Biswajit and Suman Sarkar (May 2017). "How much a galaxy knows about its large-scale environment?: An information theoretic perspective."

In: 467.1, pp. L6–L10. DOI: 10.1093/mnrasl/slw250. arXiv: 1611.00283 [astro-ph.CO].

Park, Changbom and Yun-Young Choi (Feb. 2009). "Combined Effects of Galaxy Interactions and Large-Scale Environment on Galaxy Properties." In: 691.2, pp. 1828–1845. DOI: 10.1088/0004-637X/691/2/1828. arXiv: 0809.2156 [astro-ph].

Patil, V.V. and H.V. Kulkarni (2012). "Comparison of Confidence Intervals for the Poisson Mean: Some New Aspects." In: *REVSTAT-Statistical Journal* 10.2, 211–22. URL: https://revstat.ine.pt/index.php/REVSTAT/article/view/117.

Penston, M. V., M. J. Penston, R. A. Selmes, E. E. Becklin, and G. Neugebauer (Nov. 1974). "Broadband optical and infrared observations of Seyfert galaxies." In: 169, pp. 357–393. DOI: 10.1093/mnras/169.2.357.

Penston, M. V. and E. Perez (Nov. 1984). "An evolutionary link between Seyfert I and II galaxies." In: 211, 33P–39. DOI: 10.1093/mnras/211.1.33P.

Peterson, B. M. (Jan. 2011). "Masses of Black Holes in Active Galactic Nuclei: Implications for Narrow-Line Seyfert 1 Galaxies." In: *Narrow-Line Seyfert 1 Galaxies and their Place in the Universe*. Ed. by L. Foschini, M. Colpi, L. Gallo, D. Grupe, S. Komossa, K. Leighly, and S. Mathur, 32, p. 32.

Peterson, B. M. and K. Horne (Mar. 2004). "Echo mapping of active galactic nuclei." In: *Astronomische Nachrichten* 325.3, pp. 248–251. DOI: 10.1002/asna.200310207. arXiv: astro-ph/0407538 [astro-ph].

Poudel, A., P. Heinämäki, E. Tempel, M. Einasto, H. Lietzen, and P. Nurmi (Jan. 2017). "The effect of cosmic web filaments on the properties of groups and their central galaxies." In: 597, A86, A86. DOI: 10.1051/0004-6361/201629639. arXiv: 1611.01072 [astro-ph.GA].

Pović, M. et al. (May 2012). "AGN-host galaxy connection: morphology and colours of X-ray selected AGN at z $\leqslant$ 2." In: 541, A118, A118. DOI: 10.1051/0004-6361/201117314. arXiv: 1202.1662 [astro-ph.CO].

Rafanelli, P. and P. Marziani (Jan. 1992). "Seyfert Galaxies with close companions. A method of identification." In: *Morphological and Physical Classification of Galaxies*. Ed. by G. Longo, M. Capaccioli, and G. Busarello. Vol. 178. Astrophysics and Space Science Library, p. 451. DOI: 10.1007/978-94-011-2522-2_65.

Rafanelli, P., M. Violato, and A. Baruffolo (Apr. 1995). "On the Excess of Physical Companions among Seyfert Galaxies." In: 109, p. 1546. DOI: 10.1086/117384.

Reber, Grote (Nov. 1944). "Cosmic Static." In: 100, p. 279. DOI: 10.1086/144668.

Richards, Gordon T. et al. (June 2006). "The Sloan Digital Sky Survey Quasar Survey: Quasar Luminosity Function from Data Release 3." In: 131.6, pp. 2766–2787. DOI: 10.1086/503559. arXiv: astro-ph/0601434 [astro-ph].

Richstone, D. O. and M. Schmidt (Jan. 1980). "The spectral properties of a large sample of quasars." In: 235, pp. 361–376. DOI: 10.1086/157640.

Robotham, A. S. G. et al. (Nov. 2014). "Galaxy And Mass Assembly (GAMA): galaxy close pairs, mergers and the future fate of stellar mass." In: 444.4, pp. 3986–4008. DOI: 10.1093/mnras/stu1604. arXiv: 1408.1476 [astro-ph.GA].

Sakamoto, K., S. K. Okumura, S. Ishizuki, and N. Z. Scoville (Nov. 1999). "Bar-driven Transport of Molecular Gas to Galactic Centers and Its Consequences." In: 525.2, pp. 691–701. DOI: 10.1086/307910. arXiv: astro-ph/9906454 [astro-ph].

Salpeter, E. E. (Aug. 1964). "Accretion of Interstellar Matter by Massive Objects." In: 140, pp. 796–800. DOI: 10.1086/147973.

Sandage, Allan (May 1965). "The Existence of a Major New Constituent of the Universe: the Quasistellar Galaxies." In: 141, p. 1560. DOI: 10.1086/148245.

Schechter, P. (Jan. 1976). "An analytic expression for the luminosity function for galaxies." In: 203, pp. 297–306. DOI: 10.1086/154079.

Schmidt, Maarten (Feb. 1968). "Space Distribution and Luminosity Functions of Quasi-Stellar Radio Sources." In: 151, p. 393. DOI: 10.1086/149446.

Schneider, Peter (2006). *Extragalactic Astronomy and Cosmology*.

Schulze, A. and L. Wisotzki (Nov. 2011). "Selection effects in the black hole-bulge relation and its evolution." In: 535, A87, A87. DOI: 10.1051/0004-6361/201117564. arXiv: 1109.2787 [astro-ph.CO].

Sérsic, J. L. (Feb. 1963). "Influence of the atmospheric and instrumental dispersion on the brightness distribution in a galaxy." In: *Boletin de la Asociacion Argentina de Astronomia La Plata Argentina* 6, pp. 41–43.

Seyfert, Carl K. (Jan. 1943). "Nuclear Emission in Spiral Nebulae." In: 97, p. 28. DOI: 10.1086/144488.

Shakura, N. I. and R. A. Sunyaev (June 1976). "A theory of the instability of disk accretion on to black holes and the variability of binary X-ray sources, galactic nuclei and quasars." In: 175, pp. 613–632. DOI: 10.1093/mnras/175.3.613.

Shen, Yue and Luis C. Ho (Sept. 2014). "The diversity of quasars unified by accretion and orientation." In: 513.7517, pp. 210–213. DOI: 10.1038/nature13712. arXiv: 1409.2887 [astro-ph.GA].

Silk, Joseph and Martin J. Rees (Mar. 1998). "Quasars and galaxy formation." In: 331, pp. L1–L4. arXiv: astro-ph/9801013 [astro-ph].

Slipher, V. M. (Jan. 1913). "The radial velocity of the Andromeda Nebula." In: *Lowell Observatory Bulletin* 1, pp. 56–57.

Steinhauser, Dominik, Sabine Schindler, and Volker Springel (June 2016). "Simulations of ram-pressure stripping in galaxy-cluster interactions." In: 591, A51, A51. DOI: 10.1051/0004-6361/201527705. arXiv: 1604.05193 [astro-ph.GA].

Storchi-Bergmann, T. (Apr. 2008). "Observational Overview of the Feeding of Active Galactic Nuclei." In: *Revista Mexicana de Astronomia y Astrofisica Conference Series*. Vol. 32. Revista Mexicana de Astronomia y Astrofisica Conference Series, pp. 139–146. arXiv: 0712.3747 [astro-ph].

Strittmatter, P. A., P. Hill, I. I. K. Pauliny-Toth, H. Steppe, and A. Witzel (Aug. 1980). "Radio observations of optically selected quasars." In: 88.3, pp. L12–L15.

Sulentic, J. W., M. Calvani, and P. Marziani (June 2001). "Eigenvector 1: an H-R diagram for AGN?" In: *The Messenger* 104, pp. 25–28.

Sulentic, J. W., P. Marziani, and D. Dultzin-Hacyan (Jan. 2000). "Phenomenology of Broad Emission Lines in Active Galactic Nuclei." In: 38, pp. 521–571. DOI: 10.1146/annurev.astro.38.1.521.

Sulentic, J. W., P. Marziani, R. Zamanov, R. Bachev, M. Calvani, and D. Dultzin-Hacyan (Feb. 2002). "Average Quasar Spectra in the Context of Eigenvector 1." In: 566.2, pp. L71–L75. DOI: 10.1086/339594. arXiv: astro-ph/0201362 [astro-ph].

Sulentic, Jack and Paola Marziani (Oct. 2015). "Quasars in the 4D Eigenvector 1 Context: a stroll down memory lane." In: *Frontiers in Astronomy and Space Sciences* 2, 6, p. 6. DOI: 10.3389/fspas.2015.00006. arXiv: 1506.01276 [astro-ph.GA].

Szuszkiewicz, Ewa, Matthew A. Malkan, and Marek A. Abramowicz (Feb. 1996). "The Observational Appearance of Slim Accretion Disks." In: 458, p. 474. DOI: 10.1086/176830. arXiv: astro-ph/9509037 [astro-ph].

Taniguchi, Yoshiaki (Oct. 1999). "The Minor-Merger-driven Nuclear Activity in Seyfert Galaxies: A Step toward the Simple Unified Formation Mechanism of Active Galactic Nuclei in the Local Universe." In: 524.1, pp. 65–70. DOI: 10.1086/307814. arXiv: astro-ph/9905353 [astro-ph].

Tarrío, P. and S. Zarattini (Oct. 2020). "Photometric redshifts for the Pan-STARRS1 survey." In: 642, A102, A102. DOI: 10.1051/0004-6361/202038415. arXiv: 2005.06489 [astro-ph.GA].

Tonry, J. L. et al. (May 2012). "The Pan-STARRS1 Photometric System." In: 750.2, 99, p. 99. DOI: 10.1088/0004-637X/750/2/99. arXiv: 1203.0297 [astro-ph.IM].

Tonry, J., Barry E. Burke, and Paul L. Schechter (Oct. 1997). "The Orthogonal Transfer CCD." In: 109, pp. 1154–1164. DOI: 10.1086/133989.

Trakhtenbrot, Benny, Hagai Netzer, Paulina Lira, and Ohad Shemmer (Mar. 2011). "Black Hole Mass and Growth Rate at z $\sim=$ 4.8: A Short Episode of Fast Growth Followed by Short Duty Cycle Activity." In: 730.1, 7, p. 7. DOI: 10.1088/0004-637X/730/1/7. arXiv: 1012.1871 [astro-ph.CO].

Urrutia, Tanya, Mark Lacy, and Robert H. Becker (Feb. 2008). "Evidence for Quasar Activity Triggered by Galaxy Mergers in HST Observations of Dust-reddened Quasars." In: 674.1, pp. 80–96. DOI: 10.1086/523959. arXiv: 0709.2805 [astro-ph].

Urry, C. Megan and Paolo Padovani (Sept. 1995). "Unified Schemes for Radio-Loud Active Galactic Nuclei." In: 107, p. 803. DOI: 10.1086/133630. arXiv: astro-ph/9506063 [astro-ph].

Weedman, Daniel W. (July 1973). "A Photometric Study of Markarian Galaxies." In: 183, pp. 29–40. DOI: 10.1086/152205.

White, S. D. M. and M. J. Rees (May 1978). "Core condensation in heavy halos: a two-stage theory for galaxy formation and clustering." In: 183, pp. 341–358. DOI: 10.1093/mnras/183.3.341.

Wilson, A. S. and E. J. M. Colbert (May 1995). "The Origin of Powerful Radio Sources." In: *American Astronomical Society Meeting Abstracts #186*. Vol. 186. American Astronomical Society Meeting Abstracts, 15.02, p. 15.02.

Woltjer, L. (July 1959). "Emission Nuclei in Galaxies." In: 130, p. 38. DOI: 10.1086/146694.

Xu, Dawei, S. Komossa, Hongyan Zhou, Honglin Lu, Cheng Li, Dirk Grupe, Jing Wang, and Weimin Yuan (Apr. 2012). "Correlation Analysis of a Large Sample of Narrow-line Seyfert 1 Galaxies: Linking Central Engine and Host Properties." In: 143.4, 83, p. 83. DOI: 10.1088/0004-6256/143/4/83. arXiv: 1201.2810 [astro-ph.CO].

Yang, Qian et al. (Aug. 2018). "Discovery of 21 New Changing-look AGNs in the Northern Sky." In: 862.2, 109, p. 109. DOI: 10.3847/1538-4357/aaca3a. arXiv: 1711.08122 [astro-ph.GA].

Zamfir, S., J. W. Sulentic, and P. Marziani (June 2008). "New insights on the QSO radio-loud/radio-quiet dichotomy: SDSS spectra in the context of the 4D eigenvector1 parameter space." In: 387.2, pp. 856–870. DOI: 10.1111/j.1365-2966.2008.13290.x. arXiv: 0804.0788 [astro-ph].

Zamfir, S., J. W. Sulentic, P. Marziani, and D. Dultzin (Apr. 2010). "Detailed characterization of Hβ emission line profile in low-z SDSS quasars." In: 403.4, pp. 1759–1786. DOI: 10.1111/j.1365-2966.2009.16236.x. arXiv: 0912.4306 [astro-ph.CO].

Zel'dovich, Ya. B. and I. D. Novikov (Oct. 1964). "The Radiation of Gravity Waves by Bodies Moving in the Field of a Collapsing Star." In: *Soviet Physics Doklady* 9, p. 246.

Zhou, Hongyan, Tinggui Wang, Weimin Yuan, Honglin Lu, Xiaobo Dong, Junxian Wang, and Youjun Lu (Sept. 2006). "A Comprehensive Study of 2000 Narrow Line Seyfert 1 Galaxies from the Sloan Digital Sky Survey. I. The Sample." In: 166.1, pp. 128–153. DOI: 10.1086/504869. arXiv: astro-ph/0603759 [astro-ph].

Zhu, Ling, Shuang Nan Zhang, and Sumin Tang (Aug. 2009). "Evidence for an Intermediate Line Region in Active Galactic Nuclei's Inner Torus Region and its Evolution from Narrow to Broad Line Seyfert I Galaxies." In: 700.2, pp. 1173–1189. DOI: 10.1088/0004-637X/700/2/1173. arXiv: 0807.3992 [astro-ph].

de Vaucouleurs, Gerard (Jan. 1948). "Recherches sur les Nebuleuses Extragalactiques." In: *Annales d'Astrophysique* 11, p. 247.

van de Ven, Glenn and Kambiz Fathi (Nov. 2010). "Kinematic Analysis of Nuclear Spirals: Feeding the Black Hole in NGC 1097." In: 723.1, pp. 767–780. DOI: 10.1088/0004-637X/723/1/767. arXiv: 0905.3556 [astro-ph.GA].

APPENDIX

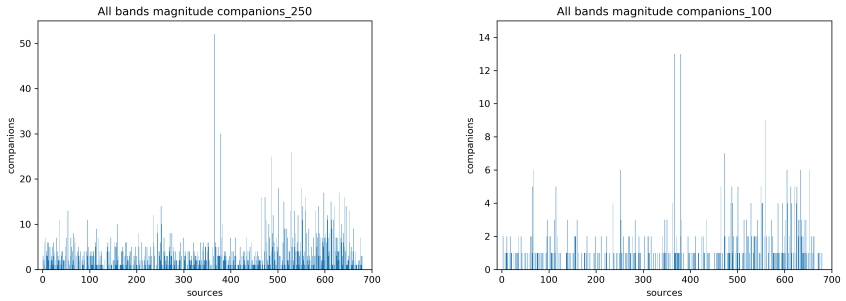

Figure 35: Source order vs n°companions, all filters simultaneously, magnitude selection, A250 and A100.

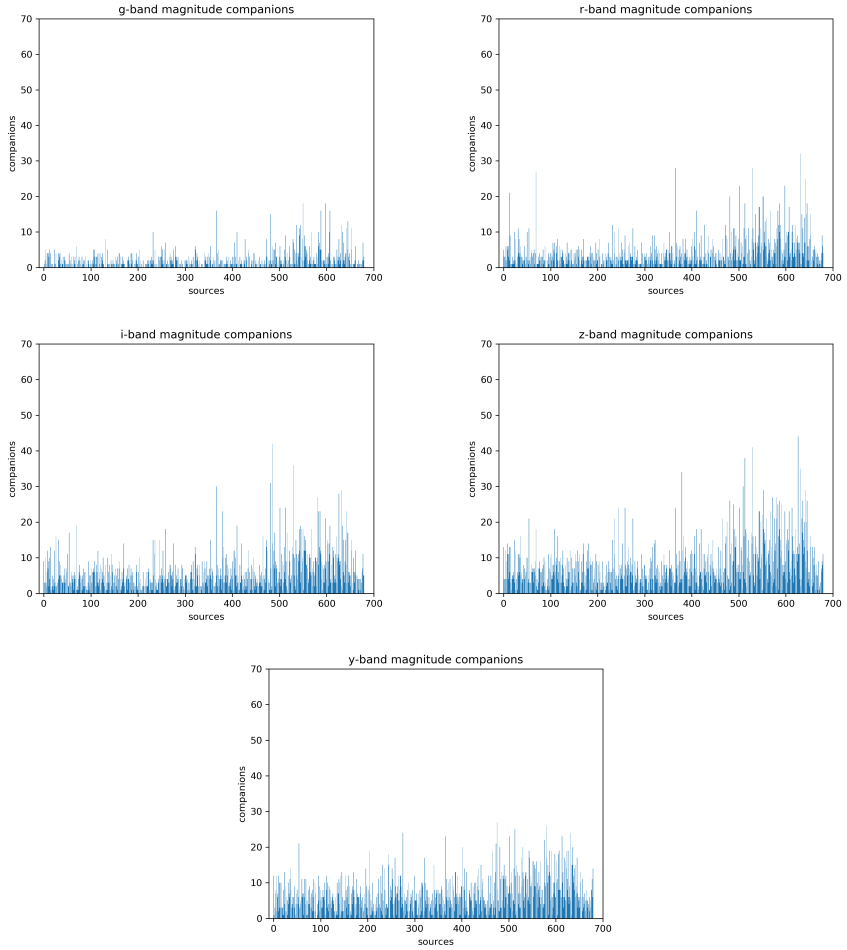

Figure 36: Source order vs n°companions, each filters separately, magnitude selection, A500.

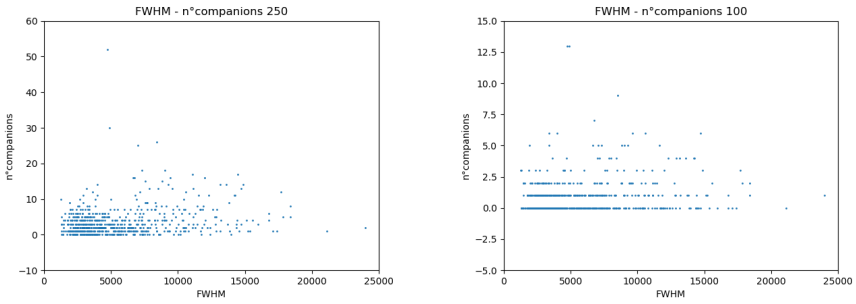

Figure 37: FWHM(H_β) order vs n°companions, magnitude selection, A250 and A100.

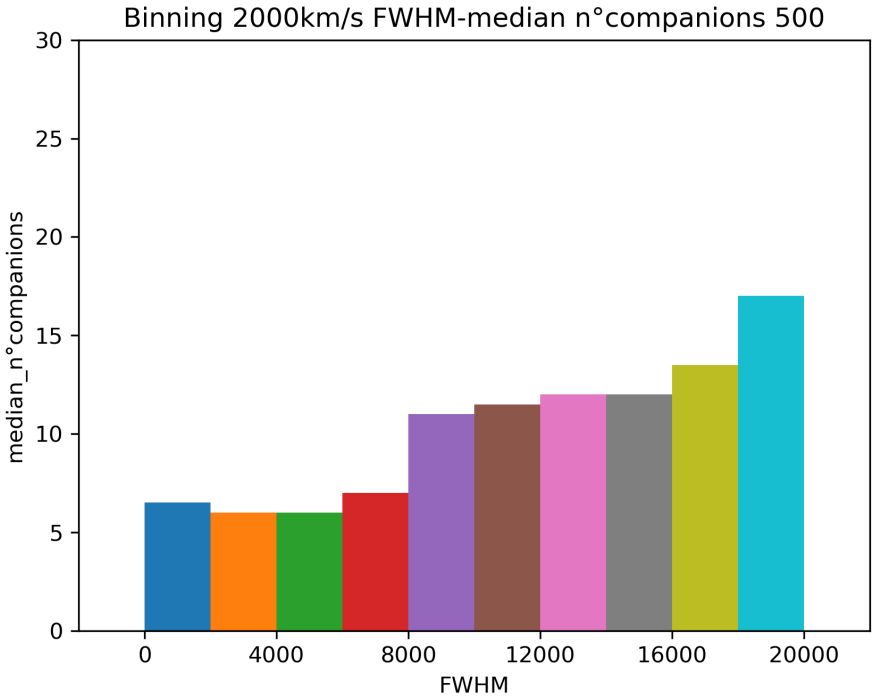

Figure 38: FWHM(H_β) binned vs median n°companions, bins=2000 km s^{-1}, magnitude selection, A500.

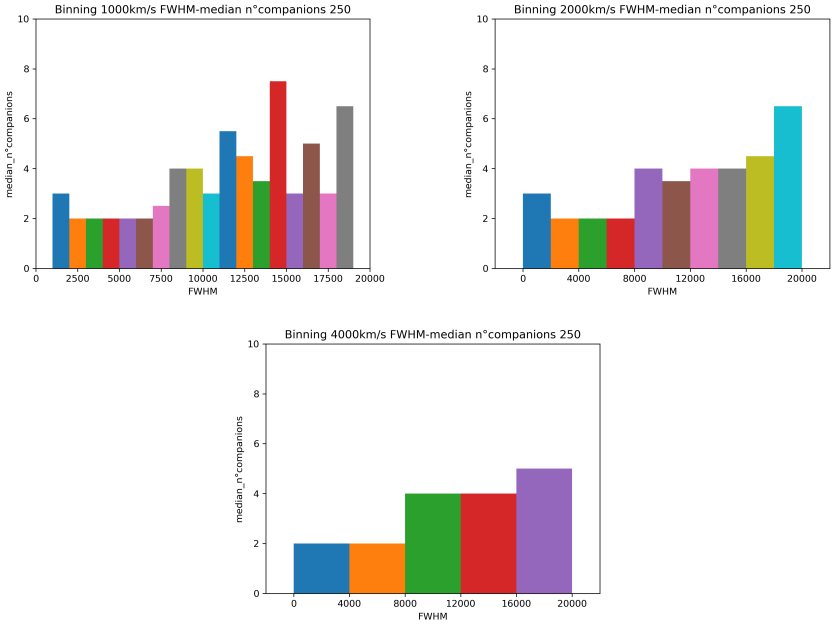

Figure 39: FWHM(H_β) binned vs median n°companions, bins=1000, 2000 and 4000 km s^{-1}, magnitude selection, A250.

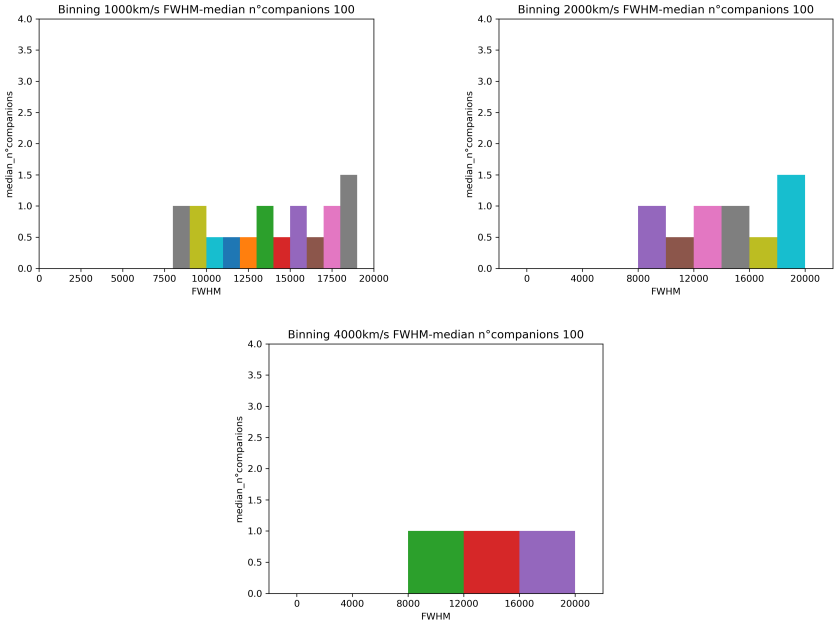

Figure 40: FWHM(H_β) binned vs median n°companions, bins=1000, 2000 and 4000 km s^{-1}, magnitude selection, A100.

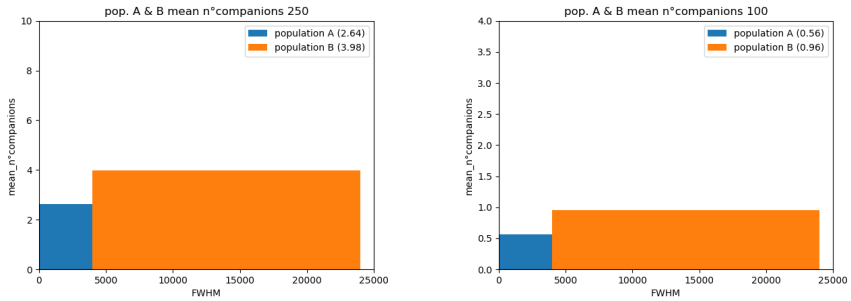

Figure 41: Mean number of companions for population A and B, magnitude selection, A250 and A100.

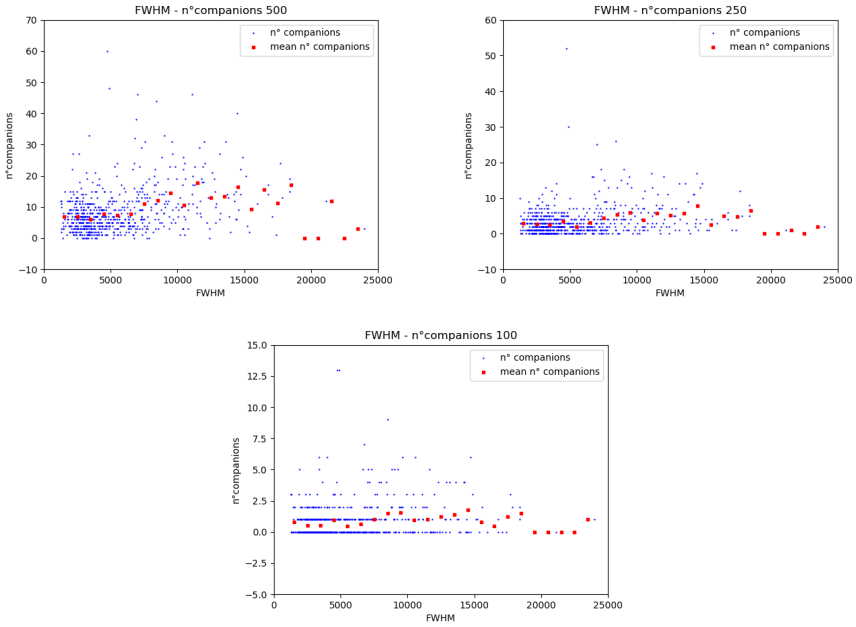

Figure 42: FWHM(H_β) order vs n°companions, superimposed mean n°companions with FWHM(H_β) bins=1000 km s^{-1}, magnitude selection, A500, A250 and A100.

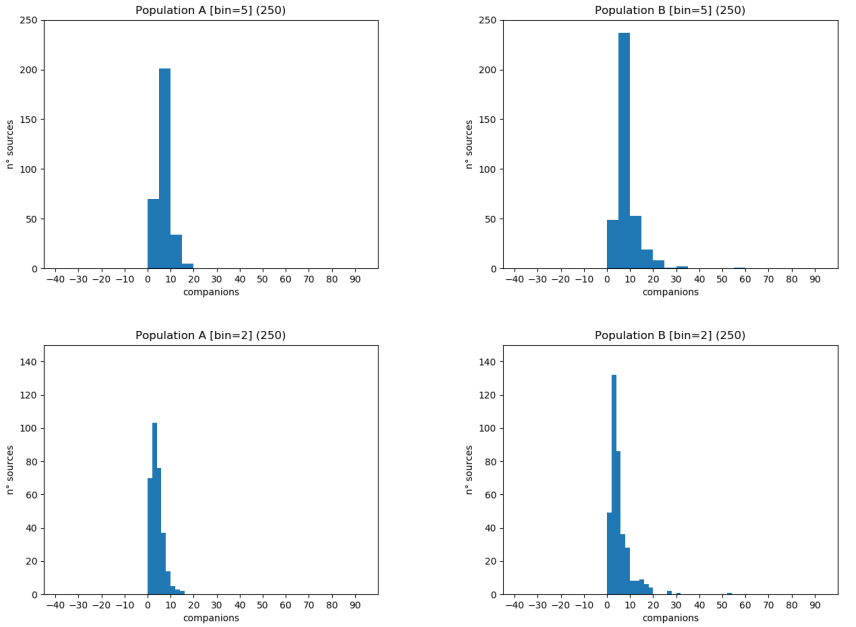

Figure 43: Companions' distribution, *top-left:* pop.A and bin=5, *top-right:* pop.B and bin=5, *bottom-left:* pop.A and bin=2, *bottom-right:* pop.B and bin=2; magnitude selection, A250.

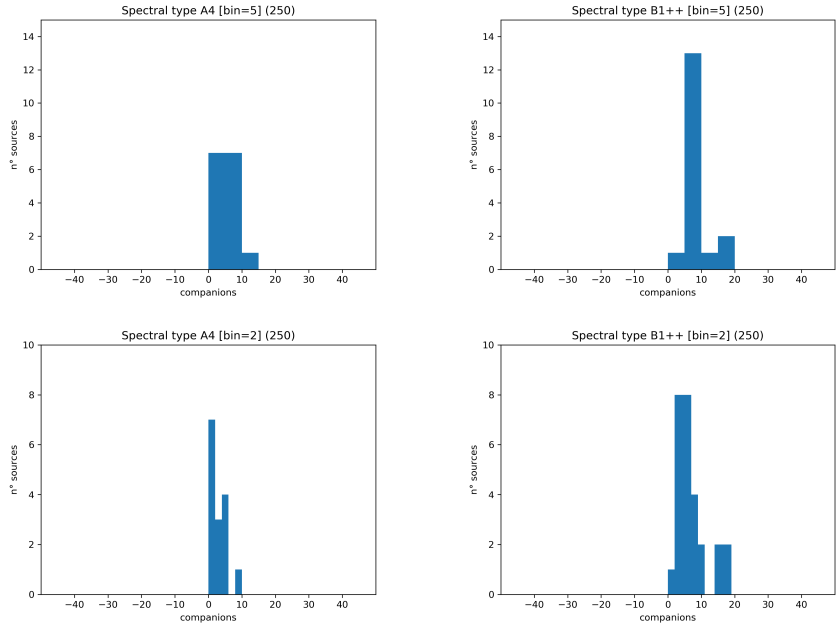

Figure 44: Companions' distribution, *top-left:* A4 sources and bin=5, *top-right:* B1++ sources and bin=5, *bottom-left:* A4 sources and bin=2, *bottom-right:* B1++ sources and bin=2; magnitude selection, A250.

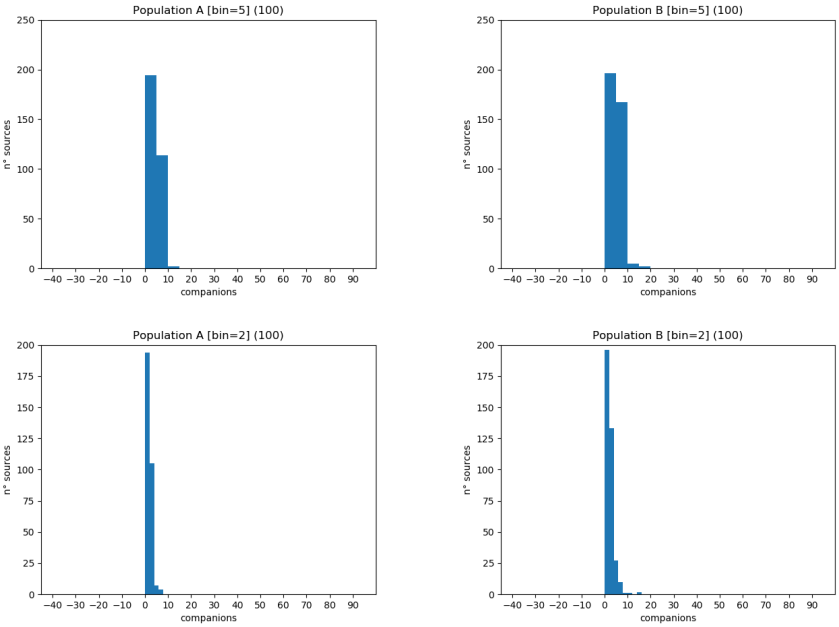

Figure 45: Companions' distribution, *top-left:* pop.A and bin=5, *top-right:* pop.B and bin=5, *bottom-left:* pop.A and bin=2, *bottom-right:* pop.B and bin=2; magnitude selection, A100.

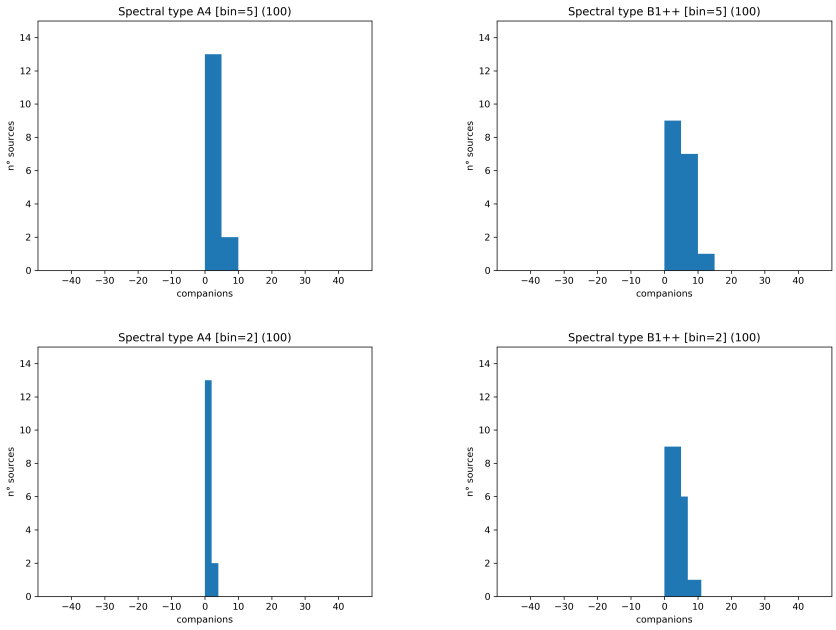

Figure 46: Companions' distribution, *top-left:* A4 sources and bin=5, *top-right:* B1++ sources and bin=5, *bottom-left:* A4 sources and bin=2, *bottom-right:* B1++ sources and bin=2; magnitude selection, A100.

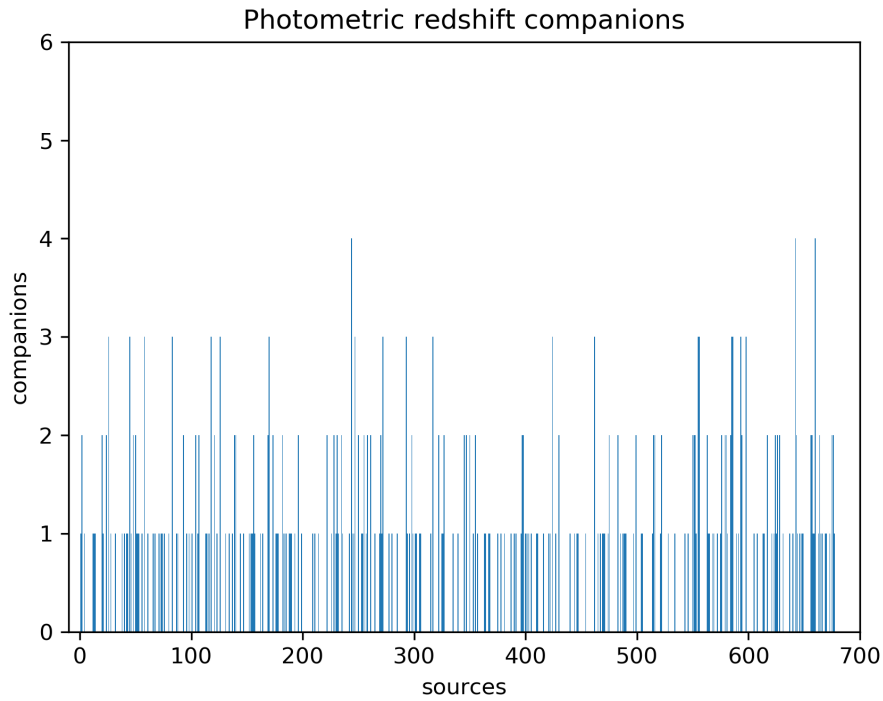

Figure 47: Source order vs n°companions, photometric redshift selection, A500.

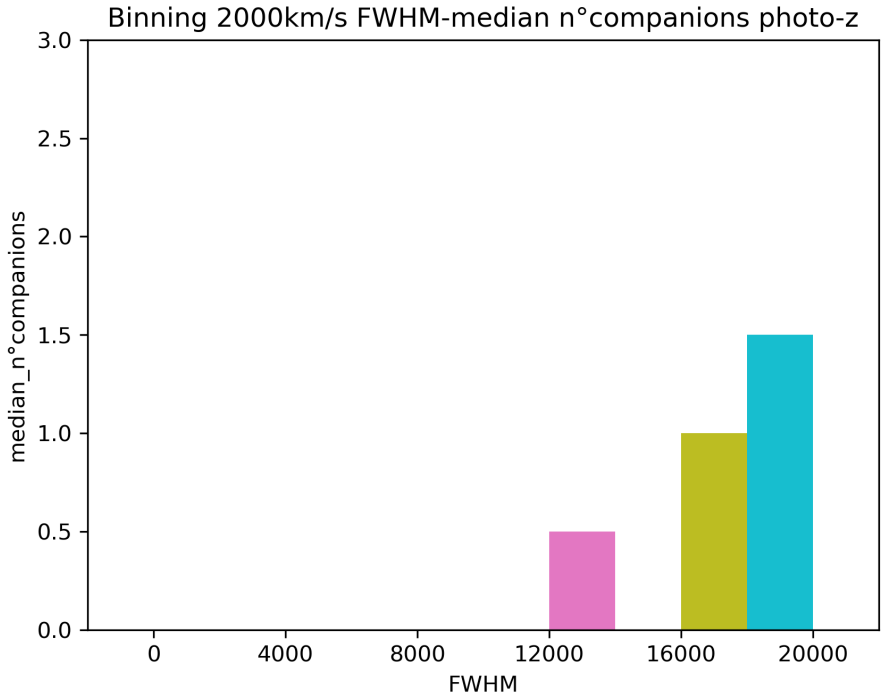

Figure 48: FWHM(H_β) binned vs median n°companions, bins=2000 km s^{-1}, photometric redshift selection, A500.

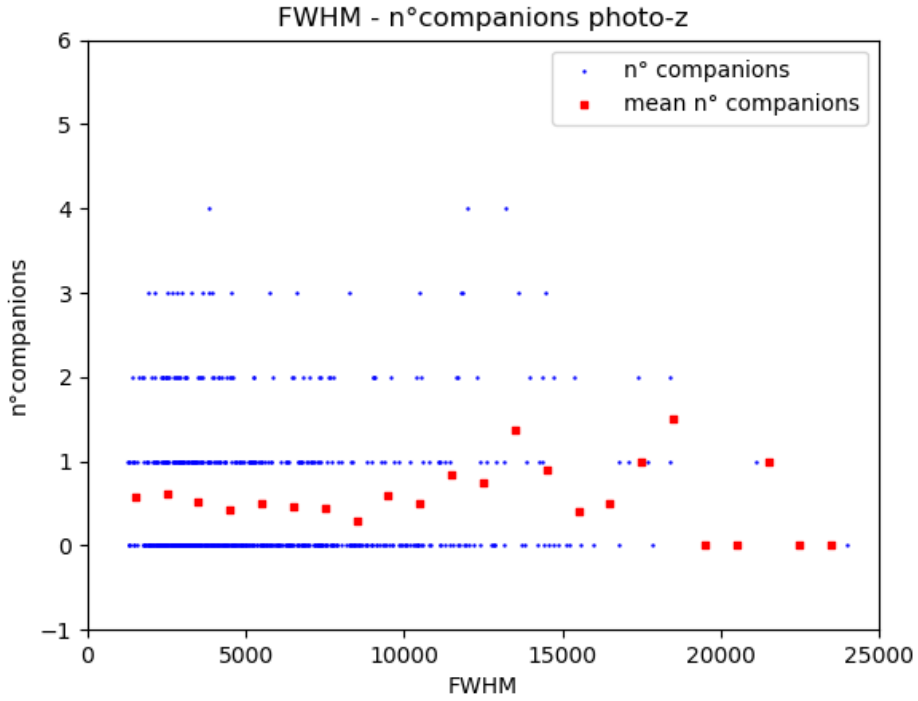

Figure 49: FWHM(H_β) order vs n°companions, superimposed mean n°companions with FWHM(H_β) bins=1000 km s^{-1}, magnitude selection, A500.

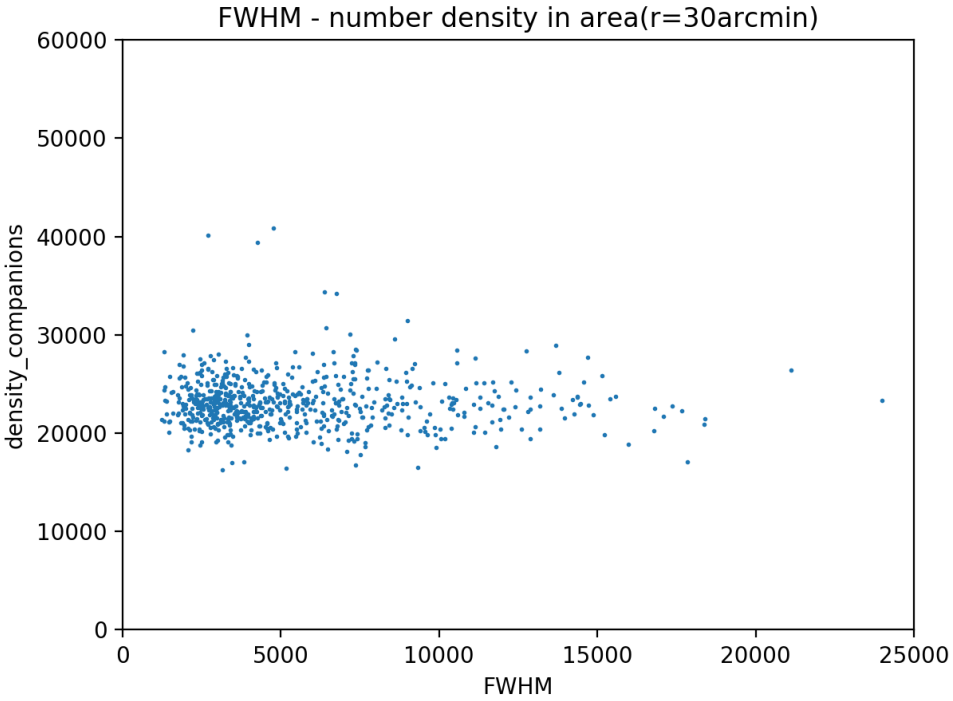

Figure 50: FWHM(H_β) order vs galaxies in area(r=30arcmin), density approach.

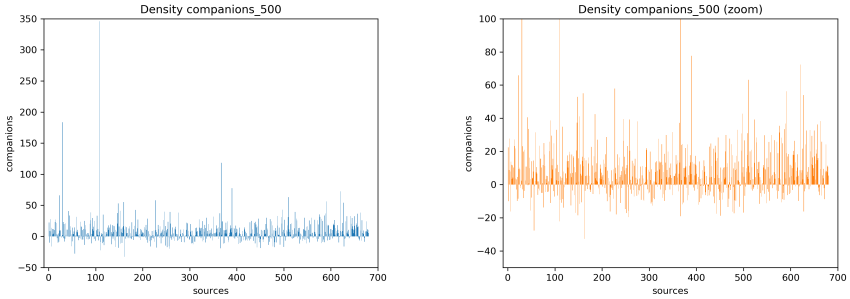

Figure 51: Source order vs n°companions, density approach, A500.

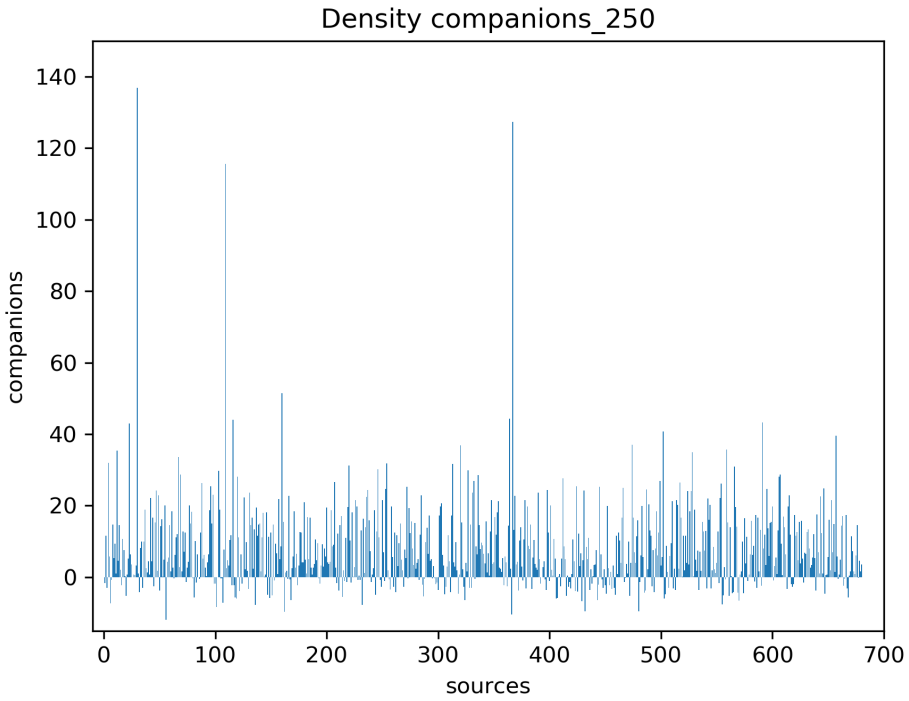

Figure 52: Source order vs n°companions, density approach, A250.

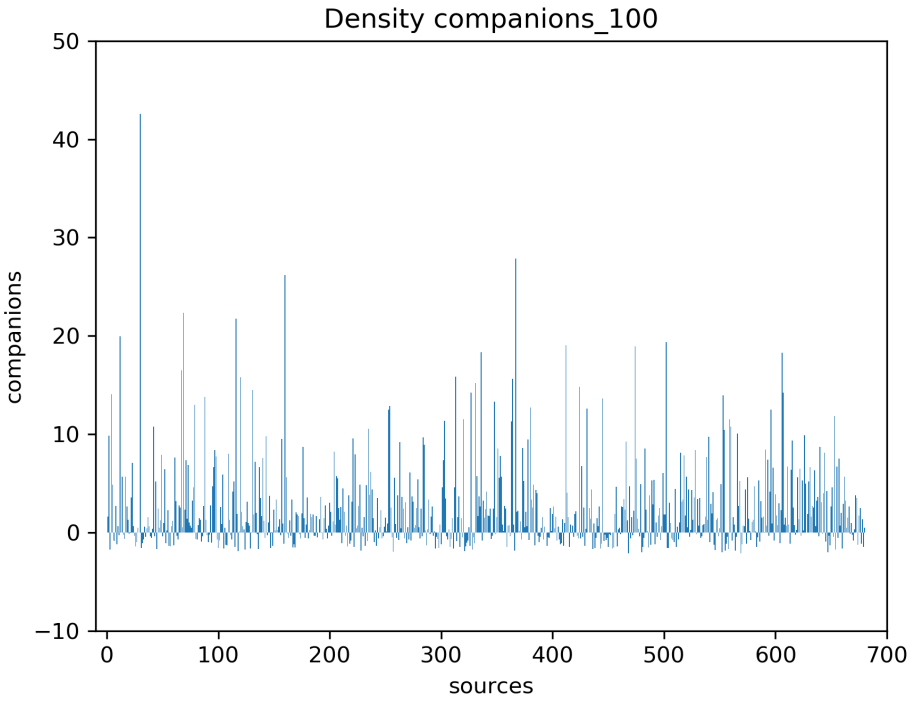

Figure 53: Source order vs n°companions, density approach, A100.

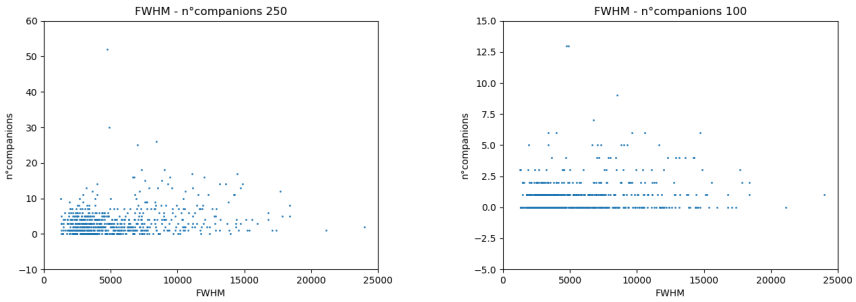

Figure 54: FWHM(H_β) order vs n°companions, density approach, A250 and A100.

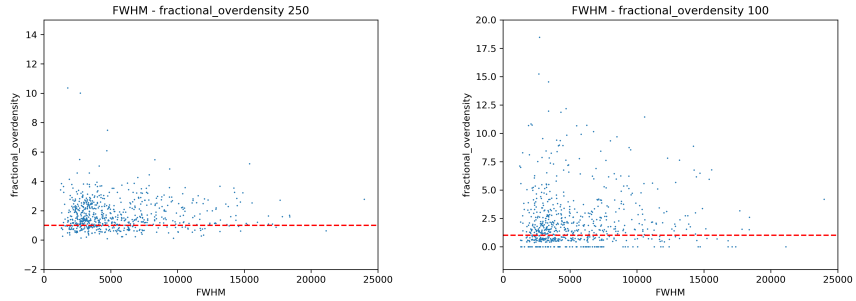

Figure 55: FWHM(H_β) order vs fractional overdensity, density approach, A250 and A100.

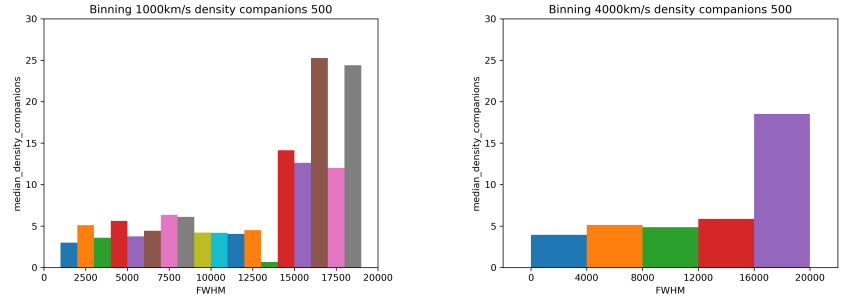

Figure 56: FWHM(H_β) binned vs median n°companions, bins=1000 and 4000 km s^{-1}, density approach, A500.

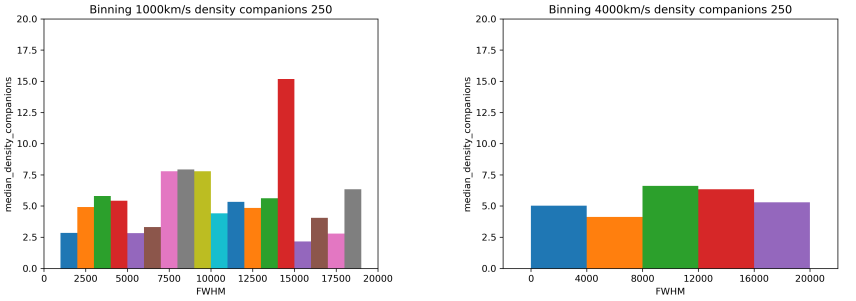

Figure 57: FWHM(H_β) binned vs median n°companions, bins=1000 and 4000 km s^{-1}, density approach, A250.

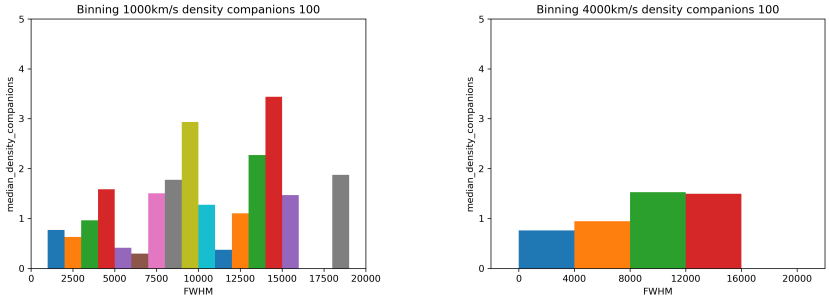

Figure 58: FWHM(H_β) binned vs median n°companions, bins=1000 and 4000 km s^{-1}, density approach, A100.

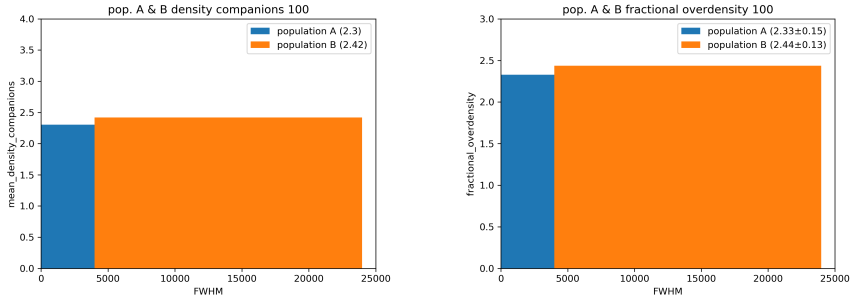

Figure 59: Mean number of companions and fractional overdensity of the mean number of companions for population A and B, density approach, A100.

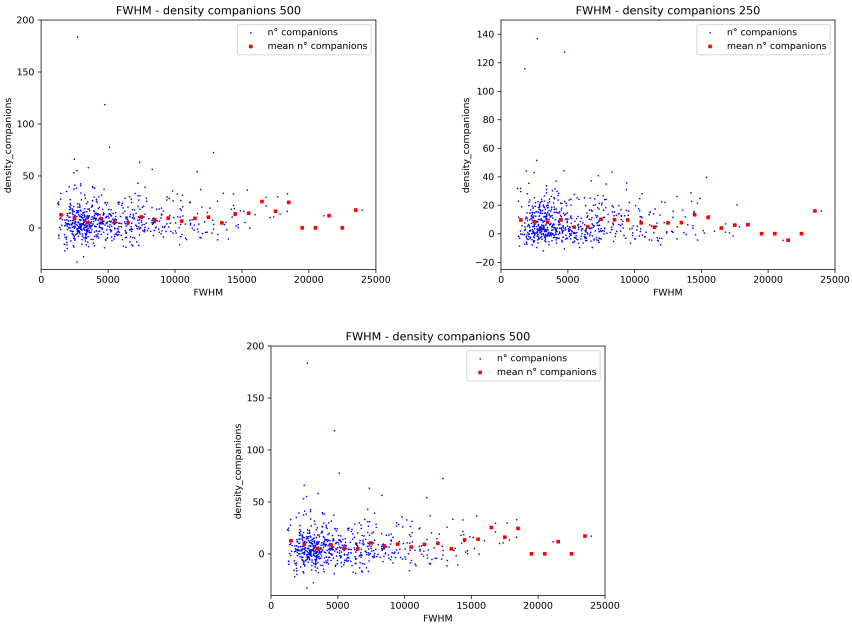

Figure 60: FWHM(H_β) order vs n°companions, superimposed mean n°companions with FWHM(H_β) bins=1000 km s^{-1}, density approach, A500, A250 and A100.

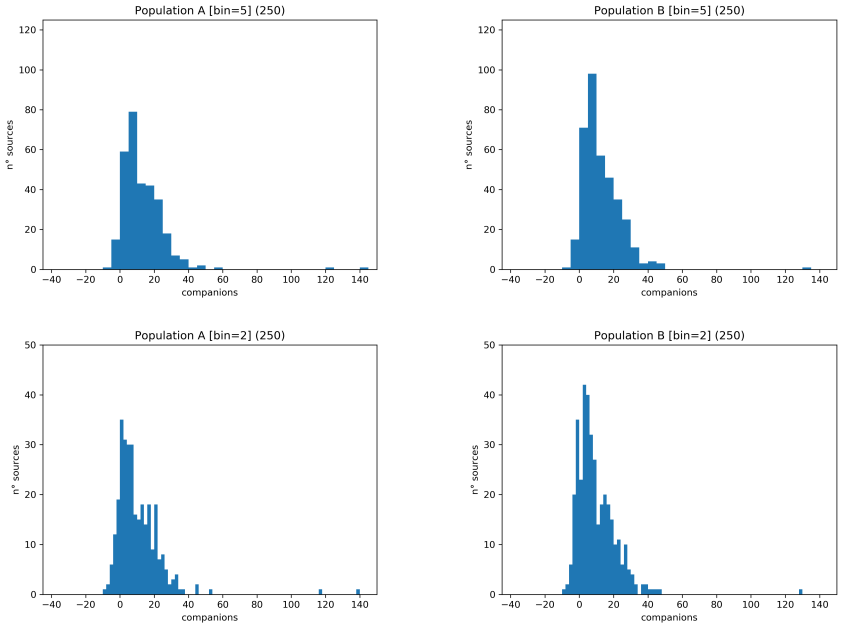

Figure 61: Companions' distribution, *top-left:* pop.A and bin=5, *top-right:* pop.B and bin=5, *bottom-left:* pop.A and bin=2, *bottom-right:* pop.B and bin=2; density approach, A250.

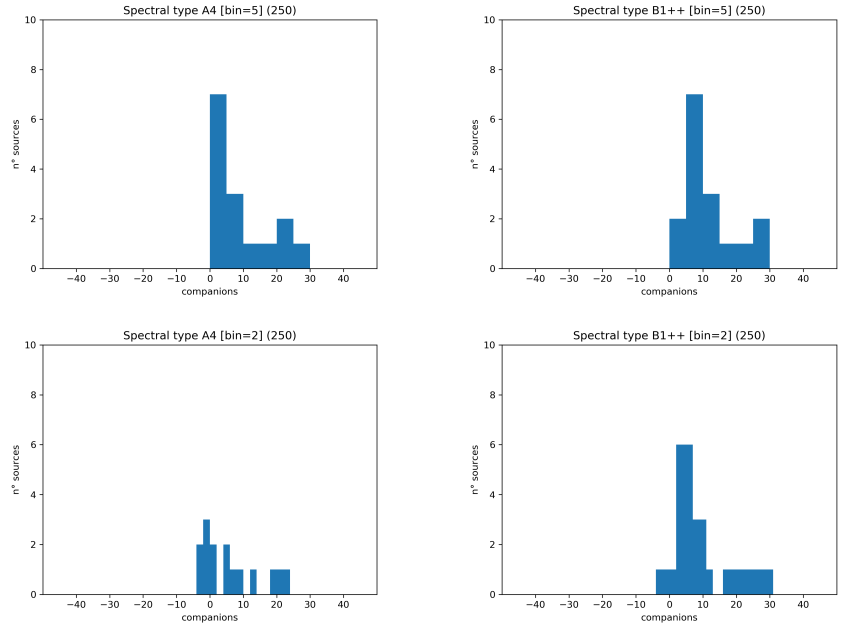

Figure 62: Companions' distribution, *top-left:* A4 sources and bin=5, *top-right:* B1++ sources and bin=5, *bottom-left:* A4 sources and bin=2, *bottom-right:* B1++ sources and bin=2; density approach, A250.

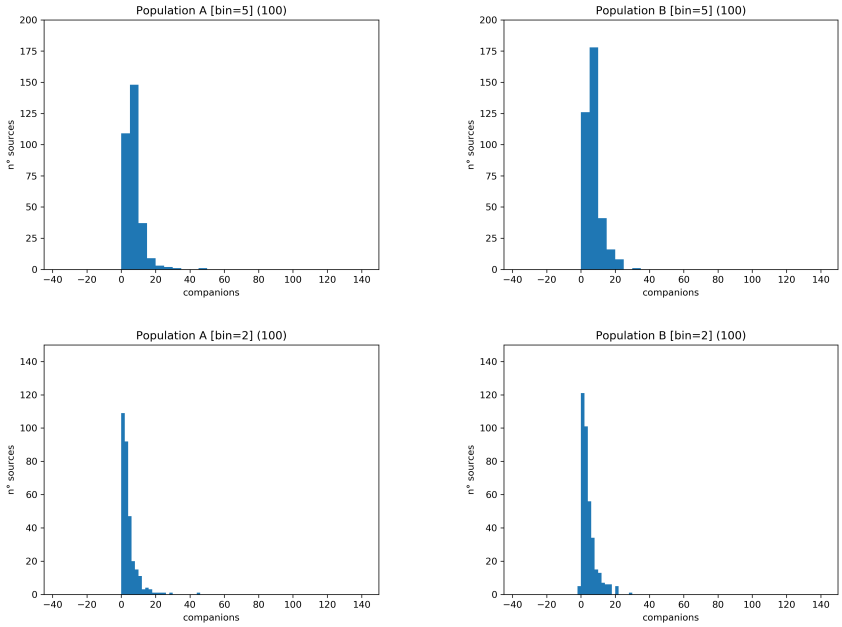

Figure 63: Companions' distribution, *top-left:* pop.A and bin=5, *top-right:* pop.B and bin=5, *bottom-left:* pop.A and bin=2, *bottom-right:* pop.B and bin=2; density approach, A100.

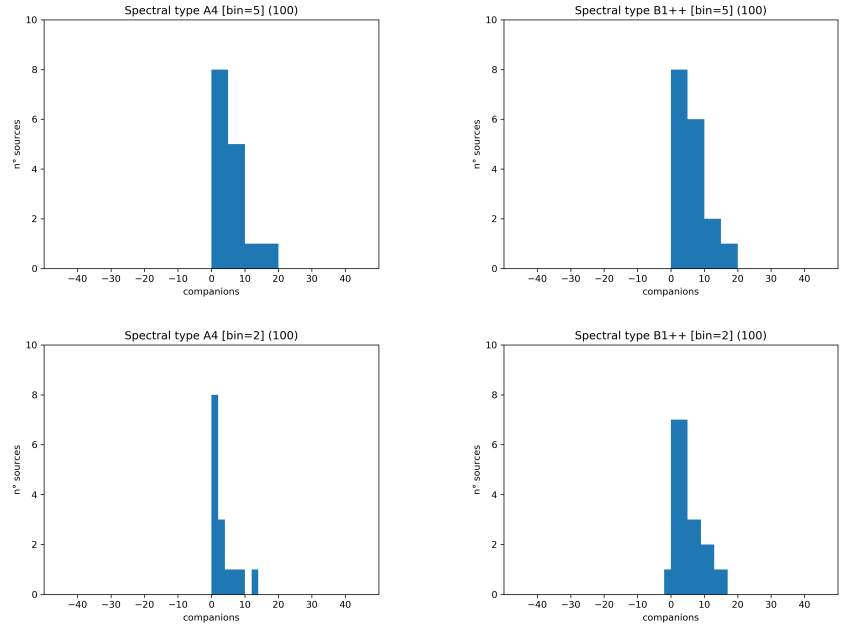

Figure 64: Companions' distribution, *top-left:* A4 sources and bin=5, *top-right:* B1++ sources and bin=5, *bottom-left:* A4 sources and bin=2, *bottom-right:* B1++ sources and bin=2; density approach, A100.